

Harmonic Poly-Actuator: Design and Control of a New Piezoelectric Mechanism

by

James Torres

B.S., Mechanical Engineering, Massachusetts Institute of Technology, 2010

M.S., Mechanical Engineering, Massachusetts Institute of Technology, 2012

Submitted to the Department of Mechanical Engineering in partial fulfillment of the requirements for the degree of

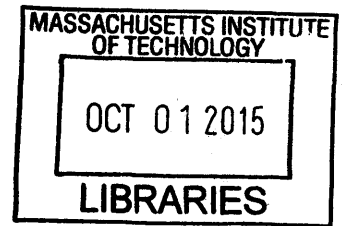
Doctor of Philosophy in Mechanical Engineering

at the

MASSACHUSETTS INSTITUTE OF TECHNOLOGY

September 2015

ARCHIVES



© Massachusetts Institute of Technology 2015. All rights reserved.

Author .. **Signature redacted**
Department of Mechanical Engineering
September 1, 2015

Certified by **Signature redacted**
H. Harry Asada
Ford Professor of Mechanical Engineering
Thesis Supervisor

Accepted by **Signature redacted**
David E. Hardt
Chairman, Department Committee on Graduate Students
Department of Mechanical Engineering

Harmonic Poly-Actuator: Design and Control of a New Piezoelectric Mechanism

by

James Torres

Submitted to the Department of Mechanical Engineering
on September 1, 2015, in partial fulfillment of the
requirements for the degree of
Doctor of Philosophy in Mechanical Engineering

Abstract

Piezoelectric devices, e.g. piezoelectric stack actuators, have several salient features inherent to their structure. They are efficient, have a high bandwidth, and their capacitive loading allows for static loads to be maintained with virtually no power consumption. The major preventative drawback that limits more widespread use is the small strain, on the order of 0.1%. For macro-scale applications, the displacement must be amplified, typically through mechanical or frequency leveraging. Both have inherent limitations: mechanical devices can increase the stroke but is naturally limited; and frequency devices relies on friction and is limited to nanopositioning.

In this thesis, we investigate combining a unique mechanical amplification with a frequency amplification device that does not rely on friction to produce an arbitrarily large stroke linear actuator. The first stage of amplification aims to achieve the greatest displacement amplification without sacrificing force capabilities. The second stage relies on the coordinated actuation of multiple copies of the mechanically amplified device to produce a long stroke, smooth force poly-actuator. The theoretical design concepts for each stage of amplification are explicitly derived. The mechanical amplification device uses rolling contact joints to maintain stiff connections to transmit the force without losses due to friction; and the frequency amplification uses a sinusoidal Transmission interface to exploit a passive balancing of undesirable non-linearities, proven by harmonic analysis. A unique control algorithm is developed to produce a wide variety of capabilities. The theoretical findings are supported by experimental prototypes. The mechanical amplification device produces a comparable energy density while amplifying the displacement by an additional factor 10. The proof-of-concept poly-actuator prototype can continually produce ± 100 Newtons of force over a stroke of 200 mm. We conclude with simulations, which are verified through physical experiments, used to estimate several performance metrics for comparison.

Thesis Supervisor: H. Harry Asada

Title: Ford Professor of Mechanical Engineering

Acknowledgments

First and foremost, I would like to thank Professor Asada. Over the past two years he has acted as my mentor and has helped develop my creativity, an attribute I never considered a strength prior to working with him. I greatly appreciate the patience he afforded me, while constantly pushing to me strive forward.

Furthermore, I would also like to thank the Sumitomo Heavy Industries, for their generous financial support that allowed me to pursue this captivating research and continue to grow as a student, an engineer, and a person.

I am grateful to my colleagues at the d'Arbeloff Laboratory. They were always available to provide another mind to brainstorm with, or a laugh when needed. Specifically, I thank Shinichiro Tsukahara who unquestionably helped me develop as an engineer, who taught me practices and tips not available in the classroom and how to attack a problem from all directions, and who I am blessed to call a friend.

Finally, and most importantly, I must thank my parents for their unwavering love and who serve as constant pillars of support. I am proud to say that I would not be the person I am today without the teaching, motivation, and care they have always provided me.

Contents

1	Introduction	21
1.1	Piezoelectric Actuator Technology	21
1.2	Previous Work	22
1.2.1	Amplification Mechanisms	22
1.2.2	Additional Actuator Types	24
1.3	Thesis Scope	24
2	Amplification Mechanism	27
2.1	Analysis of the Output Work Cycle	27
2.2	Buckling Amplification Concept	30
2.2.1	Kinematics	31
2.2.2	Functional Requirements of the Rotational Joint	34
2.3	Rolling Contact Flexure-Free Rotational Joint	34
2.3.1	Kinematics of Rolling Contact Joint	36
2.3.2	Maximizing Transmissibility	39
3	Harmonic Poly-Actuator	49
3.1	Harmonic Poly-Actuator Concept	49
3.2	Theoretical Analysis	51
3.2.1	Formulation of Unit Properties and Output Force	51
3.2.2	Elimination of the Effect of Non-Linear Stiffness	53
3.2.3	Transmission of Dynamics	56
3.2.4	Single Frequency Sinusoidal Inputs	58

3.2.5	Input Null Space	62
3.3	Force Ripple due to Unit Imbalance	64
3.3.1	Unit Properties	64
3.4	Generalization of the Transmission Function	67
3.5	Control Synthesis	69
3.5.1	On-Off Control Timing	70
3.5.2	Continuous Control	73
4	Implementation	77
4.1	Buckling Amplification Unit	77
4.1.1	Proof-of-Concept Unit	77
4.1.2	Poly-Actuator Buckling Unit	81
4.1.3	Design Optimization	85
4.2	Poly-Actuator	87
4.2.1	Additional Considerations	90
4.3	Experimental Implementation	91
4.3.1	Implementation of Electronics	91
4.3.2	Force Ripple Compensation Based on Error Model	91
4.3.3	Unit Force Control	93
4.3.4	Position Control	94
4.3.5	Simulation	95
5	Experimental and Simulation Results	97
5.1	Unit Results	97
5.1.1	Proof-of-Concept Unit	97
5.1.2	Poly-Actuator Unit	99
5.1.3	Discussion	100
5.2	Poly-Actuator Results	101
5.2.1	Experimental Results	101
5.2.2	Simulation Results	110
5.2.3	Discussion	117

6 Conclusion and Future Work	119
6.1 Project Goals	119
6.2 Contributions	120
6.3 Future Work	123
A Derivation of the Mechanism Transmissibility	125

List of Figures

1-1	A comparison of the (a) power density and (b) efficiency of piezoelectric actuators to a variety of other devices. Figure is taken from [14]. . . .	22
1-2	An example of common mechanical leverage technique. (a) A figure from one of the first versions of the concept, image taken from [23] (b) A schematic highlighting the source of compliance from the amplification structure.	23
2-1	A simple spring model of a PSA (a) alone, (b) in a compliant mechanism, (c) a lumped model including the compliant mechanism connected with the amplification transformer.	28
2-2	Cyclic loading and output work of a PSA in the force-displacement plane. (a) The ideal work output trajectory for a PSA without a preload is shown in dark grey $\overline{012}$, and the work output trajectory of a PSA coupled with a compliant mechanism is shown in light grey $\overline{0'1'2'}$. The ideal work output trajectory for a preloaded PSA in dark grey is the parallelogram outlined by $\overline{0123}$, and that of a preloaded PSA with a compliant mechanism is in light grey outlined by $\overline{0'1'2'3'}$ (b) in the frame of the PSA and (c) in the frame of the mechanism output. . . .	28
2-3	A basic schematic of the buckling amplification mechanism.	31
2-4	A plot of the instantaneous amplification gain G (blue), the total gain \bar{G} (green), and the peak-to-peak gain G_{pp} (red) as a function of the input displacement z for an initial length $L = 40$ mm. The displacement range relates to a PSA strain of 0.1%.	32

2-5	A sketch of the amplification mechanism force-displacement relationship. The initial slope increases with the input u . Note the position $y = 0$ is a singular point where the mechanism force f_y is always zero.	33
2-6	A labeled schematic of the rolling contact joint buckling amplification mechanism.	35
2-7	A displaced configuration of a portion of the rolling contact buckling mechanism. Note, due to the fact that the mechanism is symmetric, half of it is shown for brevity.	37
2-8	This plot relates the peak-to-peak amplification gain of the buckling unit G_{pp} to the characteristic radius Γ where z is held constant at 40 micrometers, the free displacement of the PSA. The cap center distance Δ_0 is zero and the cap profile radius r is 30 millimeters.	38
2-9	A schematic of the rolling contact buckling mechanism. (a) A general rolling contact buckling mechanism at the singular configuration with several parameters labeled, including the cap radius r , the base radius R , and the cap center distance Δ . (b) A special case, $\Delta = 0$ in the displaced configuration showing the alignment of the contact forces f_c and faces of the rolling surface. (c) A non-zero cap center distance $\Delta \neq 0$ that requires a friction force to stay balanced due to the misalignment angle μ .	40
2-10	A preloaded PSA using shape memory alloy wires with super-elastic properties.	41
2-11	The benefit of preload compensation springs (PCS). (a) Shows a simple schematic of the preload process and corresponding stabilizing spring. (b) Shows the equal slope of the initial instability due to preloading and the PCS stiffness at the center position $y = 0$. Note the input u is zero for this example.	42

2-12 A schematic detailing the force balance on the output node based on the constant preload force in the direction of the PSA, f_{pre} , and the PCS force, $f_{pcs} = -k_y y$. Note that the preload force in the y -direction, $f_{y,pre}$, is the summation of the two forces in the z -direction. Furthermore, the $f_{y,pre}$ is exactly balanced by the f_{pcs} 43

2-13 A plot of the transmissibility as a function of the normalized serial stiffness. This plot assumes the parallel stiffness is effectively zero. . . 46

2-14 A plot showing the normalized joint stiffness as a function of the normalized preload. The stiffness and preload are normalized with respect to the PSA's stiffness and blocking force, respectively. The cap and base material is steel and each profile radius is 25 millimeters. 48

3-1 This schematic highlights the key features of the harmonic PA: the input Units with displacement y ; the output, or Transmission with position x ; and the interface between the two, including the sinusoidal waveform and the rollers transmitting the force. Note that the Transmission waveform itself is offset from a sinusoid, such that the rollers, and therefore the Units, track a pure sinusoid (the dashed line). 50

3-2 A schematic of the force transmission of the i^{th} Unit roller along the slope of the Transmission. The slope and the ratio of the two forces are directly related as defined in Eq. (3.3). 52

3-3 A schematic of the force transmission within a general PA architecture. The i^{th} Unit located at $\theta_i = \theta + \theta_i^o$ outputs a force f_i which is transformed by the sinusoidal Transmission to output F_i . The total force F is the sum of the contribution from all n Units. The transmission ratio from f_i to F_i is determined by the location and the geometry of the sinusoid, A and λ 54

3-4	An FFT of the output force ripple associated with a few example cases: the linear passive stiffness term in the buckling Unit h_1 ; the cubic passive stiffness term in the buckling Unit h_3 ; the Unit preload force f_{pre} ; the vertical zero position of the Unit y_o ; and the relative position of the Unit along the Transmission x_i	66
3-5	Sensitivity of two parameters: (a) the linear term in the buckling Unit force associated with the preload and the PCS h_1 (the provided example case), and (b) the location of the buckling Unit along the Transmission x_i . Note the dashed lines are the 1 sigma bound of the average values.	67
3-6	A schematic showing the control timing with respect to the Transmission for charging θ_c (dashed) and discharging θ_d (dot-dash).	71
3-7	A smooth surface showing the average PA output force as a function of both the charge and discharge phase. Note the plot is symmetric as the actuator has no preferred direction. Furthermore, the contours on the θ_c - θ_d plane show lines of constant average output force.	72
3-8	The output force-displacement profile given the input defined in (3.27a). The parameters C and φ are input control parameters. Note the stable regime surrounding the equilibrium point at $\varphi + \frac{\pi}{2}$ is a passive property that does not require any measurement or active control. Furthermore, if the PA is loaded by amount \bar{F}_{load} the input can be used to tune the stiffness \bar{K} at the shifted equilibrium point $l\bar{\theta}$	73
3-9	A plot showing two signals that both produce the same output. First, a sample input signal (solid line) utilizing the second mode of a system with 20 Units. Second, a signal (dashed line) minimizing the sum of the squared inputs that combines the original with a sixth order signal.	75
4-1	Test bed of the high-gain, rolling-contact PSA buckling amplification mechanism.	78

4-2	A labeled diagram of the cap-base profile contact. To avoid friction, there is a designed gap between the gear tooth and the slot on the cap. Ideally, the gear is used only for alignment during assembly and as a failsafe mechanism.	80
4-3	A plot showing the nonlinear Hertzian contact stiffness for the cylindrical and crowned caps. Note the large change in stiffness due to an angular misalignment when the caps are cylindrical.	80
4-4	A simple schematic highlighting the crowning on both the cap and the base profiles. Note the concave crown radius of the base is larger than the convex crown radius of the cap.	81
4-5	The buckling amplification Unit implemented in the PA. (a) A size comparison of between the proof-of-concept prototype and the PA Unit. (b) A labeled diagram showing a few of the new key features. . .	82
4-6	Force-displacement plot of the biased amplification Unit. Note the force is always positive and there is never a neutrally stable point. Furthermore, the peak forces for either extreme, on or off, are approximately the same magnitude ensuring low wear.	84
4-7	A figure provided by the PSA manufacturer describing the maximum off axis load angle ϑ	86
4-8	A reproduction of Fig. 2-7 to highlight off axis loading by angle ϑ caused by the rolling contact joint.	86
4-9	A plot of the maximum allowed amplification gain G_{pp} as a function of the length-to-width aspect ratio of the PSA, limited by the shear force caused by the rotation along the rolling contact joint.	87
4-10	Labeled pictures of the proof-of-concept PA prototype in (a) a disassembled and (b) assembled configuration. The encoder read head and power amplifier are not pictured.	89
4-11	A labeled picture of the experimental implementation, including the PA, driving lead screw, and output measurement load cell.	92

4-12	A block diagram of the feedforward force control including the ripple compensation and the phased sinusoidal inputs u	93
4-13	A block diagram of the Unit force feedback control including the ripple compensation. Instead of producing the inputs directly, the phased sinusoidal inputs generate the reference inputs f_r . Note the double lines denote a vector of size n , the number of Units.	94
4-14	A block diagram using a general linear controller G_c to generate a force command to follow the reference position, x_d	94
4-15	A schematic of the mechanical dynamic model used in the simulation	96
5-1	A plot of the force-displacement trajectory comparing the model of the initial prototype and the measured performance. A measured peak-to-peak displacement, Δy_{p-p} , of 4.2 mm and transmissibility, γ , of 61% was achieved.	98
5-2	Spatial FFT of the output force ripple. The frequencies relate to the pitch of the gear and are affected by the discrepancies between Units, including position and stiffness.	102
5-3	Two plots of the output force with a command of 0 N as a function of the output displacement. (a) In the first, the force ripple due to imbalanced Units is not compensated, but a model was developed based on a 6 th order Fourier series model, shown in red. (b) The same command was given, but the ripple was compensated using the method shown in Fig. 4-14. Note the scales for both plots are the same.	103
5-4	A plot showing the measured output force for three different inputs. The desired output is shown in the fine dashed line. Note this controller does include the ripple compensation.	103
5-5	A plot showing the measured output force for three different inputs. The desired output is shown in the fine dashed line. Note this controller does include the ripple compensation.	104

5-6	A plot of the individual Unit force control as function of the PA output displacement. A reference command (shown in blue) is passed to a feedback controller that varies input voltage (shown in green) to change the Unit force which is then measured (shown in red). In this example case the reference command is based off a desired PA output force. The expected (feedforward) command is shown in black.	105
5-7	The output force of the PA as a function of output position utilizing Unit force control. The blue line plots solely the Unit force control, whereas the black line shows the Unit force control in conjunction with ripple compensation.	106
5-8	A step response of the PA with a proportional controller. Note a steady state error exists due to the force ripple and static friction.	108
5-9	Several 1 mm step responses were measured at different initial positions utilizing a PI controller and ripple compensation. The variety of responses is due to the difference in the ripple force with position. Ultimately, the integrator is able to overcome the disturbances, but with a long time constant.	108
5-10	A step response exemplifying the two time scales of the PI controller. Both plots show the same experiment, however the first (a) shows the time scale of the velocity saturation region, and the second (b) shows the slow response of the integrator term. Note both plots have the same time scale.	109
5-11	Lead-lag step response	110
5-12	Several plots showing the verification of the electrical dynamics between the physical prototype and simulation. In general, the discrete points are measurements, whereas the continuous lines are simulation data.	112

5-13	A bode diagram of the output force with respect to the input frequency. The bandwidth changes with input because the current saturation affects the larger voltages sooner. Note the discrete points represent experiments, whereas the continuous lines are simulation data.	113
5-14	The measured and simulated step response of the PA. (a) Shows the complete response over, whereas (b) enlarges the response near the commanded position to highlight the dynamic response.	113
5-15	A plot of the simulated PA force as a function of the output velocity, both with and without amplifier current saturation.	114
5-16	A plot of the simulated PA output power as a function of the output velocity, both with and without amplifier current saturation.	116
A-1	The force-displacement trajectory, c , of a PSA with stiffness, blocking force and free displacement of k_{psa} , F_{block} , and z_{free} , respectively, within a mechanism with a serial and parallel stiffness, k_s and k_p , respectively.	126

List of Tables

4.1	Tabulated parameters for the prototype shown in Fig. 4-1	79
4.2	Summary of Parameters of the PA Buckling Units	82
4.3	Summary of Parameters of the Harmonic PSA Poly-Actuator	88
5.1	Summary of Poly-Actuator Unit Measurements	100
5.2	Comparison of Several PSA Mechanical Amplification Devices	100
5.3	Comparison of Actuator Properties	117

Chapter 1

Introduction

1.1 Piezoelectric Actuator Technology

Capacitive actuators, such as piezoelectric actuators, consume virtually no power for generating a static force while maintaining a constant position. In contrast, electromagnetic actuators consume energy whenever a torque/force is generated. Grounded robots are able to bear substantial gravity loads for long periods of time via gearing, but they sacrifice backdrivability. Backdrivability is a key feature for robotic interactions with humans, e.g. stroke rehabilitation [20], but the robotics field has been shifting towards wearable mechanisms increasing the importance of weight and efficiency. [2, 31] This fact motivated the present work towards piezoelectric actuators. By eliminating energy consumption for bearing nearly constant torque loads, we can significantly improve the actuators' energy efficiency.

In addition to interactive robotics, piezoelectric actuators are suitable for use where magnetic fields can cause a disruption. They are already frequently used to drive mechanisms for use in MRI machines for this very reason. [43, 34] However, their use could be expanded for driving additional components, such as the continuously moving table [45], provided they could meet the necessary specifications. In machine tools, permanent magnetic linear motors are the standard, but they may develop issues when working with ferromagnetic materials. [4, 1] These motivating examples provide benchmarks for the design specifications of the proposed actuator.

Beyond their capacitive properties and backdrivability, piezoelectric actuators have several desirable attributes including: a high bandwidth, large power density and excellent mechanical efficiency. [16] See Fig. 1-1 for details.[14] However, piezos lack the strain to be practically used in macro-scale systems. Typically, the amplification is achieved one of two ways: frequency leveraging, e.g. ultra-sonic motors; or, external mechanical leveraging, e.g. flexure pivot mechanisms.[32]

The objective of this thesis is to develop the concepts of a device that utilizes piezoelectric actuators that is backdrivable and can produce an arbitrarily long stroke.

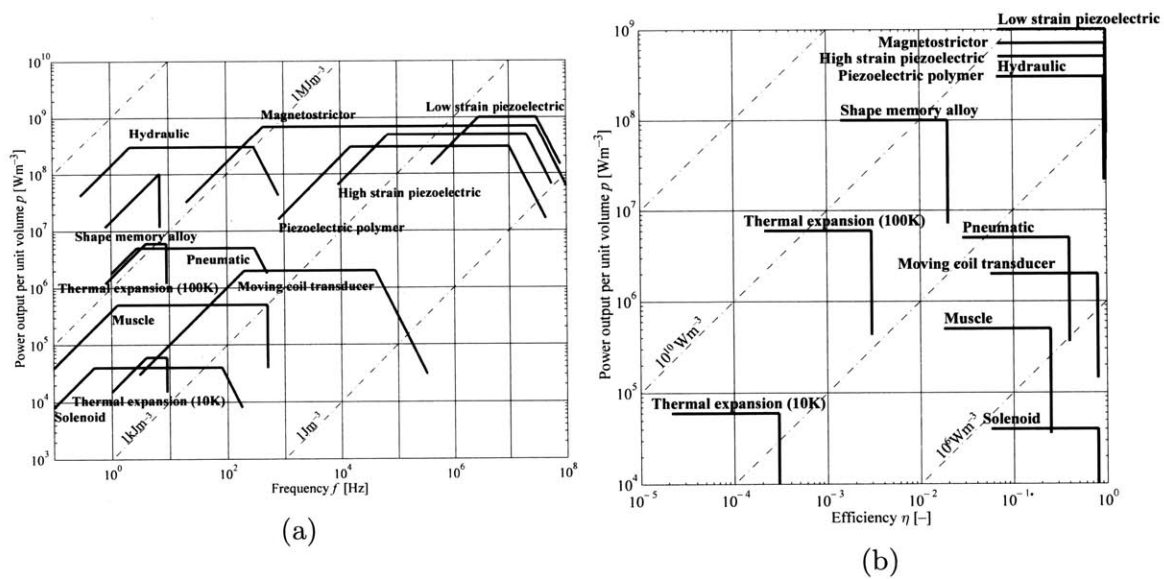


Figure 1-1: A comparison of the (a) power density and (b) efficiency of piezoelectric actuators to a variety of other devices. Figure is taken from [14].

1.2 Previous Work

1.2.1 Amplification Mechanisms

The most common technique to linearly amplify the displacement is to utilize a low angle flexure hinge to leverage an output. There are several implementations of this design, including the Moonie [28], the Cymbal-type [8], and the Rhombus [23], but they all have the same basic principal. An example is shown in Fig. 1-2, where (a)

shows a physical prototype with the flexure rotational joints at A and B and (b) shows a compliant model of the structure with input z and output y .

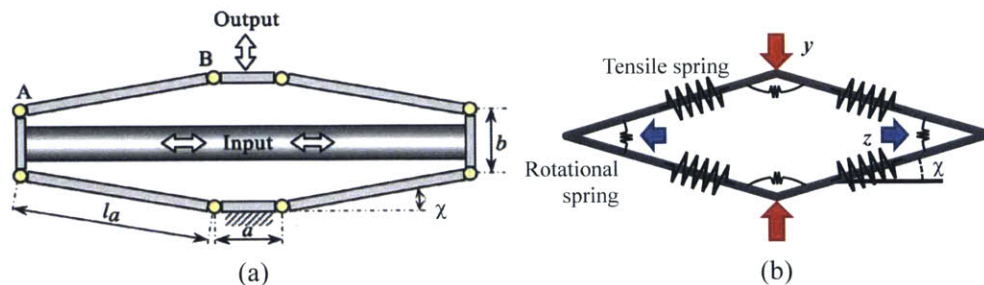


Figure 1-2: An example of common mechanical leverage technique. (a) A figure from one of the first versions of the concept, image taken from [23] (b) A schematic highlighting the source of compliance from the amplification structure.

These mechanisms have a wide variety of applications including wing flap control [11, 13], scanning stages [12, 17, 26], and valve control [37], but for the most part they are servo actuators. The amplification ratio is determined by the initial linkage angle χ , with typical values of 2° and 20 for the angle and amplification ratio, respectively. Most designs have amplification ratios ranging from 5 to 20 depending on their purpose. The spring schematic shown in Fig. 1-2(b) shows that this design has both a parallel (rotational) and serial (tensile) stiffness. Unfortunately, these are both dominated by the design of the flexure rotational joint. The ideal scenario is an infinite serial stiffness and no parallel stiffness, but because both are directly related to the same physical component there is an inherent tradeoff. This leads to typical transmissibility values of 0.5.

A benefit of this design is that it can be nested, i.e. the input z shown in Fig. 1-2(b) could be the output y of a previous stage. This leads to much larger displacement amplification ratios, over 100. [35, 41, 18] Due to the flexure, however, the same tradeoff must be made between parallel and serial stiffness. This yields a transmissibility on the order of 0.2 or lower.

The most prevalent form of frequency-leveraged piezoelectric actuator is the ultrasonic motor (USM). These motors utilize a cyclic, high frequency input to produce continuous linear [40], rotary [24], or complex multi-DOF motions [39, 25]. However,

due to their reliance on friction, it is difficult to transmit a large force reliably under varying load conditions, which results in a low power density, around 10^4 W/m^3 [29]. The lack of effective means to match impedance between the piezoactuator and the output through the friction drive also contributes heavily in the lower power density. Furthermore, the reliance on friction forfeits the actuators backdrivability. Beyond USMs, there are many ways of converting cyclic motion into a continuous output using PSAs. Inching motion was generated for a compliant leg walking robot [42], and repetitive wing or fin motion was used for a flying micro-robot [10] and an underwater robot [7].

1.2.2 Additional Actuator Types

A brief survey of the existing linear actuator technologies is shown as a basis of comparison to the work presented. Permanent magnet linear motors require long chains of permanent magnets that can interfere with magnetic components or sensitive equipment.[1] Furthermore, the long string of permanent magnets can make particularly long stroke mechanisms prohibitively expensive. Lorentz force actuators can be accurate, but have a low power density and limited stroke.[9] Hydraulic actuators are also capacitive and can have a tremendous force and power density. However, the nonlinear properties can limit the resolution and the salient features do not scale well when the size of the actuator is reduced. [15] Similarly, pneumatic actuators are also capacitive and backdrivable and are appropriate for lightweight robotic systems, hence their frequent use in skeletal hand robots. [21] However, they are limited in terms of efficiency and power density.[14]

1.3 Thesis Scope

The objective of this project is achieved with an architecture that combines aspects of both amplification methods. The new proposed actuator would be able to create an arbitrarily long stroke, similar to the frequency leveraged mechanisms, but by first amplifying the displacement, friction can be avoided to maintain backdrivability.

This comes at the cost of power/force density and bandwidth due to the mass added in the multiple stages of force transmission.

There are several goals for this work that make the design unique, allow the device to be useful in practice, and lead to novel contributions:

- Create a mechanical amplification stage that maximizes the amplification and the energy transmission: The first amplification stage (mechanical) is used a single Unit and focuses on solely on the increase of displacement such that its interaction with the overall actuator does not rely on friction. This relaxes the functional requirements of the singular Unit related to the force-displacement properties and the instantaneous stiffness as a function of displacement. Instead the design concept can maximize the transmissibility and the amplification with the realization that any imposed additional functional requirements can be addressed in the actuator as a whole.
- Create a backdrivable actuator: The second amplification stage (frequency) is quite similar to USM in general concept when it comes to locomotion, but with the amplification mechanisms the interface between the Unit and the Output, deemed the Transmission, does not have to flat and rely on friction. Instead, the Transmission surface can be a cyclic function that can transmit the force generated by the Units to the output or vice versa. The efficiency of the transmission of energy in either direction is related to the specific geometry and bearing friction between the two mechanisms.
- Create a poly-actuator: The actuator employs multiple Units, hence poly-actuator, working collectively to provide novel capabilities. One capability is to provide a smooth output force that is independent of position. This is achieved via an additional key feature of the Transmission: to transmit force between the Units themselves in addition to/from the Output. This creates a functional requirement for the interaction of the Unit force profile and Transmission shape based on the number and location of Units.

- Synthesize a control scheme that provides flexible control and a smooth output: The control scheme of the poly-actuator is complex given the high degree of nonlinearity in both stages of amplification. This creates a unique control design that can further exploit the geometry of the Transmission and the multitude of Units to control.
- Create an actuator that achieves specific performance benchmarks: Given the motivating examples, benchmarks are set for the performance of the actuator in terms of power, force, precision and accuracy. These benchmarks motivate the design of the physical prototype and any additional simulation to evaluate the applicable design space.

These goals drive the overall direction of the research. This thesis first discusses the design concept behind the mechanical amplification mechanism in Chapter 2. This includes the general properties of the new type of mechanical amplification and the unique implementation aspects that maximize decisive metrics. Next, the poly-actuator design concept is presented in Chapter 3. The specified goals of the poly-actuator are rigorously proven and an analysis is provided for practical considerations if the conditions of the theory are violated. In addition, a versatile control algorithm is presented. Chapter 4 details additional important implementation details for the mechanical amplification mechanism, poly-actuator, and control. Finally, Chapter 5 presents experimental results of several prototypes and uses a dynamic simulation to predict the peak performance of the actuator.

Chapter 2

Amplification Mechanism

The goal of the initial mechanism is to amplify displacement on the order of 100 times, while simultaneously maintaining energy output capabilities of the piezoelectric stack actuators (PSAs). The amplified displacement allows for the interface between the unit and the output of the total actuator to be independent of friction, which maintains several of the previously highlighted features, including: backdrivability and force control.

2.1 Analysis of the Output Work Cycle

Consider a force-displacement plane as shown in Fig. 2-2. Assume that the actuator follows cyclic trajectory within this plane. The quasi-static work produced by the PSA in a single cycle, W_{out} , is given by the closed loop integral within the force-displacement plane:

$$W_{out} = \oint f_z \cdot dz \quad (2.1)$$

where f_z and z are the output force and displacement of the PSA, respectively.

Maximizing this work output I can fully exploit the potential of a PSA. For simplicity, assume the PSA can be initially modeled as a force source in parallel with

a spring, as shown in Fig. 2-1(a). The force produced by the force source f_{in} is proportional to the input voltage u . The PSA has a natural stiffness associated with the material properties k_{PSA} and an output force and displacement, f_z and z respectively. This model yields a linear force-displacement property, as shown in Fig. 2-2(a). For a given maximum voltage, u_{max} , the maximum work output is determined by the area of the triangle connecting the origin point 0, the blocking force, f_{block} at point 1, and the free displacement, z_{free} at point 2, if the PSA can only be loaded under a compressive force: $f \geq 0$. Therefore, the total output work from the PSA is $W_{out} = f_{block} \times z_{free}/2$.

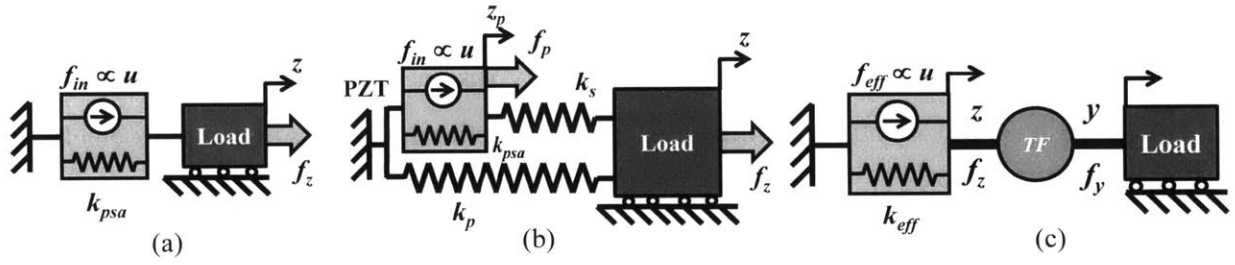


Figure 2-1: A simple spring model of a PSA (a) alone, (b) in a compliant mechanism, (c) a lumped model including the compliant mechanism connected with the amplification transformer.

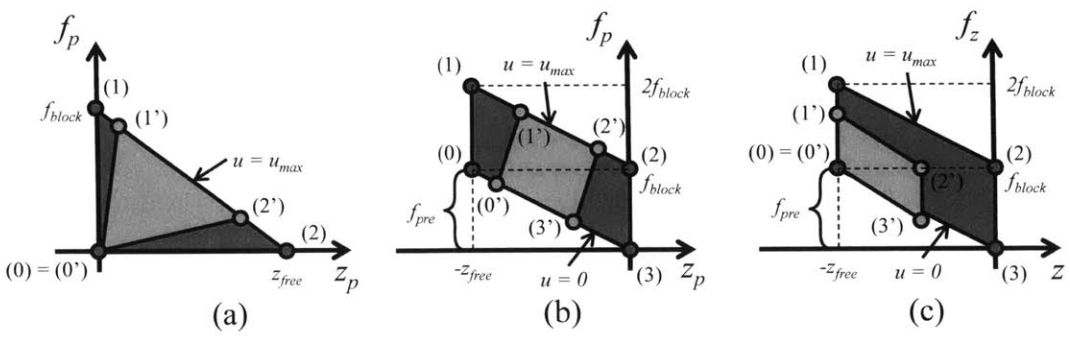


Figure 2-2: Cyclic loading and output work of a PSA in the force-displacement plane. (a) The ideal work output trajectory for a PSA without a preload is shown in dark grey $\overline{012}$, and the work output trajectory of a PSA coupled with a compliant mechanism is shown in light grey $\overline{0'1'2'}$. The ideal work output trajectory for a preloaded PSA in dark grey is the parallelogram outlined by $\overline{0123}$, and that of a preloaded PSA with a compliant mechanism is in light grey outlined by $\overline{0'1'2'3'}$ (b) in the frame of the PSA and (c) in the frame of the mechanism output.

If a negative output force is allowed, i.e. a tensile force, the overall work trans-

mitted can be increased. This is achievable with use of a preload mechanism that provides a bias force so that “net tensile” force is allowed. Suppose that a preload as large as the maximum blocking force is applied. By shifting the origin from point 3’ to point 0 in Fig. 2-2(b), I can redraw the force-displacement plane that is expanded to allow forces in both directions. The theoretical maximum work output is outlined by the trajectory $0 \rightarrow 1 \rightarrow 2 \rightarrow 3 \rightarrow 0$. This produces a total output work equal to $W_{out} = f_{block} \times z_{free}$, which is double the output without the preload. Note, however, that this is under the assumption that the preload is kept constant at least at the magnitude of the blocking force independent of the PSA’s displacement, $f_{pre} = \text{constant} \geq f_{block}$. If the preload varies (typically increasing with relation to the PSA displacement z), it can effectively be modeled as an additional parallel stiffness.

In reality however, the net usable work output is smaller than this theoretical limit. In particular, when a compliant mechanism is used for amplifying the displacement, the structure reduces the serial stiffness, lowering the PSA force f_p , while any additional parallel stiffness impedes the displacement of the PSA z . In general the static characteristics of such displacement amplification mechanisms can be represented by a simple icon model, as shown in Fig. 2-1(b). The compliant elements distributed across the mechanical structure can be lumped to two springs: one serial spring with stiffness k_s , and one parallel spring with stiffness k_p . For the purposes of this comparison analysis, the hysteresis of the PSA is ignored as it is a common factor among all PSAs [5].

Due to this serial compliance the PSA force transmitted to the load cannot reach the highest point, i.e. the blocking force. If the mechanism output displacement z is constant as the PSA input is increased, the PSA displacement z_p will expand slightly due to the serial compliance, reaching point 1’ in Fig. 2-2(a). Similarly, as the PSA output expands, the parallel stiffness prevents it from fully expanding such that it only reaches point 2’. Overall the work output is reduced, as indicated by the shrunken area of triangle $\overline{0'1'2'}$ compared to $\overline{012}$. From this analysis I can conclude that the ideal displacement amplification mechanism must have an infinitely large serial stiffness and zero parallel stiffness: $k_s \rightarrow \infty, k_p = 0$.

This conclusion holds for the preloaded case as well. The area of the parallelograms $\overline{0'1'2'3'}$ in Figs. 2-2(b) and (c) are again limited by structural stiffness. Note the difference between the two plots is the force-displacement plane. The force-displacement plane in Fig. 2-2(b) is in the reference frame of the PSA f_p - z_p , whereas the force-displacement plane of Fig. 2-2(c) is in the reference frame of the structure output, f_z - z . There are no loss mechanisms in this model between the PSA and the structure, therefore the work output in both are identical. This reduction in work output can be characterized with a single metric: transmissibility. Transmissibility is defined as the work output of one cycle of actuation normalized by a characteristic energy of the PSA, $W_{psa} = F_{block} \times z_{free}$. If k'_s and k'_p are the stiffness of the serial and parallel springs, respectively, normalized by the PSA stiffness, then the transmissibility, γ , can be described as the following:

$$\gamma \equiv \frac{W_{out}}{W_{psa}} = \frac{k_s'^2}{(k_s' + 1)(k_s' + k_p' + k_p'k_s')} \quad (2.2)$$

The functional relationship between input displacement z and output displacement y is determined by the amplification gain of the transformer, denoted by TF in the figure. Note that the transformer is modeled as ideal and does not affect the transmissibility, since it is a kinematic component, neither storing nor dissipating energy. Therefore, the above expression gives the transmissibility at the mechanism output y . This transmissibility reinforces the previous conclusion that if $k_p = 0$ and $k_s \rightarrow \infty$, the transmissibility, γ , approaches 1. The derivation of Eq. (2.2) is shown in Appendix A.

2.2 Buckling Amplification Concept

The goal of the new amplification mechanism is to produce the same large amplification ratios, on the order of 100, but with a much higher transmissibility, over 0.5. This is achieved with a buckling amplification mechanism, which utilizes a single

stage amplification to minimize the stacking effect of multiple stages, but produces a large amplification ratio by reducing the initial linkage angle χ to zero.

Figure 2-3 shows the schematic of the buckling amplification mechanism. Two PSAs are linearly aligned with a connecting component between them, referred to hereafter as the “output node,” that displaces perpendicular to the original axis of alignment, as shown in the figure. As the PSAs elongate, they rotate causing a phenomenon similar to buckling. The buckling mechanism allows for bi-polar swing of the output displacement across a kinematic singular point in the middle. This kinematic singularity will be addressed later in the design. [27]

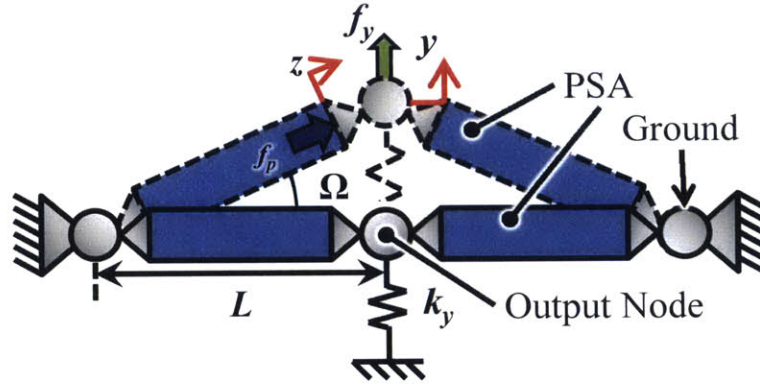


Figure 2-3: A basic schematic of the buckling amplification mechanism.

As the PSA, with an initial length L , increases in length by amount z , the structure “buckles” vertically a distance y . This rotates the PSA by an angle Ω about the ground rotational joints. A portion of the force produced by the PSA f_p is transmitted to the mechanism output f_y . A spring with stiffness k_y is added to the output node to stabilize the whole system.

2.2.1 Kinematics

The input (PSA) displacement z and mechanism displacement y can be related to the initial length L .

$$y^2 = (L + z)^2 - L^2 = 2Lz + z^2, \quad \frac{z}{L} \ll 1 \quad (2.3)$$

$$y \approx \sqrt{2Lz}$$

The assumption in 2.3 is valid for PSAs which typically have strains, i.e. $\frac{z}{L}$, of 0.1%. The instantaneous amplification gain G can be described as the derivative of the mechanism displacement y with respect to the input (PSA) displacement z . The total gain \bar{G} is defined as the ratio of the mechanism displacement to the input displacement.

$$G(z) = \left. \frac{dy}{dz} \right|_z = \sqrt{\frac{L}{2z}}$$

$$\bar{G}(z) = \frac{\Delta y}{\Delta z} = \sqrt{\frac{2L}{z}}$$
(2.4)

where Δy and Δz are the total change in the mechanism and input displacement, respectively. When $z = 0$ the gain is infinite, but once the PSA begins to extend, the gain rapidly decreases as shown in Fig. 2-4. As mentioned previously, the buckling mechanism allows for a bi-polar swing where the output node swings through the kinematic singularity. This effectively doubles the output gain, explicitly the peak-to-peak gain is: $G_{pp} = 2G(z_{max})$.

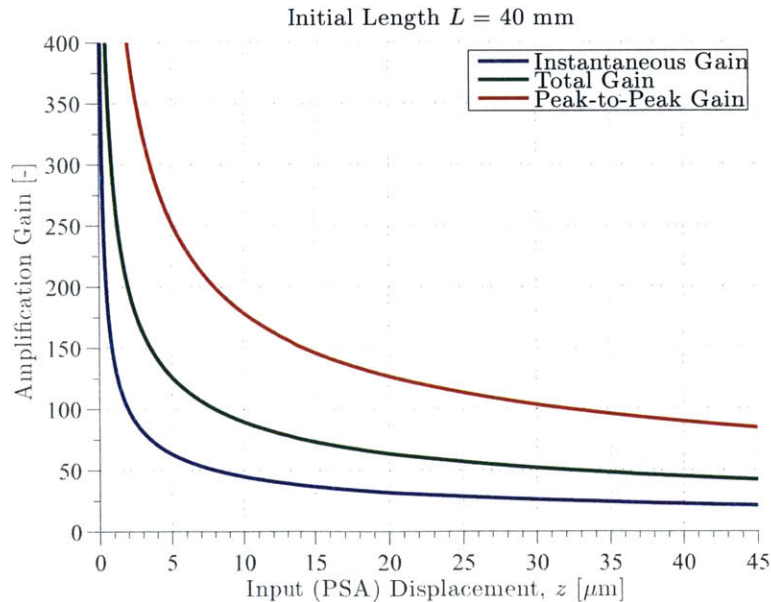


Figure 2-4: A plot of the instantaneous amplification gain G (blue), the total gain \bar{G} (green), and the peak-to-peak gain G_{pp} (red) as a function of the input displacement z for an initial length $L = 40$ mm. The displacement range relates to a PSA strain of 0.1%.

Similarly, the input (PSA) force f_z can be related to mechanism force f_y :

$$f_y = f_z \cdot \sin \Omega - k_y y = f_z \frac{y}{L+z} - k_y y, \quad \frac{z}{L} \ll 1$$

$$f_y \approx f_z \frac{y}{L} - k_y y$$
(2.5)

Replacing f_z with an ideal model of the PSA, the mechanism force f_y can be related to the displacement y by combining Eqs. 2.3 and 2.5:

$$f_z = f_{in} - k_{psa} z = f_{in} - k_{psa} \frac{y^2}{2L}$$

$$f_y = f_{in} \frac{y}{L} - k_{psa} \frac{y^3}{2L^2} - k_y y$$
(2.6)

The resulting mechanism force has a strong non-linear relationship with respect to the mechanism displacement, depicted in Fig. 2-5. The singular configuration discussed earlier is expressed in the fact that regardless of the mechanism parameters or the input $u \propto f_{in}$, the mechanism force is always zero when the position is zero.

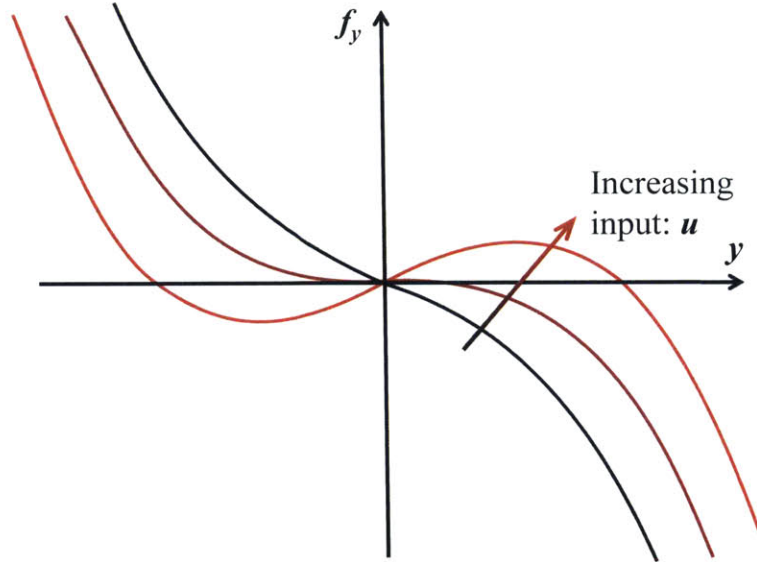


Figure 2-5: A sketch of the amplification mechanism force-displacement relationship. The initial slope increases with the input u . Note the position $y = 0$ is a singular point where the mechanism force f_y is always zero.

Although the non-linear relationship is undesirable for direct application to a load, this mechanism will be used as a unit within a larger structure where many of the difficulties, including the singularity, can be dealt with through proper balancing.

These features will be discussed in the following chapter.

2.2.2 Functional Requirements of the Rotational Joint

The crucial design component of the buckling mechanism is the rotational joint. If designed similar to previous mechanisms there will be a similar tradeoff between the parallel and serial stiffness. [27] However, the joint cannot rely on friction either due to the extremely large forces produced by the PSA would yield large losses. If a joint can be designed so that it doesn't produce frictional losses, nor has a parallel stiffness component, a substantial improvement in transmissibility can be expected without efficiency losses. Furthermore, this joint should have the maximum possible stiffness to minimize a reduction in transmissibility due to a finite serial stiffness. For the moment, the spring connected to the output node with stiffness k_y in Fig. 2-3 is ignored and will be addressed in later sections.

The following design requirements are defined for the rotational joint:

- Amplification: mechanically amplify the piezoelectric stack displacement two orders of magnitude
- Energy efficiency: The mechanical energy transfer loss due to serial compliance and friction should be minimized
- Preload: The system will provide a preload to the PSA with a comparatively low stiffness to increase the mechanical work output per cycle

The proposed design uses a rolling contact joint that effectively eliminates friction and parallel stiffness while maintaining the necessary amplification.

2.3 Rolling Contact Flexure-Free Rotational Joint

Fig. 2-6 shows the basic schematic of a flexure-free, rolling-contact buckling mechanism for PSA displacement amplification. It consists of three major components, aside from the PSAs themselves:

- Caps: workpieces placed at both ends of each PSA
- Output node: a workpiece placed in the middle that is connected directly to the load of the amplification mechanism
- Base: a rigid structure with a curved profile

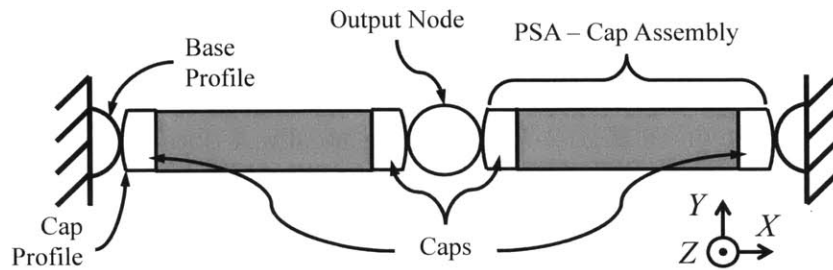


Figure 2-6: A labeled schematic of the rolling contact joint buckling amplification mechanism.

The joint is formed by the contacts maintaining a rolling contact. This buckling mechanism contains four rolling contacts where the caps interact with the base and output node. Not shown in the figure, the output node is constrained to prevent rotation in all 3 axes and translation in X and Z , therefore allowing a single degree of freedom, displacement in Y . As the PSAs are activated, they elongate. As a result, the output node displaces upwards (or downward) and the caps roll without slipping along the base/output node.

The following conditions for the rolling contact surfaces must be met to minimize losses due to friction:

- All the components make only rolling contact
- They do not slide or slip with respect to each other
- The quasi-static contact forces act only in the direction normal to the contacting surfaces.

If the no slip condition is assumed, the mechanism must be symmetric with respect to the centerline upon which the output node moves. The profiles of each pair of

caps on each PSA must be symmetric and have the same curvature. Furthermore, the curvature of the ground profile must be the same as that of the output node. Additional restrictions on the geometry are discussed later to maintain these no slip conditions.

2.3.1 Kinematics of Rolling Contact Joint

Let R be the radius of the base surface as well as the output node surface, and r be that of the cap, as shown in Fig. 2-7. Assuming no slip, I obtain

$$R\xi = -r\vartheta \therefore \vartheta = -\frac{R}{r}\xi \quad (2.7)$$

where $\xi = \angle OAB$ is the ground contact angle, and $\vartheta = \angle PBA$ is the cap contact angle shown in the figure. The tilting angle of the PSA-cap assembly, α , is given by

$$\alpha = \xi - \vartheta, \therefore \alpha = \left(1 + \frac{R}{r}\right) \xi \quad (2.8)$$

Let Δ_0 be the distance between points B and D at rest. At this rest configuration both PSAs, caps, and the output node are aligned, and the PSAs are not activated. As both PSAs elongate, the distance between B and D becomes $\Delta = \Delta_0 + z$. Assuming no slip at the rolling contact points I can obtain the displacement of the output node in the vertical direction. From Fig. 2-7:

$$\begin{aligned} y &= 2(R+r)\sin\xi + \Delta\sin\alpha \\ &= 2r(1+\Gamma)\sin\xi + \Delta\sin[\xi \cdot (1+\Gamma)] \end{aligned} \quad (2.9)$$

where, $\Gamma = R/r$ is the characteristic radius.

Note that, since the output node is constrained to not rotate, the caps rotate symmetrically about the base and output node. Since the distance between points A and O is constrained by the ground structure, the distance from the ground to the

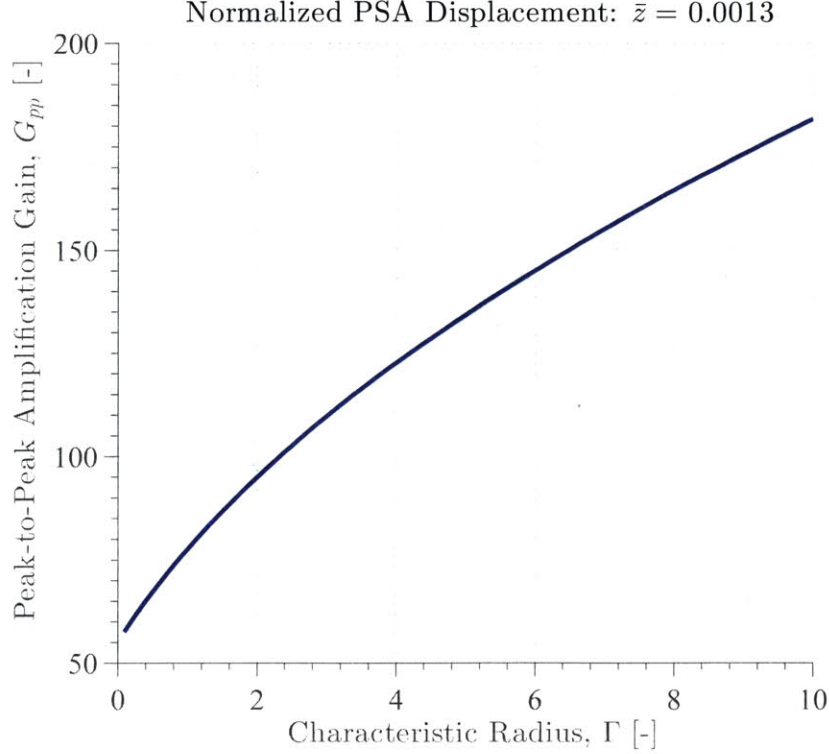


Figure 2-8: This plot relates the peak-to-peak amplification gain of the buckling unit G_{pp} to the characteristic radius Γ where z is held constant at 40 micrometers, the free displacement of the PSA. The cap center distance Δ_0 is zero and the cap profile radius r is 30 millimeters.

In the case $\bar{\Delta}_0 = 0$, a situation explained in greater detail later, the peak-to-peak amplification gains can be simplified to:

$$G_{pp} = \frac{y_{pp}}{z_{max}} = \frac{2y_{max}}{\Delta\lambda} \cong 4\sqrt{\frac{1+\Gamma}{\bar{z}_{max}}} = 4\sqrt{\frac{R+r}{z_{max}}} \quad (2.13)$$

where $\bar{z} \ll 1$. Figure 2-8 shows the plot of the amplification gain against the characteristic radius $\Gamma = R/r$ for a maximum free displacement of a typical PSA (40 micrometers of free displacement and a body length of 40 millimeters), a cap profile radius r of 30 millimeters, and a cap center distance Δ_0 of zero. A wide range of amplification gains can be obtained by tuning the characteristic radius, Γ . A characteristic radius of $\Gamma = 2.3$ produces a peak-to-peak amplification ratio of 100.

Zero Slip Condition

In order to prevent slippage and thus prevent unnecessary losses, friction must be minimized at the contact surfaces. Furthermore, increasing the normal force at the contact joint increases the force necessary to cause slippage. Therefore, the ideal configuration is if, in statics, the contact force is normal to the contact face throughout the entire stroke of the actuator regardless of the output force of the PSA. Provided that the caps and ground/output node profiles are symmetric, this is accomplished by setting Δ_0 to zero. As a force acts at the output node in the Y -direction, internal forces are generated at the four contacting points, two of which are labeled as C and D in Fig. 2-9(b)(c). If the distance Δ is not zero, as illustrated in Fig. 2-9(c), line \overline{CD} is not aligned with the normal of the contacting surfaces, shown as dotted lines. Since the contact force, f_c , acts in the direction of \overline{CD} , it produces a component in the tangential direction. This means that a static frictional force with magnitude $\sin \mu f_c$ acts at both points C and D . In contrast, if both circular surfaces of each cap are concentric, i.e. $\Delta = 0$, the contacting forces are collinear with line \overline{CD} in Fig. 2-9(b) and therefore, no tangential component, i.e. no friction force, is induced. Thus, in order for the mechanism to satisfy all of the functional requirements described above, the caps must be concentric, $\Delta = 0$. Note that due to the contact force, f_c , even a small non-zero displacement, Δ , can cause a large frictional force leading to a reduction of the output performance. Furthermore, in this situation, it is simple to approximate the general amplification mechanism length and angle of rotation in terms of the base/cap radii and the contact angle: $L = 2(R + r)$ and $\Omega = \xi$.

2.3.2 Maximizing Transmissibility

Preload Compensation Springs

A preload is common in mechanical systems to reduce slop, increase stiffness, and maintain contact between surfaces. As motivated already by the work output analysis in Section 2.1, a preload is particularly important in the buckling amplification mechanism. The preload's functional necessity is expanded for the rolling contact

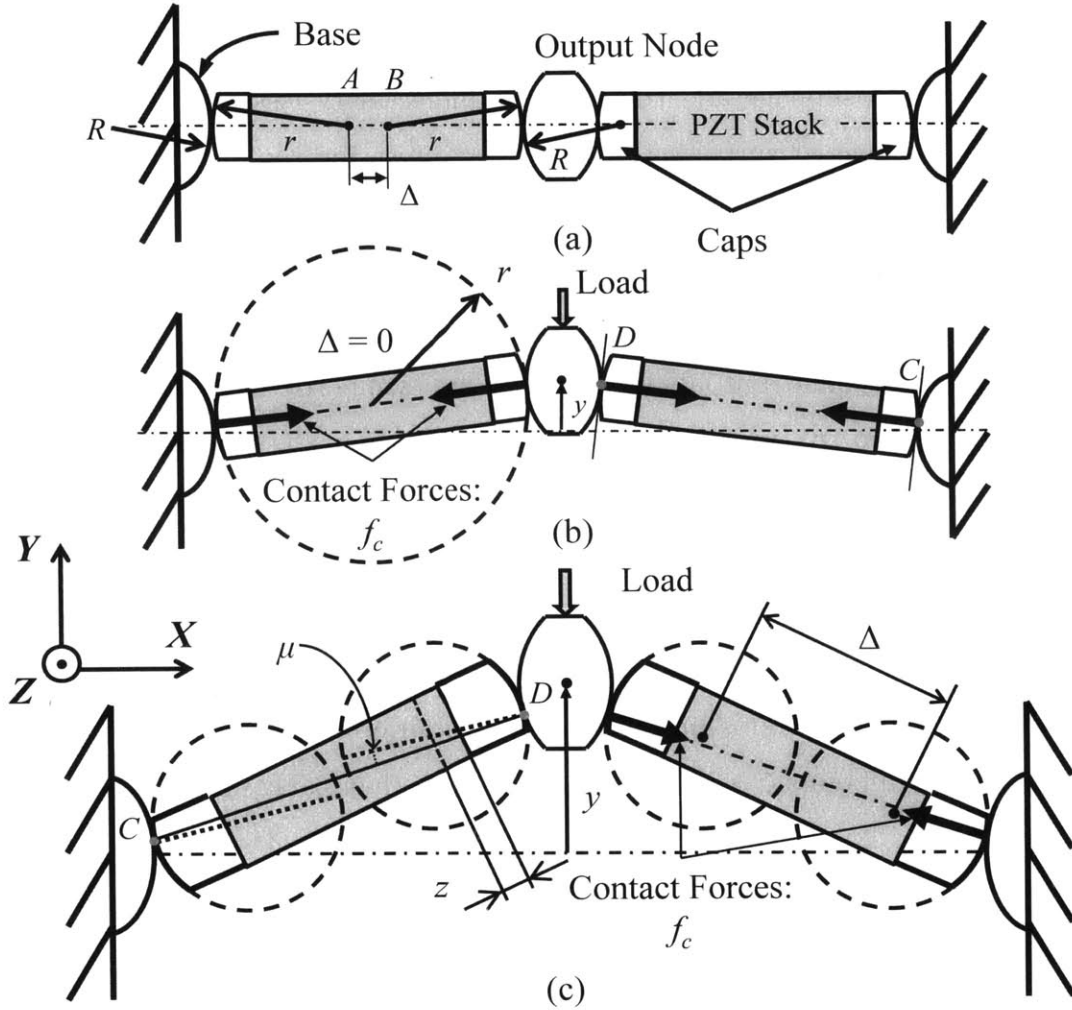


Figure 2-9: A schematic of the rolling contact buckling mechanism. (a) A general rolling contact buckling mechanism at the singular configuration with several parameters labeled, including the cap radius r , the base radius R , and the cap center distance Δ . (b) A special case, $\Delta = 0$ in the displaced configuration showing the alignment of the contact forces f_c and faces of the rolling surface. (c) A non-zero cap center distance $\Delta \neq 0$ that requires a friction force to stay balanced due to the misalignment angle μ .

joint. Due to the fact that a contact force can only be used in compression, a preload force is necessary to maintain contact between the caps and the base/output node.

Figure 2-10 shows an experiment apparatus for verifying the theoretical limit of work output. A shape memory alloy (SMA) wire was wound around the PSA for preloading the stack. To maintain the constant preload despite the extension of the PSA, the stiffness of the wire k_{sma} must be much less than the stiffness of the

PSA k_{psa} . Exploiting the super-elasticity of shape memory alloy I have satisfied this constant preload condition. By holding the PSA between two rigid structures, the force-displacement trajectory of the preloaded PSA has produced nearly the maximum work output.

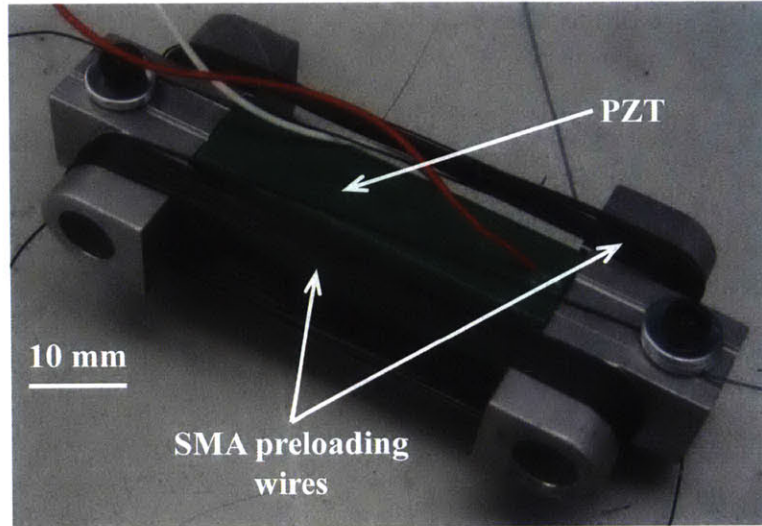


Figure 2-10: A preloaded PSA using shape memory alloy wires with super-elastic properties.

Preloading the PSA utilizing SMA wires is complex and costly. This can be effectively replaced by a simple spring mechanism by exploiting the buckling mechanism. Fig. 2-11 shows a mechanism for applying a preload. One wall of the buckling mechanism is pushed inward to apply a preload larger than or equal to the blocking force while holding the voltage at 0 V. As the preload is applied, an instability is caused at the singular configuration pushing the output node in either vertical direction. As a result, the preload is hardly kept constant as the output node departs the singular position. This problem can be solved effectively by using a simple spring placed at the output node that can apply a constant preload for a broad range of output displacement y . The spring is termed Preload Compensation Springs (PCS).

We first consider the necessary condition for the preload force, f_{pre} , to be constant in the direction of z -axis. As shown in Fig. 2-12, the two preload forces acting from both sides of the PSAs create a force in the Y -direction at the output node:

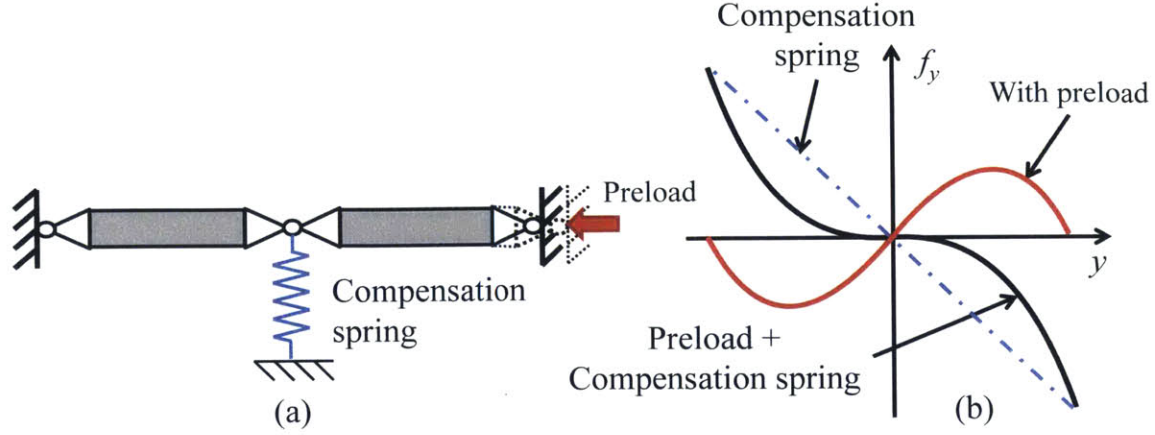


Figure 2-11: The benefit of preload compensation springs (PCS). (a) Shows a simple schematic of the preload process and corresponding stabilizing spring. (b) Shows the equal slope of the initial instability due to preloading and the PCS stiffness at the center position $y = 0$. Note the input u is zero for this example.

$$f_{y,pre} = 2f_{pre} \sin \xi \quad (2.14)$$

where ξ is the angle between the horizontal centerline and the line connecting the two contacting points, as shown in Fig. 2-12. Assuming that the two circles of the cap surface are concentric, $\Delta = 0$, and that the PSA displacement is small, $\frac{z}{L} \ll 1$, the direction of the preload force satisfies the following relationship with y :

$$\tan \xi = \frac{y}{L} \approx \sin \xi \quad (2.15)$$

where $L = 2(R + r)$. Substituting Eq. (2.15) into Eq. (2.14), I find that the preload forces in the y and z directions must satisfy the following functional relationship with output displacement y :

$$f_{y,pre} = \frac{2f_{pre}}{L}y \quad (2.16)$$

Therefore, Eq. (2.6) becomes:

$$f_y = f_{in} \frac{y}{L} - k_{psa} \frac{y^3}{2L^2} - k_y y + \frac{2f_{pre}}{L} y \quad (2.17)$$

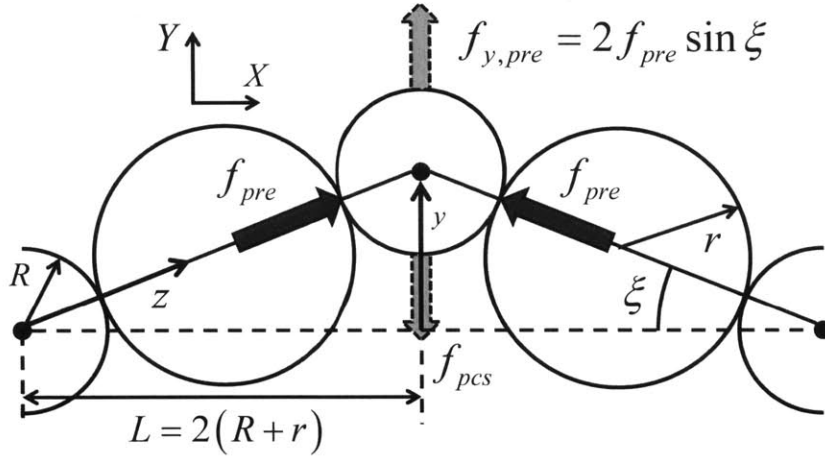


Figure 2-12: A schematic detailing the force balance on the output node based on the constant preload force in the direction of the PSA, f_{pre} , and the PCS force, $f_{pcs} = -k_y y$. Note that the preload force in the y -direction, $f_{y,pre}$, is the summation of the two forces in the z -direction. Furthermore, the $f_{y,pre}$ is exactly balanced by the f_{pcs} .

Note that the preload force f_{pre} must be kept constant, which means that the factors other than the output displacement y in Eq. (2.16) are constant. Defining the constant factors in Eq. (2.16) as a spring constant:

$$k_{pre} \equiv \frac{2f_{pre}}{L} \quad (2.18)$$

Eq. (2.16) reduces to:

$$f_{y,pre} = k_{pre} y \quad (2.19)$$

This implies that a spring of stiffness $k_y = k_{pre}$ placed between the output node

and the center line can generate a constant preload in the z direction for an arbitrary output displacement, y , as long as $\frac{z}{L} \ll 1$. At the singular position where the preload has been set, each PSA experiences the set preload f_{pre} , and the PCS does not affect the PSA stacks since $y = 0$. As the output node deviates from the horizontal centerline, the PCS generates the restoring force $f_{pcs} = k_{pcs}y$. This balances the force generated by the preload, f_{pre} , in the Y -direction, enabling the PSAs to have the constant preload regardless of output displacement y . This is the principle of the preload compensation spring (PCS). The final equation for f_y becomes:

$$f_y = f_{in} \frac{y}{L} - k_{psa} \frac{y^3}{2L^2} - \cancel{k_y y} + \cancel{k_{pre} y} \quad (2.20)$$

As long as the PCS has the matched spring constant $k_y = k_{pre} = \frac{2f_{pre}}{L}$, the singular point at the center becomes a neutrally stable point when the PSAs are held at 0 V. This can be explained graphically in Fig. 2-11(b). The broken line shows the force-displacement characteristics at the output node when the preload alone is applied. Note that the singular point is an unstable equilibrium with the preload alone. In Fig. 2-11(b) the PCS with the matched spring constant is represented by the straight dash-dot line whose slope has the same magnitude as the unstable slope at the singularity but the opposite sign. Superimposing the two forces generated by the PCS (dashed line) and the preloaded buckling mechanism (red line) I find that the singular point is neutrally stable, as shown by the solid curve. Note that the voltage is kept zero in this diagram. As the output node deviates further, the force created by the PCS dominates creating a large negative force, as shown by the solid curve.

The above argument is based on the approximation of the sine and tangent functions given by Eq. (2.15). As the displacement of the output node extends, this approximation may cause some error. As shown in Fig. 2-7, the PSA's motion is more complex for a large displacement; it rotates as well as expands. The following analysis using a potential function provides a rigorous argument, and shows that the

error of the PCS is negligibly small for a wide range of output node displacement y .

The PCS is connected between point E, shown in Fig. 2-7, and ground such that the potential energy, Q_s , stored in the spring is equal to: $Q_s = \frac{1}{2}k_y y^2$. Recall the angle of the PSA α is directly related to the contact angle ξ as defined in Eq. (2.8). The equivalent force, $f_{z,pcs}$, is defined as the force from the PCS along the direction of the PSA. This force can be determined by differentiating the potential energy Q_s with respect to the displacement z . Note that due to the complex geometry it is not trivial to put the output displacement y in terms of the displacement z . So instead, the displacement angle, ξ , is used as an intermediate variable.

$$\begin{aligned}\xi(\varphi) &= L \frac{1 - \cos \xi}{\cos \alpha} \\ y(\varphi) &= L \sin \xi + z(\xi) \sin \alpha\end{aligned}\tag{2.21}$$

By using the chain rule, $f_{z,pcs}$ is given by:

$$\begin{aligned}f_{z,pcs} &= -\frac{\partial Q_s}{\partial z} = -\frac{\partial Q_s}{\partial y} \frac{\partial y}{\partial \xi} \left(\frac{\partial z}{\partial \xi}\right)^{-1} \\ &\approx -k_y L \left[1 - \left(\Gamma + \frac{1}{2}\right) \Gamma \xi^2\right]\end{aligned}\tag{2.22}$$

Over a wide range of characteristic radii, including the characteristic radius used in the implementation described below, the deviation of the preload from its initial value is less than 0.1% over the full range of the buckling amplification mechanism. Considering a preload on the order of the blocking force of the PSA, this corresponds to a normalized parallel stiffness, k'_p on the order of 0.001. Therefore, the complex, bulky, and costly SMA wires can be eliminated. The simple spring can approximate the required restoring force accurately. This result is independent of the specific PSA properties, provided that the maximum strain and Γ are on the order of 0.1% and 1, respectively.

Serial Compliance

With the parallel stiffness effectively removed, the parallel stiffness is essentially removed from the amplification mechanism: $k'_p \approx 0$. Furthermore, the circular rolling

contact may have a much higher stiffness than that of flexures. In flexure design there is a trade-off between the serial and parallel stiffness; a thicker flexure joint yields a stiffer serial spring at a cost of a higher parallel spring stiffness. There is no equivalent conflicting requirement for the rolling contact buckling mechanism. If the parallel stiffness is removed, the transmissibility is given by Eq. (2.2) and shown in Fig. 2-13.

$$\gamma = \frac{k'_s}{k'_s + 1}, \text{ if } k'_p = 0 \quad (2.23)$$

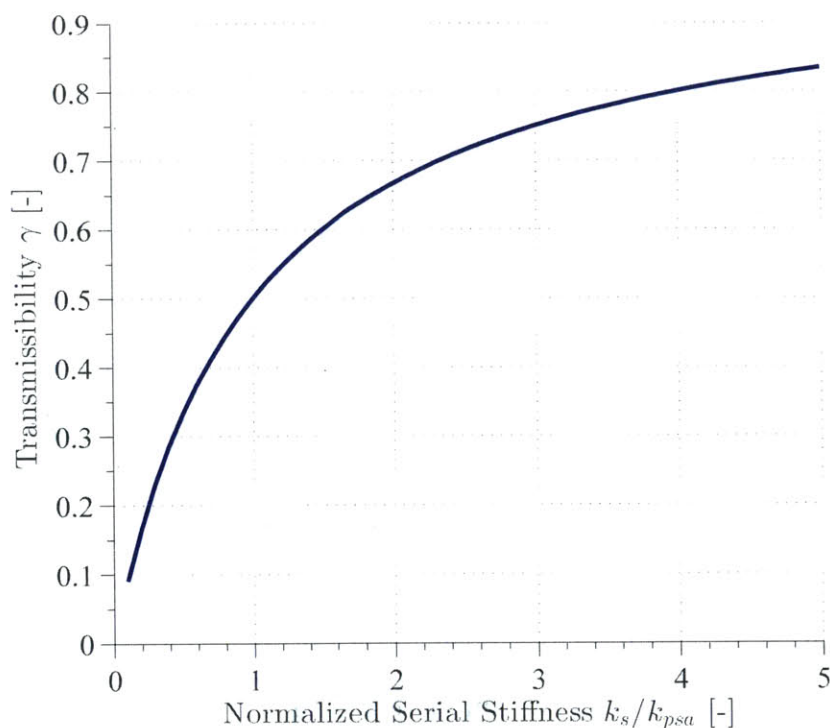


Figure 2-13: A plot of the transmissibility as a function of the normalized serial stiffness. This plot assumes the parallel stiffness is effectively zero.

Note that when $k'_p = 0$, as is the situation described above, the effective PSA force and stiffness in Fig. 2-1(c) can be related to the transmissibility: $f_{eff} \rightarrow \gamma f_{in}$ and $k_{eff} \rightarrow \gamma k_{psa}$. Therefore, the transmissibility not only describes the relationship between the actual work output compared to the ideal scenario, but also linearly scales the effective PSA force output and stiffness.

The serial compliance becomes the driving parameter for controlling the transmissibility. The stiffness of the rolling contact surfaces is determined by the Hertzian contact stress. A higher force between the two surfaces produces more deformation, a larger contact area, and subsequently a greater stiffness. Applying this to the buckling mechanism where two rolling cylinders of the base, output node, and cap profiles are compressed, an estimate of stiffness can be obtained given by Eq. (2.24).[44] In the equation, the radii R^* , elastic moduli E , and Poisson's ratios ν are assumed to be equal for each surface. In addition, k_{joint} is the stiffness of the joint, w is the width of cylinder, ς is the contact length, δ is the relative displacement of the two cylinders, and f_{pre} is the preload force. Figure 2-14 plots the normalized stiffness of the joint as a function of the normalized preload force. The stiffness and force are normalized with respect to the PSA's stiffness and blocking force, respectively.

$$\begin{aligned}
\frac{1}{E^*} &= \frac{2(1-\nu^2)}{E} \\
\varsigma &= \sqrt{\frac{8Rf_{pre}}{\pi w E^*}} \\
\delta &= \frac{f_{pre}}{2wE^*} \left(\frac{2}{3} + 2 \ln \frac{4R}{\varsigma} \right) \\
k_{joint} &= \left(\frac{\partial \delta}{\partial f_{pre}} \right)^{-1}
\end{aligned} \tag{2.24}$$

Because there are two joints for each PSA, one for the base and the output node each, the total serial stiffness is half the joint stiffness. The load at the rolling contact surface changes throughout the stroke of the amplification mechanism, but provided the preload is sufficiently higher than the variation, the joint stiffness can conservatively estimated as constant at it's lowest value. Given the example in Fig. 2-14, if the lowest contact force is half the blocking force, then the expected transmissibility will be 0.67. In implementation, the trade-off for designing the rolling contact joint becomes serial stiffness (which is directly related to transmissibility), amplification gain G_{pp} and the material stress. These factors and more will be covered in a later chapter.

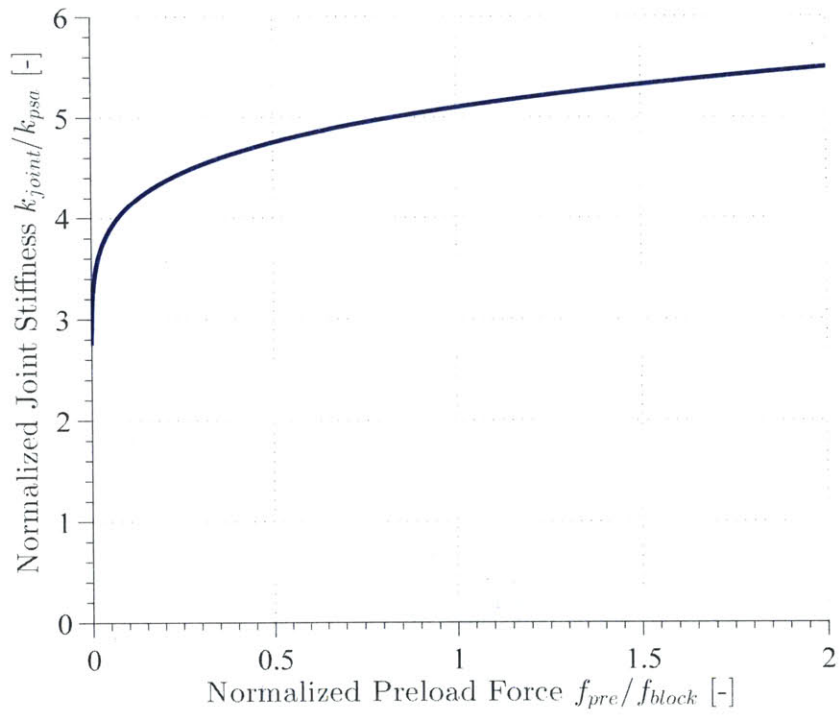


Figure 2-14: A plot showing the normalized joint stiffness as a function of the normalized preload. The stiffness and preload are normalized with respect to the PSA's stiffness and blocking force, respectively. The cap and base material is steel and each profile radius is 25 millimeters.

Chapter 3

Harmonic Poly-Actuator

The objective of this chapter is to introduce the design concept of the “harmonic poly-actuator”, describe and mathematically prove the salient features it has over the buckling amplification mechanism alone and other piezoelectric actuators, and develop unique control algorithms that exploit the physical structure.

3.1 Harmonic Poly-Actuator Concept

Whereas the buckling amplification mechanism has a finite stroke limited mostly by the inherent stiffness of the PSA, the harmonic Poly-Actuator (PA) has no inherent characteristics limiting the stroke. It achieves this through frequency leveraging, the process of converting a cyclic motion, typically along a track, into a large linear stroke or infinite rotary stroke. The harmonic PA consists of several identical amplification units, described in the previous chapter, all acting in parallel on a single output. An individual actuator unit is referred to as a Driving Unit, or simply a Unit, within the PA, shown in Fig. 3-1. In the most general terms, a PA is defined as an actuator that combines several simple units in series, parallel, or both to provide work to a collective output. The vertical arrows indicate the displacement direction of the individual units, whereas the horizontal arrow shows the direction of the PA output. The mechanism that aggregates the forces of individual Units into a single output is referred to as a Parallel Transmission, or simply a Transmission, in this thesis.

The redundant Units provides flexibility when it comes to controlling the output. The goal of the PA is two fold: greatly expand the stroke of the actuator without sacrificing force or backdrivability due to friction; exploit the architecture of the PA to balance the internal forces such that the output force does not depend on position. As an additional benefit, the second point also ensures that all singular points are removed, as the PA can always produce a non-zero force at any position. Both of these goals are achieved due to the cyclic (sinusoidal) waveform of the Transmission, and therefore yield the name “harmonic” poly-actuator.

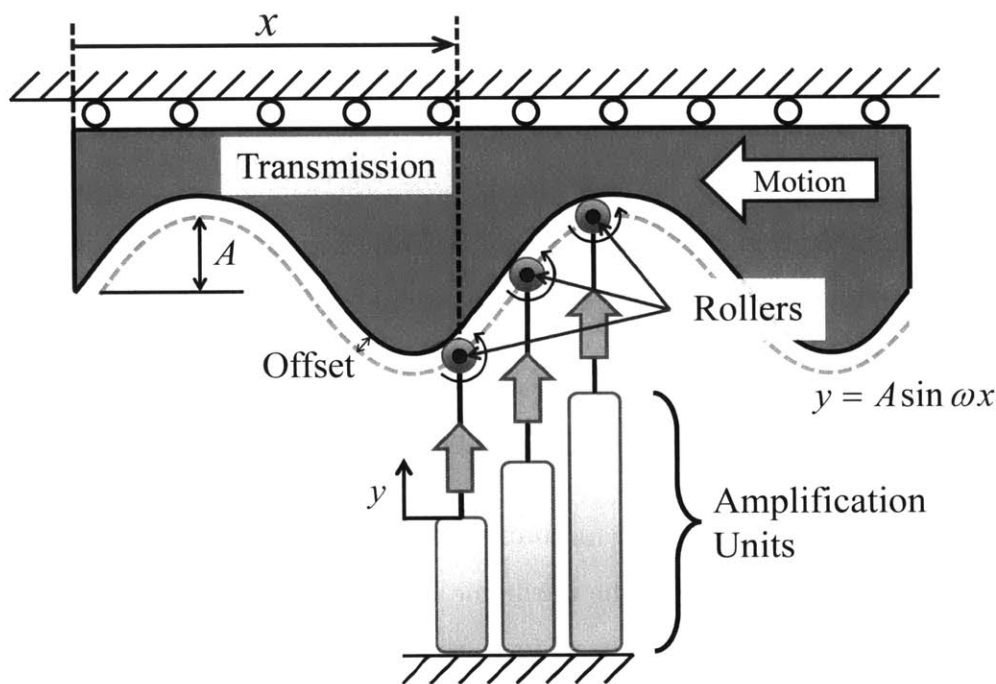


Figure 3-1: This schematic highlights the key features of the harmonic PA: the input Units with displacement y ; the output, or Transmission with position x ; and the interface between the two, including the sinusoidal waveform and the rollers transmitting the force. Note that the Transmission waveform itself is offset from a sinusoid, such that the rollers, and therefore the Units, track a pure sinusoid (the dashed line).

The units are equally spread along the wavelength of the output Transmission. The initial analysis will include the assumption that the Units travel in a sinusoid with amplitude A and spatial frequency ω , although that assumption will be addressed further in a later section. The location of the units is indicated by the position x which is defined from the leading edge of the Transmission to the Unit measured in

millimeters. The position can be directly related to a corresponding phase $\theta = \omega x$, measured in radians. Note that the Transmission waveform itself is offset from a sinusoid by the radius of the rollers. This ensures the displacement of the Units can be related directly to the position of the Transmission: $y = A \sin \omega x$.

3.2 Theoretical Analysis

3.2.1 Formulation of Unit Properties and Output Force

The fundamental property of individual actuator Units is described by force-displacement characteristics:

$$f = g_p(y) + g_d(\dot{y}, \ddot{y}) + g_u(y)u \quad (3.1)$$

where f is the Unit force, y is the Unit displacement with its time derivatives \dot{y} and \ddot{y} and u is the input. The Unit has a input-induced force term $g_u(y)u$ has a displacement dependent coupling function $g_u(y)$ as well as a nonlinear stiffness function $g_p(y)$ and dynamics function $g_d(\dot{y}, \ddot{y})$. All functions are assumed to be smooth and continuous. The dynamics function is linear, whereas the stiffness and input coupling functions are described as finite polynomials:

$$g_p(y) = \sum_{\kappa=0}^m h_{\kappa} y^{\kappa} \quad (3.2a)$$

$$g_d(y) = \beta \dot{y} + \rho \ddot{y} \quad (3.2b)$$

$$g_u(y) = \sum_{q=0}^p \eta_q y^q \quad (3.2c)$$

As will be shown in future sections, the minimum number of Units required to balance the internal forces will be affected by the order of the Taylor series approximations, i.e. m and p in the previous equation. Therefore, it is crucial for proper

operation that the model of the physical properties of the Units be accurate with finite polynomials.

The bandwidth of the Unit, on the order of 50 Hz, is significantly less than that of PSA upwards of 10 kHz, as discussed in previous work. [27] Therefore, it is apt to model the PSA as a spring in parallel with a force source controlled by the input voltage. The force of the i^{th} Unit f_i is transmitted to the output F_i through the sloped surface of the Transmission as opposed to relying on friction as shown in Fig. 3-2.

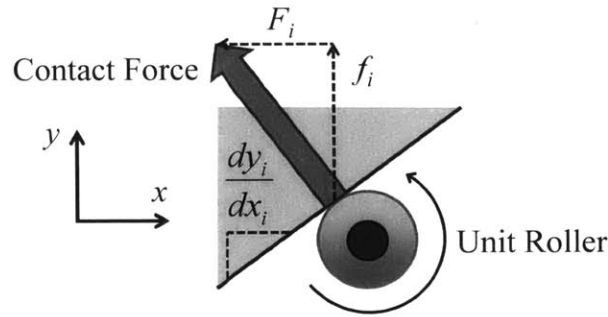


Figure 3-2: A schematic of the force transmission of the i^{th} Unit roller along the slope of the Transmission. The slope and the ratio of the two forces are directly related as defined in Eq. (3.3).

The contribution to the output force from the i^{th} Unit F_i is, therefore a function of the Unit force f_i and the instantaneous slope of the Transmission at the Unit position $\frac{dy_i}{dx_i}$.

$$F_i = -f_i \frac{dy_i}{dx_i} \quad (3.3)$$

Subsequently, the aggregate output force is then given by:

$$F = \sum_{i=1}^n F_i \quad (3.4)$$

In general, the position of the Unit is related to the position of the output by the Transmission function $T(x)$:

$$\begin{aligned}
y &= T(x) \\
\frac{dy}{dx} &= \frac{dT}{dx}
\end{aligned} \tag{3.5}$$

A particular class of Transmission that possesses useful features is a sinusoidal waveform:

$$\begin{aligned}
y &= A \sin \omega x \\
\frac{dy}{dx} &= A\omega \cos \omega x
\end{aligned} \tag{3.6}$$

where A and ω are the amplitude and spatial frequency of the sinusoid, respectively. Let λ be the wavelength of the sinusoid shown in Fig. 3-3. The spatial frequency is then given by $\omega = \frac{2\pi}{\lambda}$. Using the spatial frequency, the location along the sinusoid wavelength is represented by phase angle: $\theta = \omega x$. From Eqs. (3.2), (3.3), (3.6), the i^{th} Unit force is given by:

$$F_i = F_{i,p} + F_{i,d} + F_{i,u} \tag{3.7a}$$

$$F_{i,p} = g_p (A \sin \theta_i) \cdot A\omega \cos \theta_i \tag{3.7b}$$

$$F_{i,d} = g_d \left(A\dot{\theta} \cos \theta_i, -A\omega\ddot{\theta} \sin \theta_i \right) \cdot A\omega \cos \theta_i \tag{3.7c}$$

$$F_{i,u} = g_u (A \sin \theta_i) u_i \cdot A\omega \cos \theta_i \tag{3.7d}$$

where θ_i and u_i are phase position and input of the i^{th} Unit, respectively.

3.2.2 Elimination of the Effect of Non-Linear Stiffness

The PA with a sinusoidal Transmission can possess useful properties if we exploit harmonics by coordinating the multiple Units. Specifically, the forces associated with the nonlinear stiffness of each Unit $g_p(y)$ can be eliminated from the output force. If the n Units are spatially distributed with a particular spacing, the force generated by the nonlinear stiffness of one Unit can be balanced by another Unit. The following

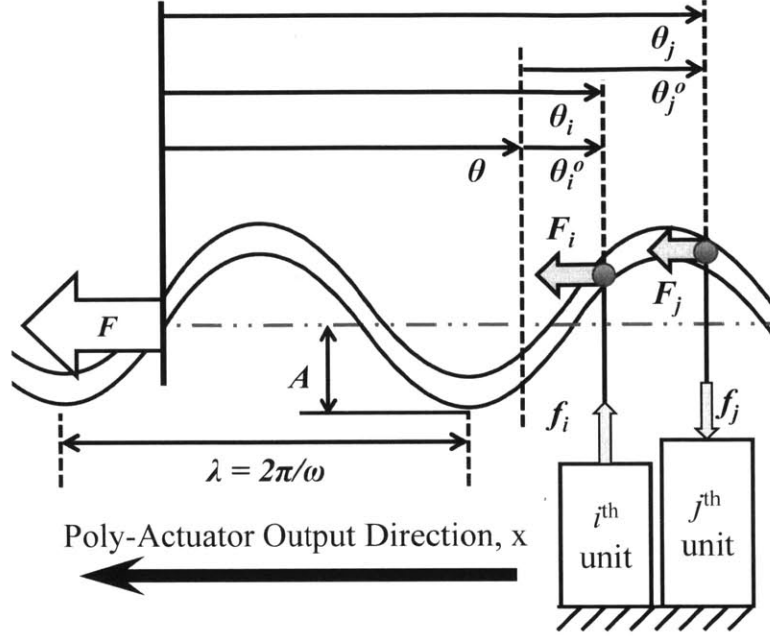


Figure 3-3: A schematic of the force transmission within a general PA architecture. The i^{th} Unit located at $\theta_i = \theta + \theta_i^o$ outputs a force f_i which is transformed by the sinusoidal Transmission to output F_i . The total force F is the sum of the contribution from all n Units. The transmission ratio from f_i to F_i is determined by the location and the geometry of the sinusoid, A and λ .

Proposition describes this useful property.

Proposition 3.2.1 *In the PA described by Eqs. (3.1)-(3.7), the forces associated with the nonlinear stiffness of each Unit balance, so that the output force F does not depend on the internal nonlinear properties of the individual Units:*

$$\sum_{i=1}^n F_{i,p} = 0, \forall \theta \quad (3.8)$$

when the following sufficient conditions are met:

$$\theta_i^o k n = 2\pi, 4\pi, \dots, 0 < k \leq m \quad (3.9)$$

$$\theta_i^o k \neq 0, 2\pi, 4\pi, \dots, 0 < k \leq m \quad (3.10)$$

θ_i^o is the phase position of the i^{th} Unit relative to the position of the output measured

in phase angle, $\theta_i^o = \theta_i - \theta$; as shown in Fig. 3-3.

Proof For the purpose of analysis, it is useful to rewrite the component of a single Unit's nonlinear stiffness transformed to the output direction, $F_{i,p}$ in Eq. (3.7b), as a summation of several harmonics, which allows for convenient analytical methods to be applied. The new expression is equivalent without any loss in generality or requiring any additional assumptions.

$$F_{i,p} = \sum_{\kappa=0}^m h_{\kappa} A^{\kappa+1} \omega \sin^{\kappa} \theta_i \cos \theta_i = \sum_{\kappa=1}^{m+1} [a_{\kappa} \cos \kappa \theta_i + b_{\kappa} \sin \kappa \theta_i] \quad (3.11)$$

where a_{κ} and b_{κ} ($\kappa = 1, \dots, m+1$) are coefficients determined by taking the Fourier transform of $F_{i,p}$. We wish to show that $\sum_{i=1}^n F_{i,p} = 0$ by proving each term in Eq. (3.11) summed over $i = 1, \dots, n$ is equal to zero for all output phase positions θ . For an arbitrary k , replacing θ_i by $\theta + \theta_i^o$ in Eq. (3.11) we attain:

$$\begin{aligned} \sum_{i=1}^n [a_{\kappa} \cos \kappa \theta_i + b_{\kappa} \sin \kappa \theta_i] &= \sum_{i=1}^n [\cos \kappa \theta (a_{\kappa} \cos \kappa \theta_i^o + b_{\kappa} \sin \kappa \theta_i^o)] \\ &+ \sum_{i=1}^n [\sin \kappa \theta (b_{\kappa} \cos \kappa \theta_i^o - a_{\kappa} \sin \kappa \theta_i^o)] \end{aligned} \quad (3.12)$$

Therefore, if $\sum_{i=1}^n e^{j\kappa\theta_i^o} = \sum_{i=1}^n (\cos \kappa \theta_i^o + j \sin \kappa \theta_i^o) = 0$ where j is the imaginary number, then the expression in Eq. (3.12) is zero for all output phase positions θ . If this can be shown for all κ , then $\sum_{i=1}^n F_{i,p} = 0$. If the relative phase position θ_i^o is a linear function with the Unit index i , then the expression can be expanded using a geometric series :

$$\begin{aligned} &\text{If } e^{2\pi j \frac{\kappa}{n}} \neq 1 \\ \sum_{i=1}^n e^{j\kappa\theta_i^o} &= \frac{[1 - (e^{2\pi j \frac{\kappa}{n}})^n] e^{2\pi j \frac{\kappa}{n}}}{1 - e^{2\pi j \frac{\kappa}{n}}} = 0 \end{aligned} \quad (3.13)$$

The conditions Eqs. (3.9) and (3.10) ensure that Eq. (3.13) is always true. then the PA output force F is entirely independent of the nonlinear stiffness term $g_p(y_i)$ and solely relies on the sum of the terms containing the inputs, $\sum F_{i,b}$. ■

Remark A sufficient condition that satisfies both Eqs. (3.9) and (3.10) is:

$$\theta_i^o = 2\pi \frac{i}{n} \quad (3.14a)$$

$$n > m + 1 \quad (3.14b)$$

For the purpose of the analysis in this thesis, these conditions will be assumed for any additional derivations. However, given a specific application, it could be beneficial to deviate from these conditions. For example, the minimum number of Units to balance the nonlinear terms can be significantly reduced if the specifics of the system are exploited. Consider a case where the nonlinear stiffness function $g_p(y)$ is purely an odd function. If so, there is no difference between the output force at an arbitrary position from a single Unit and the output force from a single Unit shifted by π radians: $F_{i,p}(\theta_i) = F_{i,p}(\theta_i + \pi)$. If there are an even number of actuators n and the arrangement is as described in Eq. (3.14a), then each Unit $i > \frac{n}{2}$ has another Unit that always produces exactly the same force. This is equivalent to having half the number of Units over half a cycle:

$$n' = \frac{n}{2} \quad (3.15a)$$

$$\theta_i^o = \pi \frac{i}{n'} \quad (3.15b)$$

Therefore, if $g_p(y)$ is odd, n is even, and the conditions in Eq. (3.14) are satisfied, then (3.15) must also be a balanced configuration.

3.2.3 Transmission of Dynamics

Similar to the stiffness function, the individual dynamic forces of the Units can be balanced and replaced in the model as a single lumped dynamic force.

Proposition 3.2.2 *If the dynamic properties associated with damping, β , and mass, ρ , are linear as defined in Eq. (3.2b) and the arrangement of Units is described by Eq. (3.14a) where the number of Units n is greater than 2, then the output also has linear dynamics associated with an effective damping and mass, B_{eff} and M_{eff} respectively.*

Proof The dynamic force in the direction of the output from a single Unit is defined in Eq. (3.7c). This force can be separated into a contribution from the damping and mass, $F_{i,B}$ and $F_{i,M}$.

$$F_{i,d} = F_{i,B} + F_{i,M} \quad (3.16)$$

$$F_{i,B} = \beta A^2 \omega \dot{\theta} \cos^2 \theta_i = \frac{\beta A^2 \omega}{2} \dot{\theta} (1 + \cos 2\theta_i) \quad (3.17)$$

$$F_{i,M} = \rho A^2 \omega \left(\ddot{\theta} \cos^2 \theta_i - \dot{\theta}^2 \sin \theta_i \cos \theta_i \right) = \frac{\rho A^2 \omega}{2} \left[\ddot{\theta} (1 + \cos 2\theta_i) - \dot{\theta}^2 \sin 2\theta_i \right] \quad (3.18)$$

Note the phase velocity and acceleration, $\dot{\theta} = \omega \dot{x}$ and $\ddot{\theta} = \omega \ddot{x}$, do not have a subscript i because they are the velocity and acceleration of the output and do not depend on the particular Unit. Summing the damping force from a single Unit $F_{i,B}$ and repeating a process similar to the stiffness function, the individual phase positions θ_i can be replaced with the sum of the global and relative phase position $\theta + \theta_i^o$.

$$\begin{aligned} F_B &= \sum_{i=1}^n F_{i,B} = \frac{b A^2 \omega}{2} \dot{\theta} \left(\sum_{i=1}^n 1 + \sum_{i=1}^n \cos 2\theta_i \right) \\ &= \frac{b A^2 \omega}{2} \dot{\theta} \left[n + \cos 2\theta \sum_{i=1}^n \cos 2\theta_i^o - \sin 2\theta \sum_{i=1}^n \sin 2\theta_i^o \right] \end{aligned} \quad (3.19)$$

Given that there are more than two Units $n > 2$ and they are arranged equally along one period of the Transmission Eq. (3.14a), then the terms containing $\cos 2\theta_i^o$ and $\sin 2\theta_i^o$ sum to zero. Therefore, the damping force is:

$$F_B = \frac{b A^2 \omega n}{2} \dot{\theta} = B_{\text{eff}} \dot{\theta} \quad (3.20)$$

Similarly, for the inertial term $F_{i,M}$:

$$\begin{aligned}
F_M &= \sum_{i=1}^n F_{i,M} = \frac{\rho A^2 \omega}{2} \left(\ddot{\theta} \sum_{i=1}^n (1 + \ddot{\theta} \cos 2\theta_i) - \dot{\theta}^2 \sum_{i=1}^n \sin 2\theta_i \right) \\
&= \frac{\rho A^2 \omega}{2} \left[n\ddot{\theta} + (\ddot{\theta} \cos 2\theta - \dot{\theta}^2 \sin 2\theta) \sum_{i=1}^n \cos 2\theta_i^\circ \right. \\
&\quad \left. - (\ddot{\theta} \sin 2\theta + \dot{\theta}^2 \cos 2\theta) \sum_{i=1}^n \sin 2\theta_i^\circ \right]
\end{aligned} \tag{3.21}$$

Once again, the terms containing $\cos 2\theta_i^\circ$ and $\sin 2\theta_i^\circ$ sum to zero given the sufficient conditions, therefore, the inertial force is:

$$F_M = \frac{\rho A^2 \omega n}{2} \ddot{\theta} = M_{\text{eff}} \ddot{\theta} \tag{3.22}$$

■

The elimination of the stiffness function g_p and the passive transmission of the linear dynamic parameters ρ and β suggest the harmonic properties of the output due to several Units placed along the sinusoidal Transmission provides a general architecture for the PA. The harmonic analysis used to model the transmission of force can be extended to a broader class of complicated nonlinearities, including hysteresis, to determine the overall effect on the output. Once a model can be summarized and measured the undesired effects can be addressed through the input as will be shown in subsequent sections.

3.2.4 Single Frequency Sinusoidal Inputs

The equation for output force from a single Unit containing the input terms $F_{i,u}$, Eq. (3.7d), can be expanded to:

$$\begin{aligned}
F_{i,u} &= \left(\sum_{q=0}^p \eta_q A^{q+1} \omega \sin^q \theta_i \cos \theta_i \right) u_i \\
&= \left(\sum_{q=1}^{p+1} [c_q \cos q\theta_i + d_q \sin q\theta_i] \right) u_i
\end{aligned} \tag{3.23}$$

where the coefficients c_q and d_q are given by:

$$c_q = \frac{A\omega}{\pi} \int_0^{2\pi} b(A \sin \tau) \cos \tau \cos q\tau d\tau \quad (3.24a)$$

$$d_q = \frac{A\omega}{\pi} \int_0^{2\pi} b(A \sin \tau) \cos \tau \sin q\tau d\tau \quad (3.24b)$$

The output force associated with the input F_u , i.e. the summation of Eq. (3.23), can then be defined as:

$$F_u = \sum_{i=1}^n \left[u_i \sum_{q=1}^{p+1} [c_q \cos q\theta_i + d_q \sin q\theta_i] \right] \quad (3.25)$$

Replacing θ_i with $\theta + \theta_i^\circ$ yields:

$$F_u = \sum_{q=1}^{p+1} \left[\cos q\theta \sum_{i=1}^n u_i (c_q \cos q\theta_i^\circ + d_q \sin q\theta_i^\circ) + \sin q\theta \sum_{i=1}^n u_i (d_q \cos q\theta_i^\circ - c_q \sin q\theta_i^\circ) \right] \quad (3.26)$$

Each Unit input u_i is multiplied by a term containing the position $\theta = \omega x$, either $\cos q\theta$ or $\sin q\theta$. Furthermore, the series of inputs u_1, \dots, u_n are convoluted with a series of harmonics $\theta_i^\circ, 2\theta_i^\circ, \dots, (p+1)\theta_i^\circ$ through the terms containing $\cos q\theta_i^\circ$ and $\sin q\theta_i^\circ$. Therefore, if the input u_i is constructed as a sinusoidal function of the l^{th} harmonic: $l\theta$ where $1 \leq l \leq p+1$ and there are enough Units n , then the output force F_b does not contain any harmonics other than the l^{th} one.

Proposition 3.2.3 *The Unit inputs are given as phased sample points of the l^{th}*

harmonic function in the following form:

$$u_i = u_i(\theta_i^o) = U_l \cos(l\theta_i^o - \phi_l) \quad (3.27a)$$

$$1 \leq i \leq n \quad (3.27b)$$

$$1 \leq l \leq p + 1 \quad (3.27c)$$

where U_l and ϕ_l are the input amplitude and input phase shift of the l^{th} mode, and θ_i^o is the relative position of the Unit. If two sufficient conditions are met:

$$c_l \neq 0 \text{ or } d_l \neq 0 \quad (3.28)$$

and:

$$n > l + p + 1 \quad (3.29)$$

then the quasi-static output force $F = F_u$ is a sinusoidal function of the same phase angle $l\theta$ and all the other modes vanish:

$$F_u = C \cos(l\theta - \varphi) \quad (3.30)$$

where C and φ are constants determined by the input.

Proof This property relies on the orthogonality of sinusoidal modes [38]. The series of Unit inputs can be written as:

$$u_i = u(\theta_i^o) = \Lambda_s \sin l\theta_i^o + \Lambda_c \cos l\theta_i^o \quad (3.31)$$

where $U_l = \sqrt{\Lambda_s^2 + \Lambda_c^2}$ and $\tan \phi_l = \frac{\Lambda_s}{\Lambda_c}$. Substituting Eq. (3.31) into Eq. (3.26) yields products of $\cos q\theta_i^o$, $\sin q\theta_i^o$ and $\cos l\theta_i^o$, $\sin l\theta_i^o$. The summation of these products over

i becomes zero unless $q = l$ under the condition Eq. (3.29). See Eq. (3.32) for an example.

$$\sum_{i=1}^n \cos q\theta_i^o \cdot \cos l\theta_i^o = \frac{1}{2} \sum_{i=1}^n [\cos (q+l)\theta_i^o + \cos (q-l)\theta_i^o] = \begin{cases} 0 & : q \neq l \\ \frac{n}{2} & : q = l \end{cases} \quad (3.32)$$

Note that Eq. (3.13) was used again given the conditions in Eqs. (3.14a) and (3.29). Substituting these into Eq. (3.26), we obtain:

$$F_u = \frac{n}{2} [\Lambda_c (c_l \cos l\theta + d_l \sin l\theta) + \Lambda_s (d_l \cos l\theta - c_l \sin l\theta)] = C \cos (l\theta - \phi_l) \quad (3.33)$$

where $C = \frac{n}{2} \sqrt{(\Lambda_c c_l + \Lambda_s d_l)^2 + (\Lambda_c d_l - \Lambda_s c_l)^2}$ and $\tan \varphi = \frac{\Lambda_c d_l - \Lambda_s c_l}{\Lambda_c c_l + \Lambda_s d_l}$. ■

We call the input pattern of Eq. (3.27a) “phased sinusoidal inputs.”

Lemma 3.2.4 *The expression for the output force, Eq. (3.33), can be simplified further by recognizing:*

$$\begin{aligned} \text{if } l \text{ is odd} & \Rightarrow d_l = 0 \\ \text{if } l \text{ is even} & \Rightarrow c_l = 0 \end{aligned} \quad (3.34)$$

The output force can, therefore, be described as:

$$F = \begin{cases} \pi c_l (\Lambda_c \cos l\theta - \Lambda_s \sin l\theta) & \text{if } l \text{ is odd} \\ \pi d_l (\Lambda_s \cos l\theta + \Lambda_c \sin l\theta) & \text{if } l \text{ is even} \end{cases} \quad (3.35)$$

Alternatively, in terms of the parameters in Eqs. (3.27a) and (3.30):

$$C = \begin{cases} \frac{n}{2}c_l U_l & \text{if } l \text{ is odd} \\ \frac{n}{2}d_l U_l & \text{if } l \text{ is even} \end{cases} \quad (3.36a)$$

$$\varphi = \begin{cases} -\phi & \text{if } l \text{ is odd} \\ \frac{\pi}{2} - \phi & \text{if } l \text{ is even} \end{cases} \quad (3.36b)$$

3.2.5 Input Null Space

Provided that the l^{th} harmonic input Eq. (3.27a) induces only the l^{th} harmonic output force, we examine the effect of the input harmonics outside $1 \leq l \leq p + 1$. Interestingly, a bias term U_0 as well as higher order harmonics greater than $p + 1$ in the input do not affect the output force.

Proposition 3.2.5 *If $V \leq \lfloor \frac{n}{2} \rfloor$ and the input signal is of the form:*

$$u_{i,V}(\theta_i^o) = \sum_{v=p+2}^V U_v \cos(v\theta_i^o - \phi_v) \quad (3.37)$$

then the output is identically equal to 0 for all positions:

$$F_V(u_{i,V}) = \sum_{q=1}^{p+1} \sum_{i=1}^n [(c_q \cos q\theta + d_q \sin q\theta) \cos q\theta_i^o + (d_q \cos q\theta - c_q \sin q\theta) \sin q\theta_i^o] u_{i,V}(\theta_i^o) = 0, \quad \forall \theta \quad (3.38)$$

Proof Consider the product between the q^{th} term in Eq. (3.38) and the v^{th} term involved in $u_{i,V}(\theta_i^o)$.

$$\begin{aligned}
F_{v,q} &= \sum_{i=1}^n [(c_q \cos q\theta + d_q \sin q\theta) \cos q\theta_i^o \\
&\quad + (d_q \cos q\theta - c_q \sin q\theta) \sin q\theta_i^o] U_v \cos (v\theta_i^o - \phi_v)
\end{aligned} \tag{3.39}$$

Converting the parameters c_q and d_q into amplitude $A_q = \sqrt{c_q^2 + d_q^2}$ and phase $\tan \alpha_q = \frac{c_q}{d_q}$, $\tan \beta_q = \frac{d_q}{-c_q}$ and further converting U_v and ϕ_v into $v_{c,v}$ and $v_{s,v}$ where $U_v = \sqrt{v_{c,v}^2 + v_{s,v}^2}$ and $\tan \phi_v = \frac{v_{s,v}}{v_{c,v}}$, we can rewrite Eq. (3.39) as:

$$\begin{aligned}
F_{v,q} &= A_q \left[v_{c,v} \sin (q\theta + \alpha_q) \sum_{i=1}^n [\cos q\theta_i^o \cos v\theta_i^o] \right. \\
&\quad + v_{s,v} \sin (q\theta + \alpha_q) \sum_{i=1}^n [\cos q\theta_i^o \sin v\theta_i^o] \\
&\quad + v_{c,v} \sin (q\theta + \beta_q) \sum_{i=1}^n [\sin q\theta_i^o \cos v\theta_i^o] \\
&\quad \left. + v_{s,v} \sin (q\theta + \beta_q) \sum_{i=1}^n [\sin q\theta_i^o \sin v\theta_i^o] \right]
\end{aligned} \tag{3.40}$$

It is important to note several properties of q and v . First, q is always less than v due to the definition of the ranges of the summations: $1 \leq q \leq p + 1$ and $p + 2 \leq v \leq V \leq \lfloor \frac{n}{2} \rfloor$. Second, the sum of q and v is always strictly less than n : $q + v < 2V \leq n$. Now, if we take the first summation in Eq. (3.40) and use a trigonometric identity, we obtain the following expression:

$$\sum_{i=1}^n \cos q\theta_i^o \cos v\theta_i^o = \frac{1}{2} \left[\sum_{i=1}^n [\cos ((v - q) \theta_i^o)] + \sum_{i=1}^n [\cos ((v + q) \theta_i^o)] \right] = 0 \tag{3.41}$$

where we used the same properties utilized in Proposition 3.2.1, because $v - q > 0$ and $v + q < n$. Similarly, the other summations in Eq. (3.40) vanish for all v and q . Therefore, F_V is zero for all θ . ■

Remark This property is a mathematical representation of the redundancy within the system. Given that there are a greater number of inputs than outputs, there should be a significant null space within which the input can operate. Furthermore,

exploiting this property, along with superposition i.e. the sum of two inputs yields the sum of their individual outputs, provides us with the freedom to select inputs that generate a specified output force, yet optimize other criteria. This will be further exploited later in Section 3.5.2.

3.3 Force Ripple due to Unit Imbalance

The previous sections assumed that all the Units are identical and assembled perfectly, having no misalignment or offset, along a pure sinusoid, but it is important to analyze the consequences of relaxing these assumptions. If the assumptions are violated, the features of PAs exploiting the harmonic nature can be affected.

3.3.1 Unit Properties

The first assumption considered will be the properties of the Unit. For simplicity, this analysis only considers variation in the coefficients in the nonlinear stiffness function $g_p(y)$, however, the same technique was applied to several other variations and a summary of the results is provided.

Consider a modification to (3.2a):

$$g'_{p,i}(y) = \sum_{\kappa=0}^m h'_{\kappa,i} y^\kappa, \quad h'_{\kappa,i} = h_\kappa + \tilde{h}_{\kappa,i} \quad (3.42)$$

where $\tilde{h}_{\kappa,i}$ is an unknown error within the stiffness parameters that varies with each Unit. Separating the error terms $\tilde{h}_{\kappa,i}$ from the ideal terms h_κ , the deviation of the output force \tilde{F} caused by $\tilde{h}_{\kappa,i}$ can be written as:

$$\tilde{F} = \sum_{i=1}^n \sum_{\kappa=0}^m \tilde{h}_{\kappa,i} y_i^\kappa \frac{dy_i}{dx_i} \quad (3.43)$$

Substituting (3.6) into (3.43) we find:

$$\begin{aligned}
\tilde{F} &= \sum_{i=1}^n \sum_{\kappa=0}^m \tilde{h}_{\kappa,i} A^{\kappa+1} \omega \sin^{\kappa} \theta_i \cos \theta_i = \sum_{i=1}^n \sum_{\kappa=1}^{m+1} \tilde{a}_{\kappa,i} \sin \kappa \theta_i + \tilde{b}_{\kappa,i} \cos \kappa \theta_i \\
&= \sum_{\kappa=1}^{m+1} \left[\tilde{A}_{\kappa} \cos \kappa \theta + \tilde{B}_{\kappa} \sin \kappa \theta \right]
\end{aligned} \tag{3.44}$$

where \tilde{A}_{κ} and \tilde{B}_{κ} are constants given by:

$$\begin{aligned}
\tilde{A}_{\kappa} &= \sum_{i=1}^n \left(\tilde{a}_{\kappa,i} \cos \kappa \theta_i^{\circ} + \tilde{b}_{\kappa,i} \sin \kappa \theta_i^{\circ} \right) \\
\tilde{B}_{\kappa} &= \sum_{i=1}^n \left(\tilde{b}_{\kappa,i} \cos \kappa \theta_i^{\circ} - \tilde{a}_{\kappa,i} \sin \kappa \theta_i^{\circ} \right)
\end{aligned} \tag{3.45}$$

Rearranging the terms \tilde{A}_{κ} and \tilde{B}_{κ} , the total error force can be expressed as a single summation over κ :

$$\tilde{F} = \sum_{\kappa=1}^{m+1} \tilde{C}_{\kappa} \sin(\kappa \theta + \tilde{\varphi}_{\kappa}) \tag{3.46}$$

where $\tilde{C}_{\kappa} = \sqrt{\tilde{A}_{\kappa}^2 + \tilde{B}_{\kappa}^2}$ and $\tan \tilde{\varphi}_{\kappa} = \frac{\tilde{B}_{\kappa}}{\tilde{A}_{\kappa}}$. This shows that any variations within the nonlinear stiffness terms will cause a force ripple that varies with position and can be appropriately modeled as a *finite* order sum of sines function. A similar analysis can be shown for the variations to the input coupling term $g_u(y)$ and alignment errors in vertical y and horizontal x positions. The consequence is less severe for the input coupling function, however, because of the mode selection property described in Proposition 3.2.3. The component of the output force due to the PSAs input, F_u will only express the mode equal to the input mode, l in Eq. (3.27a). Therefore, only variations associated with with the selected mode l can be expressed. All other variations are negated.

In all cases, the resultant force deviation, or force ripple, \tilde{F} , can be expressed as a series of harmonic functions of a finite order: N . Therefore, combining all the force ripples caused by diverse sources of Unit variations, the total force ripple can

be written as:

$$\tilde{F}(\theta) = \sum_{\varpi=1}^N H_{\varpi} \sin(\varpi\theta + \psi_{\varpi}) \quad (3.47)$$

The parameters H_{ϖ} and ψ_{ϖ} may be determined through experiments. Spatial Fourier analysis of measured force ripple provides H_{ϖ} and ψ_{ϖ} , $\varpi = 1, \dots, N$, that represent the aggregate effect of all the Unit variations. In the case of the buckling Unit, h_1 and h_3 are the only non-zero parameters. They are associated with the second, and the second and fourth harmonics respectively, as shown in Fig. 3-4a. In the plot, the amplitude of the FFT is normalized by the maximum output force of the PA. Additional examples of variations including the Unit preload force f_{pre} , the vertical zero position of the Unit y_o , and the relative position of the Unit along the Transmission x_i are shown to enforce the concept. The sum of the contributions from the parameter variations produces a complex ripple whose FFT is shown in Fig. 3-4b.

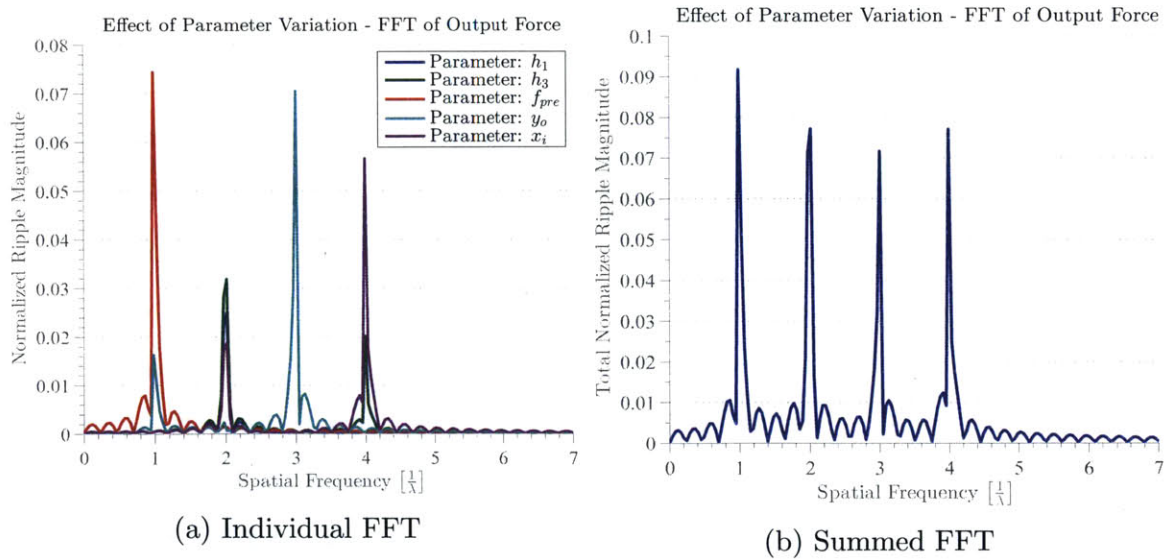


Figure 3-4: An FFT of the output force ripple associated with a few example cases: the linear passive stiffness term in the buckling Unit h_1 ; the cubic passive stiffness term in the buckling Unit h_3 ; the Unit preload force f_{pre} ; the vertical zero position of the Unit y_o ; and the relative position of the Unit along the Transmission x_i .

The precise magnitude of the ripple will vary based on the amount of variation of

a certain parameter from Unit to Unit. In addition, the ripple is more sensitive to certain parameters compared to others. As an example, Fig. 3-5 shows the 1 sigma bound of the average normalized ripple magnitude as a function of a specification of the maximum percentage variation of a given parameter. Comparing Fig. 3-5b to Fig. 3-5a, it is clear that the force ripple is much more sensitive to the positioning of the Unit, which is normalized by the wavelength of the Transmission λ . The variation of the position of the Unit, however, is much easier to control as opposed to the linear stiffness parameter h_1 , which relies on a variety of forces balancing, i.e. the preload force and the PCS stiffness.

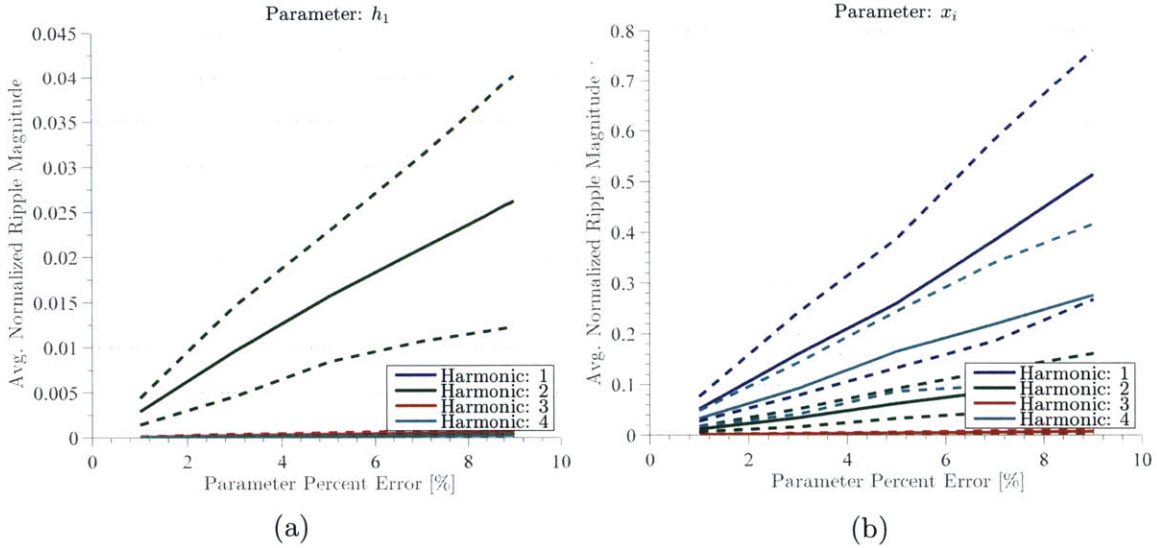


Figure 3-5: Sensitivity of two parameters: (a) the linear term in the buckling Unit force associated with the preload and the PCS h_1 (the provided example case), and (b) the location of the buckling Unit along the Transmission x_i . Note the dashed lines are the 1 sigma bound of the average values.

3.4 Generalization of the Transmission Function

In addition to variation of the properties of the Unit, the assumption that the Transmission function $T(x)$ is a sinusoid, i.e. Eq. (3.6), can be violated with acceptable consequences. The Transmission shape may be changed for a variety of reasons, including a desire to minimize stress at the peaks, for manufacturability, or to produce

additional force output capabilities.

This analysis will show the consequences if the Transmission is instead assumed that the function that defines the vertical displacement of the Unit output $T(x)$ is generally defined as periodic, smooth, and differentiable. Clearly a sinusoid is a subset of this assumption, so it is logical to assume that unlike with the imbalance of Units that there may be a sufficient condition, similar to Eq. (3.14), that does not produce any output force ripple.

Proposition 3.4.1 *If Transmission function $T(x)$ is periodic, smooth, and differentiable; the distribution of the Units satisfies Eq. (3.14a); $T(x)$ can be described as a finite Fourier series with order S and the number of Units satisfies Eq. (3.48)*

$$n > S(m + 1), \quad (3.48)$$

then: the balancing of the passive properties by using Proposition 3.2.1 and superposition is preserved.

Proof The Transmission function $T(x)$ is written as:

$$\begin{aligned} T(x) &= \sum_{j=1}^S A_j \sin(j\omega x + \phi_j) \\ T'(x) &= \frac{dy}{dx} = \sum_{j=1}^S A_j j\omega \cos(j\omega x + \phi_\kappa) \end{aligned} \quad (3.49)$$

Therefore, the passive static Unit force in the direction of the PA output is:

$$\begin{aligned} F_{i,p} &= \sum_{\kappa=0}^m \sum_{j=1}^S h_\kappa A_j^{\kappa+1} j\omega \sin^\kappa(j\theta_i + \phi_j) \cos(j\theta_i + \phi_j) \\ &= \sum_{\kappa=1}^{m+1} \sum_{j=1}^S [a_{\kappa,j} \cos \kappa j\theta_i + b_{\kappa,j} \sin \kappa j\theta_i] \end{aligned} \quad (3.50)$$

As was shown in Proposition 3.2.1, the sufficient number of Units required to ensure balancing must be greater than the highest frequency witnessed in the output

force, which in this case is equal to $S(m + 1)$. Therefore, Eq. (3.48) is a sufficient condition. ■

This result suggests that as the Transmission function Fourier series order becomes very large, i.e. $S \rightarrow \infty$, an extremely large number of Units are required. Therefore, if the sufficient condition Eq. (3.48) is violated, then a force ripple will be produced. Magnitude and frequencies of the ripple will be directly correlated with the magnitude of Fourier transform of the product of the Transmission function and its derivative: $\mathcal{F}\{TT'\}$. All frequencies greater than the number of Units n will be expressed in the output.

3.5 Control Synthesis

I have developed two methods to control the PA with algorithms determined by the measurement of the position of the Transmission. The trade-off between the two methods is cost—monetary, size, weight—and precision. On-Off control, as the name suggests, applies either the saturated voltage or 0 Volts to each Unit based on their relative position along the track. Whereas continuous control uses a linear amplifier to have unique voltage for each Unit. The control methods are essentially independent of the mechanical design and structure, allowing the same mechanism to be controlled with either method depending on constraints.

Utilizing On-Off control is significantly cheaper when considering the electronics. Switching amplifiers can be up to 20 times smaller compared to a linear amplifier of similar power required for continuous control. This affects the cost and weight of the overall system. In addition, there are some techniques to recover stored electrical energy on the charged PSAs by transmitting the energy onto capacitors [6] or other PSAs [3].

However, without the ability to continuously control each individual unit, the algorithms described in Section 3.2.4 are impossible to implement. The conclusions from the analysis from that section can inform the development of the On-Off control to optimize its effectiveness, but there will always be a force ripple for a non-zero

output. Without the fine control resolution of the output force accurate positioning, stiffness control, and precise force control are not possible.

3.5.1 On-Off Control Timing

The Units and Transmission can be aptly compared to a combustion engine in several ways. First, the stroke of the piston/Unit has a fixed amplitude defined completely by the mechanical kinematics and thus, the speed is directly related to the frequency of the piston/Unit. Second, the control technique is bang-bang (literally in the case of combustion engines) and therefore dominated by the timing. Finally, the pistons/Units are phased with each other to overcome the down-stroke/singularities.

For this analysis, solely pure On-Off control is considered, i.e. normalized inputs of $u_i = 0$ or $u_i = 1$, but it is possible to have an amplifier use a small number of discrete voltage levels. This would allow higher efficiency compared to the linear amplifier but provide a smoother output compared to this example case. A force ripple is always present with On-Off control because the input signal is a square wave which has an infinite number of harmonics. The higher order input harmonics that violate the input condition described in Eq. (3.29) in Proposition 3.2.3 are not properly balanced and create a force ripple. For a large number of PSA units, $n \gg 1$, On-Off control can generate lower relative levels of ripple because the larger n means the larger input harmonics l are properly balanced. The magnitude of higher order harmonics of a square wave decay, therefore, the force ripple is smaller. However, this is an impractical method of achieving acceptable force control. For a smaller number of units, the output force resolution is inevitably limited.

Average Output Force Control

To achieve a non-zero output force while constrained to only On-Off control of the individual units, there are two control variables: the charging phase, θ_c ; and the discharging phase, θ_d , shown in Fig. 3-6.

Note that the Units charge and discharge twice a Transmission period λ for the

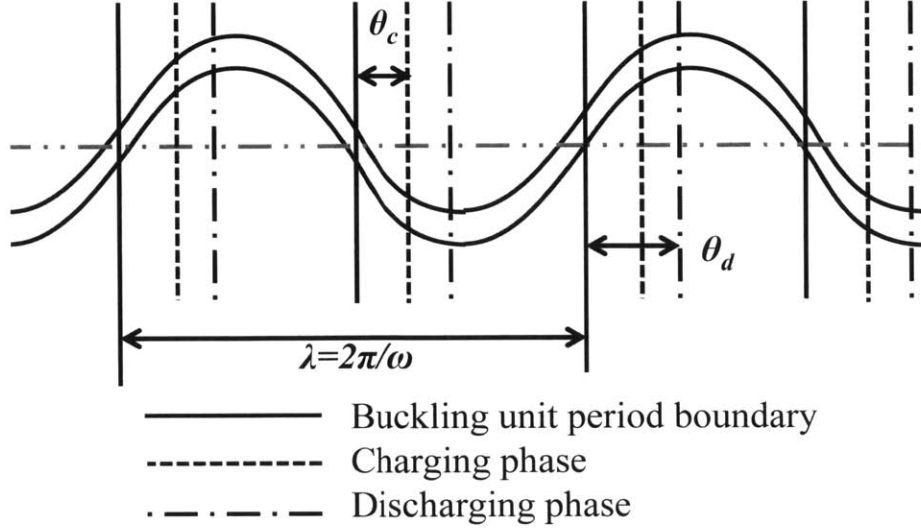


Figure 3-6: A schematic showing the control timing with respect to the Transmission for charging θ_c (dashed) and discharging θ_d (dot-dash).

same reason the input mode l is 2 in the previous section, the input is expressed solely in the second mode.

Unlike the continuous case, the instantaneous PA output force, F , varies with the phase position, θ . However, the control timing can be evaluated based on the average PA output force \check{F} , averaged over one cycle, and the force ripple F_{rms} , measured as the RMS of the force over one cycle. The average force is calculated by integrating the force over one cycle and dividing by the displacement of one cycle, as shown below, where u_{max} is the ON input magnitude.

$$\begin{aligned}
 \check{F} &= \sum_{i=1}^n \frac{1}{2\pi} \int_0^{2\pi} F_i d\theta_i = \frac{n}{2\pi} \int_0^{2\pi} d_2 u(\theta) \sin \theta d\theta \\
 &= \frac{nd_2 u_{max}}{2\pi} [\cos \theta_c - \cos \theta_d]
 \end{aligned} \tag{3.51}$$

With the two independent inputs, θ_c and θ_d , a continuous range of average PA output forces, \check{F} , is possible. As Fig. 3-7 shows, with the exception of the peak force, there are contours within the θ_c - θ_d plane that produce a constant average output force due to the redundancy in the system. Along these contours, the particular force profile can vary significantly and deciding which particular control input is determined

by other desired characteristics, such as the RMS value of the force deviation, the peak or minimum force, or the total phase charged.

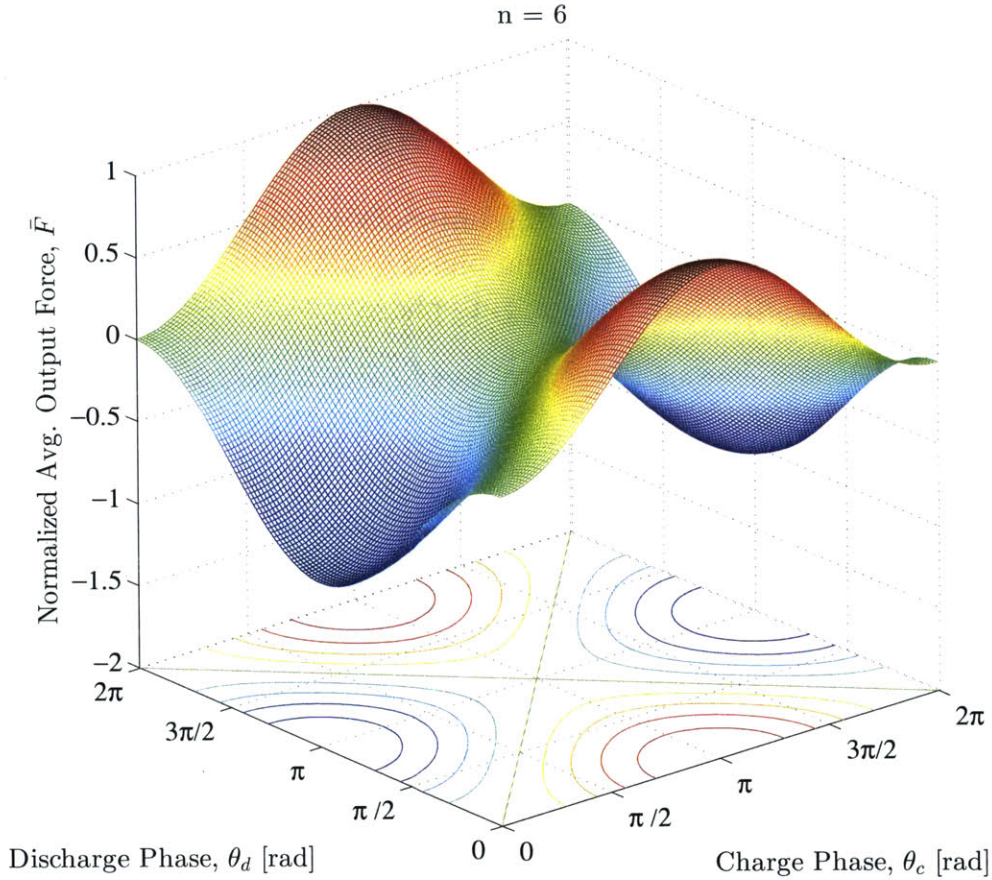


Figure 3-7: A smooth surface showing the average PA output force as a function of both the charge and discharge phase. Note the plot is symmetric as the actuator has no preferred direction. Furthermore, the contours on the θ_c - θ_d plane show lines of constant average output force.

A closed form solution for the force ripple, F_{rms} , cannot be explicitly solved for but it can be defined as the RMS deviation from the average force, \check{F} :

$$F_{rms} \triangleq \sqrt{\frac{1}{2\pi} \int_0^{2\pi} [F_X(\varphi) - \check{F}_X]^2 d\varphi} \quad (3.52)$$

3.5.2 Continuous Control

Passive Force and Stiffness Properties of the Poly-Actuator Output

As discussed in Proposition 3.2.3, when constant inputs, defined by (3.27a), are applied to the n individual Units, the resultant force F is given by (3.30), which varies depending on the position θ , shown in Fig. 3-8.

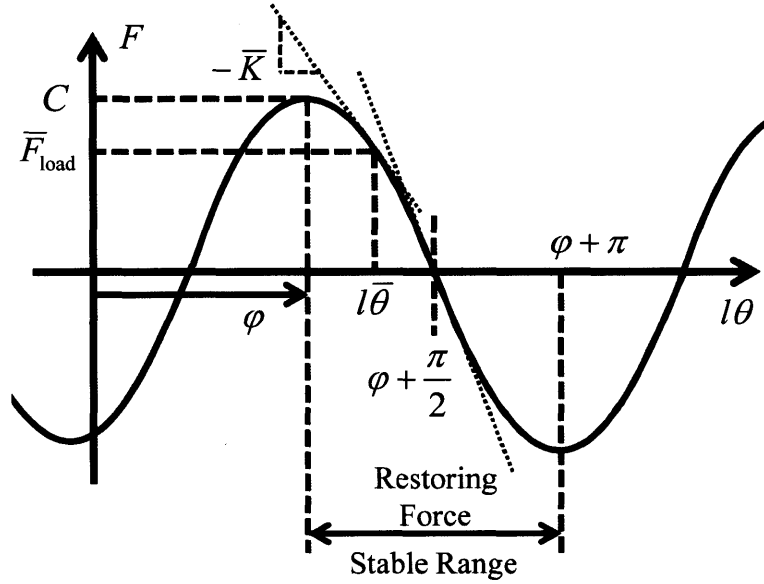


Figure 3-8: The output force-displacement profile given the input defined in (3.27a). The parameters C and φ are input control parameters. Note the stable regime surrounding the equilibrium point at $\varphi + \frac{\pi}{2}$ is a passive property that does not require any measurement or active control. Furthermore, if the PA is loaded by amount \bar{F}_{load} the input can be used to tune the stiffness \bar{K} at the shifted equilibrium point $l\bar{\theta}$.

If no external force acts on the output rod, the PA is in equilibrium at $l\theta = \varphi \pm \frac{\pi}{2}$, where the output force is zero. Note that the equilibrium at $l\theta = \varphi + \frac{\pi}{2}$ is a stable equilibrium, while the one at $l\theta = \varphi - \frac{\pi}{2}$ is unstable. A restoring force acts when the position deviates from the stable equilibrium, as long as the deviation is within the region of attraction: $\varphi < l\theta < \varphi + \pi$. The PA is *passively stable* without feedback or any active controls within this region. Stiffness can be defined as the rate of change in the restoring force to the positional deviation.

$$K = -\frac{dF}{dx} = C\omega l \sin(l\theta - \varphi) \quad (3.53)$$

See Fig. 3-8. Suppose that we want to make a specified position $l\bar{\theta}$ a stable equilibrium with a desired stiffness \bar{K} . From (3.53):

$$\varphi = l\bar{\theta} - \frac{\pi}{2} \quad (3.54a)$$

$$C = \frac{\bar{K}}{\omega l} \quad (3.54b)$$

Substituting these into (3.36) yields the input magnitude U_l and phase ϕ that creates a stable equilibrium with stiffness \bar{K} at the position $l\bar{\theta}$.

In the case a constant load \bar{F}_{load} must be borne at $l\bar{\theta}$:

$$\bar{F}_{\text{load}} = C \cos(l\bar{\theta} - \varphi) \quad (3.55)$$

with a desired stiffness \bar{K} , the parameters C and φ can be found by solving (3.53) and (3.55).

$$\varphi = l\bar{\theta} + \tan^{-1}\left(\frac{\bar{K}}{\bar{F}_{\text{load}}\omega l}\right) \quad (3.56a)$$

$$C = \frac{\bar{F}_{\text{load}}}{\cos(l\bar{\theta} - \varphi)} \quad (3.56b)$$

Note that, since the constant input function (3.27a) contains two parameters, U_l and α , which determine C and φ , the PA can generate both desired force \bar{F}_{load} and desired stiffness \bar{K} at a specified position $l\bar{\theta}$. Note, however, that the magnitude C is bounded $C \leq C_{\text{max}}$, and therefore so are \bar{F}_{load} and \bar{K} .

Input Shaping Exploiting the Null Space

The redundancy addressed in Proposition 3.2.5 can be exploited to generate a given output force while optimizing other criteria, such as the total electrical energy. Let

$J = \sum_{i=1}^n u_i^2$ be a metric of the total electrical energy stored in the n Units. Higher order terms given by (3.37) can be superimposed together with a constant term to the input command (3.27a).

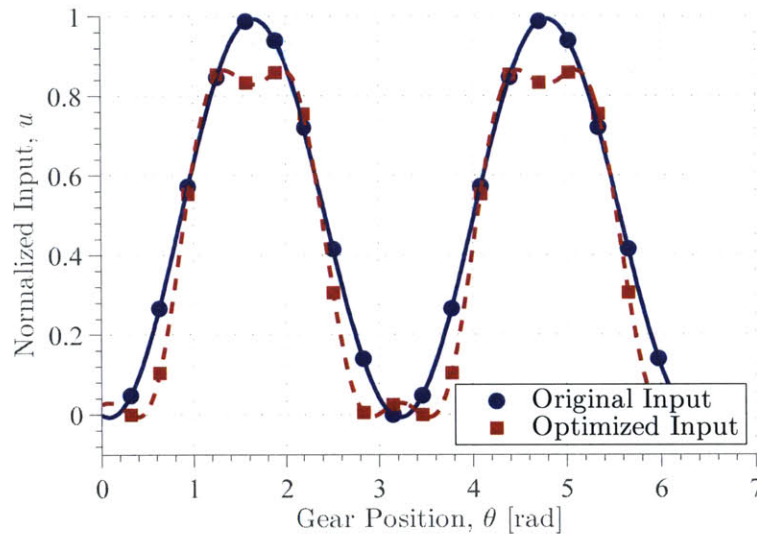


Figure 3-9: A plot showing two signals that both produce the same output. First, a sample input signal (solid line) utilizing the second mode of a system with 20 Units. Second, a signal (dashed line) minimizing the sum of the squared inputs that combines the original with a sixth order signal.

Fig. 3-9 illustrates how the redundancy can be exploited to find an optimal input that minimizes the electrical energy. Here we consider a case where $p < 4$, $d_2 \neq 0$, and $n = 20$. The solid curve indicates the inputs generated with one sinusoid of $l = 2$, i.e. the second harmonic. Superposing another spatial frequency component, e.g. the sixth harmonic, $v = 6$, onto the second harmonic, we can generate a different input pattern that produces the same output force. The magnitude and phase of the sixth mode are free parameters that can be varied to minimize the electrical energy. The broken line in Fig. 3-9 is the optimal input curve that minimizes this electrical energy. Note that the peak value is significantly lowered. This configuration is able to reduce the stored electrical energy by 15%.

Force Control

Force control, in general, aims to generate a reference force regardless of the position and velocity of the system. Here we aim to synthesize a force control system to achieve this goal effectively by considering two issues. One is to generate the desired force \bar{F} efficiently. Fig. 3-8 indicates that the maximum amplitude of force for a given input is generated at $l\theta - \varphi = 0, \pi$ or $\varphi = l\theta, l\theta + \pi$. At these points, the magnitude of the input command is:

$$U_l = \begin{cases} \frac{2\bar{F}}{nc_l}, & l \text{ is odd} \\ \frac{2\bar{F}}{nd_l}, & l \text{ is even} \end{cases} \quad (3.57)$$

The second point is that, since the output force in Eq. (3.30) varies depending on θ , the input command Eq. (3.27a) must be varied to compensate for the change. This requires a measurement of the current position $\hat{\theta}$, and varies the input as:

$$u_i(\theta_i^o, \hat{\theta}) = \begin{cases} \frac{2\bar{F}}{nc_l} \cos(l(\theta_i^o + \hat{\theta})) & l \text{ is odd} \\ \frac{2\bar{F}}{nd_l} \cos(l(\theta_i^o + \hat{\theta}) - \frac{\pi}{2}) & l \text{ is even} \end{cases} \quad (3.58)$$

Substituting Eq. (3.58) into Eq. (3.30) yields the constant output force that was specified: \bar{F} . An important feature of the above force control is that at the peak force position $l\theta^* - \varphi = 0, \pi$, the stiffness is zero: $\frac{dF}{d\theta}|_{\theta^*} = 0$, which implies that the sensitivity of the output force to positional deviation is minimized. In other words, although the measurement of $\hat{\theta}$ is inaccurate; or the compensation for the output force due to the positional change is not accurate, their effects upon the output force is small.

It should be noted that this control method does not close the loop around force. Instead, it is a feed-forward controller based on modeled or measured properties of the PA and a measurement of the position $\hat{\theta}$. Trivially, the loop can be closed around position or force, given the necessary measurement and classic control techniques.

Chapter 4

Implementation

This chapter highlights design concepts not necessary for the theoretical function of the amplification mechanism and the PA, but rather the specific implementations developed for the fabricated prototypes. This includes two buckling amplification mechanisms, a proof-of concept Unit and a Unit for use within the PA, and one PA prototype. In addition to the specifics of the fabricated prototypes, this chapter features the key design trade-offs that must be considered when optimizing the parameters of the Unit and PA. In conclusion, it discusses the setup of a dynamic simulation. This was used to further explore the capabilities of the PA beyond the capabilities of the physical prototype. This provided insight to enable a comparison between the PA and other typical actuators.

4.1 Buckling Amplification Unit

4.1.1 Proof-of-Concept Unit

The design concept of the flexure-free, rolling-contact buckling mechanism was initially implemented on the prototype test bed shown in Fig. 4-1. Table 4.1 summarizes the major specifications of the prototype. The prototype consists of a pair of PSAs encased by end caps in contact with the output node, and a pair of base blocks. All of these elements are aligned with the horizontal centerline at rest. Two sets of slotted

beam structure $ABCD$, having a tuned stiffness along the Y -axis, serve as the PCS. As point C is pushed away from point A , the beams are deformed to a rhombus-like shape: the restoring force vs. y displacement gives the spring constant. A rod attached to the output node is inserted through a clearance hole at A , and is fixed to C . This PCS mechanism plays dual roles. One is to constrain the output node so that it may not rotate about the X , Y and Z , axes as well as restrict translation in the directions perpendicular to the Y -axis. The second is to provide the tuned spring constant so that the middle position ($y = 0$) is neutrally stable, as discussed in the previous section.

Adjustment is a key feature of this prototype. A preload adjustment mechanism with load cells is attached at each end. After adjusting the preload, the base blocks are secured with the clamps shown in the figure. The preload of both PSAs can be adjusted and measured individually before being clamped. In addition, deviation of the base/output node profiles from the X -axis results in a bias force in the output (Y) direction which can be finely adjusted by the PCS clamping nuts.

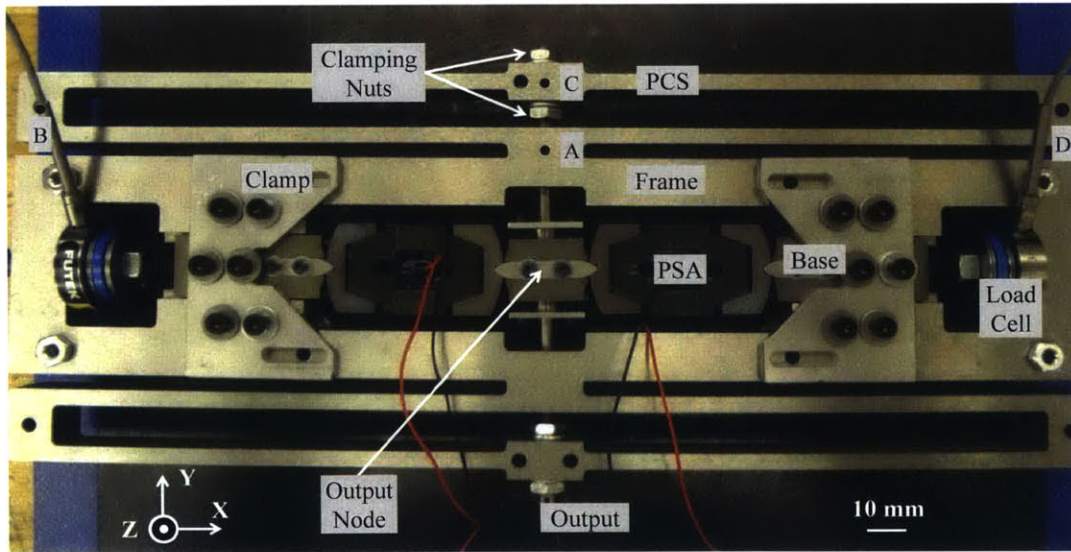


Figure 4-1: Test bed of the high-gain, rolling-contact PSA buckling amplification mechanism.

To prevent the caps from slipping relative to the output node and base, a slip prevention mechanism was devised by using a gear tooth meshed with a low clearance slot as shown in Fig. 4-2. Any slip in the u -direction between the cap and the ground

Table 4.1: Tabulated parameters for the prototype shown in Fig. 4-1

Piezoelectric Stack Actuator (PSA)		
Length	36	<i>mm</i>
Free Displacement, z_{free}	42	μm
Blocking Force, f_{block}	5250	<i>N</i>
Stiffness, k_{psa}	125	$\frac{kN}{mm}$
Piezoelectric Constant	30	$\frac{N}{V}$
Maximum Voltage	150	<i>V</i>
Mass, ρ_p	0.034	<i>kg</i>
Rolling Contact Amplification Mechanism		
Material	D2 Tool Steel	—
Young's Modulus	210	<i>GPa</i>
Cap Radius, r	25	<i>mm</i>
Cap Crowning Radius	100	<i>mm</i>
Output Node Radius, R	12.5	<i>mm</i>
Output Node Crowning Radius	-120	<i>mm</i>
PCS Stiffness, k_{PCS}	150	$\frac{N}{mm}$
Preload Force, f_{pre}	5600	<i>N</i>
Buckling Mechanism Mass, M_{unit}	1.86	<i>kg</i>

block is prevented by a tooth on the ground block inserted into a slot of the cap. Note that the large PSA force does not act on the gear tooth in the v -direction, since the PZT force is borne at the rolling contact area. A small gap between the tooth and the slot relieves the large PZT force. If the cap starts to slip in the u -direction relative to the ground block, the tooth may contact the wall of the slot to prevent further slipping. A pair of the slip prevention mechanisms (i.e. gear teeth) are stationed at both upper and bottom surfaces of each cap and base, so that a rotational misalignment about the v -axis in the figure is prevented as well.

Practically the only factor that determines the transmissibility is the relative serial stiffness. According to Eq. (2.23), the serial stiffness must be twice larger than that of the PSA in order to attain a transmissibility of 60%, and four times larger for transmissibility of 80%. The most significant cause of compliance is the rolling contact

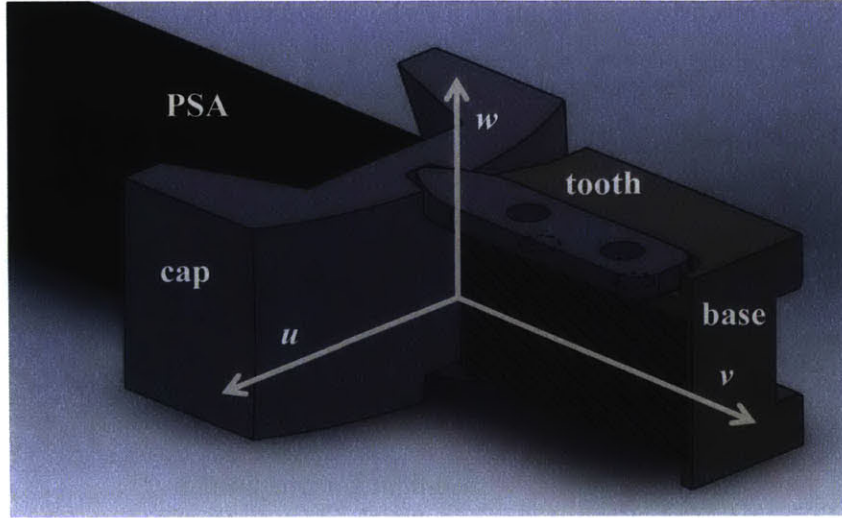


Figure 4-2: A labeled diagram of the cap-base profile contact. To avoid friction, there is a designed gap between the gear tooth and the slot on the cap. Ideally, the gear is used only for alignment during assembly and as a failsafe mechanism.

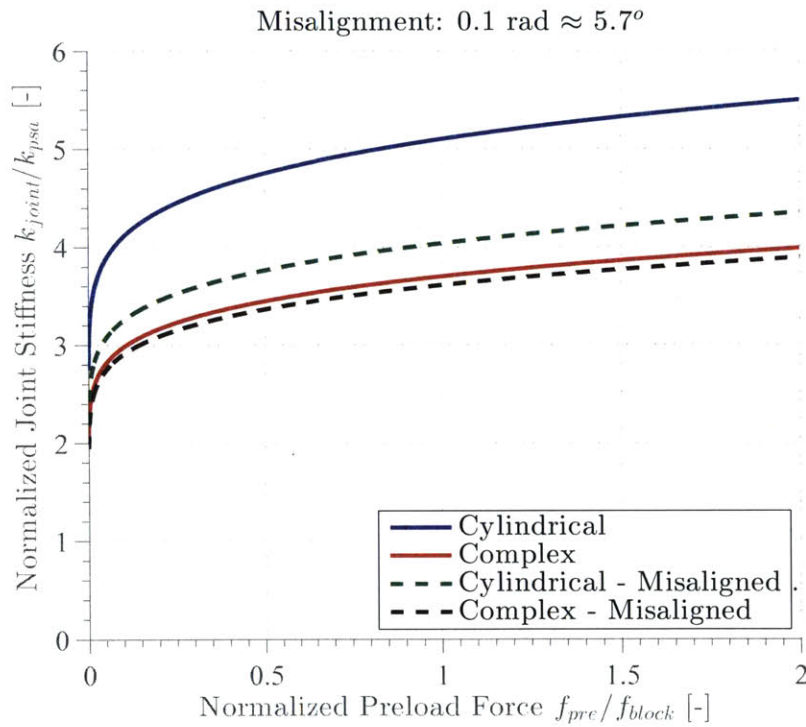


Figure 4-3: A plot showing the nonlinear Hertzian contact stiffness for the cylindrical and crowned caps. Note the large change in stiffness due to an angular misalignment when the caps are cylindrical.

joints. The transmissibility is directly proportional to the effective parameters of the PSA k_{eff} and f_{eff} . As discussed in Sec. 3.3, variation of the buckling amplification

mechanism or PSA from Unit to Unit causes a force ripple in the PA output. The gear tooth works well to prevent large rotations in the v -axis, but even small variations can cause issues in serial stiffness as shown in Fig. 4-3. The plot shows the stiffness of a single rolling contact similar to Fig. 2-13, however it considers a few additional scenarios: a misalignment in rotation about the v -axis by 0.1 radians; and, crowning the cylindrical caps so they become complex curvatures as shown in Fig. 4-4.

Although the stiffness is higher when the caps are cylindrical there are two drawbacks. The first drawback is that a stress concentration may occur near the edges of the cylinders if the two blocks are misaligned about the u -axis in Fig. 4-2. This is a common problem in bearing/gear surface contact and is overcome via crowning, a complex curvature that allows a slight misalignment. The other drawback is that the stiffness is very sensitive to the rotation about the v -axis due to cylindrical surfaces rotating relative to each other. This sensitivity would directly influence the force ripple at the PA output. With crowned surfaces the contact stiffness reduces, as shown in Fig. 4-3, however the crowned surfaces have a considerably lower sensitivity to misalignment. The stiffness varies by less than 5% for a misalignment of 0.1 radian about the v -axis.

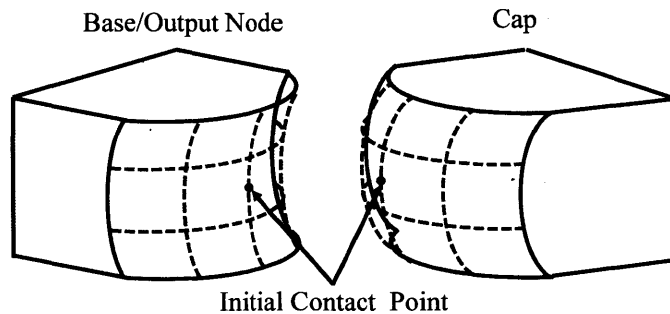


Figure 4-4: A simple schematic highlighting the crowning on both the cap and the base profiles. Note the concave crown radius of the base is larger than the convex crown radius of the cap.

4.1.2 Poly-Actuator Buckling Unit

The buckling amplification Unit implemented in the PA significantly improved upon the proof-of-concept prototype. The Unit, shown in Fig. 4-5, is substantially smaller

in both size and weight. In Fig. 4-5(a) the size of the PA Unit is compared to the proof-of-concept prototype. In Fig. 4-5(b) the new design features are highlighted, including a much smaller simpler PCS and a carbon fiber reinforced plastic frame that is both smaller and lighter. In addition, the PA Unit has a larger stroke and stronger force output. This is achieved through a 10% increase in transmissibility and further exploiting the harmonic properties of the PA. The Unit parameters are shown in Table 4.2. Note the same PSA was used in both Unit.

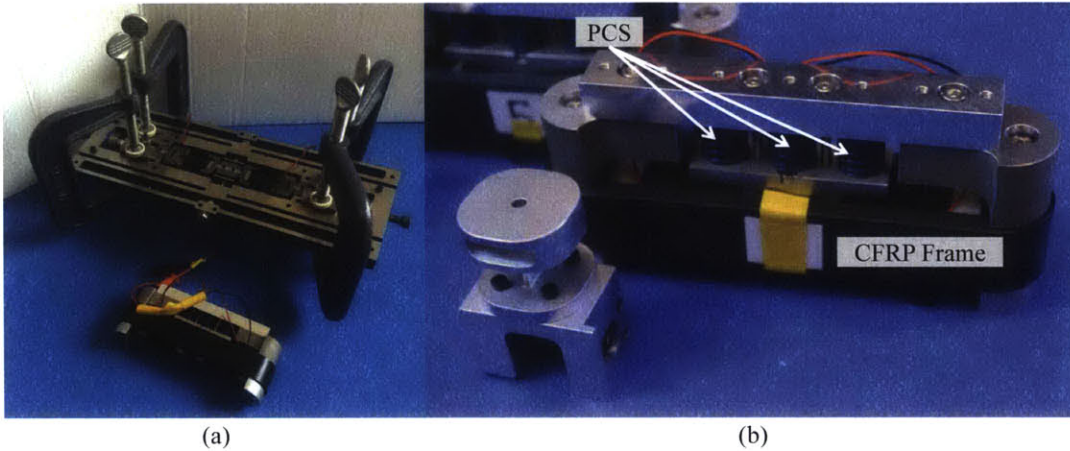


Figure 4-5: The buckling amplification Unit implemented in the PA. (a) A size comparison of between the proof-of-concept prototype and the PA Unit. (b) A labeled diagram showing a few of the new key features.

Table 4.2: Summary of Parameters of the PA Buckling Units

Parameter	Symbol	Value / Range
Cap Radius, r	23	mm
Output Node Radius, R	14	mm
PCS Stiffness, k_{pcs}	144	$\frac{N}{mm}$
Preload Force, f_{pre}	6000	N
Buckling Mechanism Mass, M_{unit}	0.360	kg

There are three design changes that directly benefit the performance of the buckling amplification Unit: fabricating the frame out of carbon fiber reinforced plastic (CFRP); decoupling the PCS from the requirement to balance the preload and constrain the motion of the output node; and biasing the PCS springs such that the Unit always has a downward force.

The most obvious and significant change was the use of CFRP for the frame. While a majority of the serial compliance is due to the rolling contact joints, the frame must be stiff enough not to cause a substantial drop in transmissibility. CFRP is a logical choice for multiple reasons. It has a Young's modulus to density ratio, i.e. a stiffness to weight ratio, 8 times higher than that of steel: 2.7×10^7 Nm/kg for steel and 2.2×10^8 Nm/kg for CFRP. The major drawback of CFRP is its anisotropic properties, it is distinctly in tension along the grain structure. The predominant load in the frame is tension in the direction of the Unit, so this bears no consequence. The PCS, however, cannot be directly integrated into the frame. This allows for greater optimization of the individual components, and to further reduce the size, the plane of the frame was rotated. Initially, the frame was in the same plane as the output, $X - Y$ see Fig. 4-5, so that the springs could be integrated. By decoupling them, the frame can now be placed in the $X - Z$ plane orthogonal to the output plane, reducing interference.

In addition to decoupling the PCS from the frame, in this iteration the PCS is also not responsible for the constraint of the output node. As detailed in Sec. 2.2.2, the output node must be constrained to a single degree of freedom, linear motion in the Y -direction. To reduce the size of the PCS, the PA structure was exploited to provide this constraint instead. The details of this constraint will be shown in the following section. Overall, this led to a much smaller compact PCS.

The final change was a bias force added via the PCS. By exploiting the same harmonic balancing used to remove the passive characteristics inherent to the buckling amplification mechanism proven in Proposition 3.2.1, the PA Unit can use a bias force to simplify the interface between the Unit and the Transmission. If both a positive and negative force needs to be transmitted, the interface must be able to withstand a tensile and compressive load. Conversely, if only compressive forces are required a single rolling contact, e.g. a roller-cam type mechanism, can aptly transmit the force. In addition, the force range, and consequently the stress range, of the unit is distinctly varied based on the input as shown in the previous figure, Fig. 2-5. The PCS does not need to exactly balance the preload as Eq. (2.20) describes, but instead tune

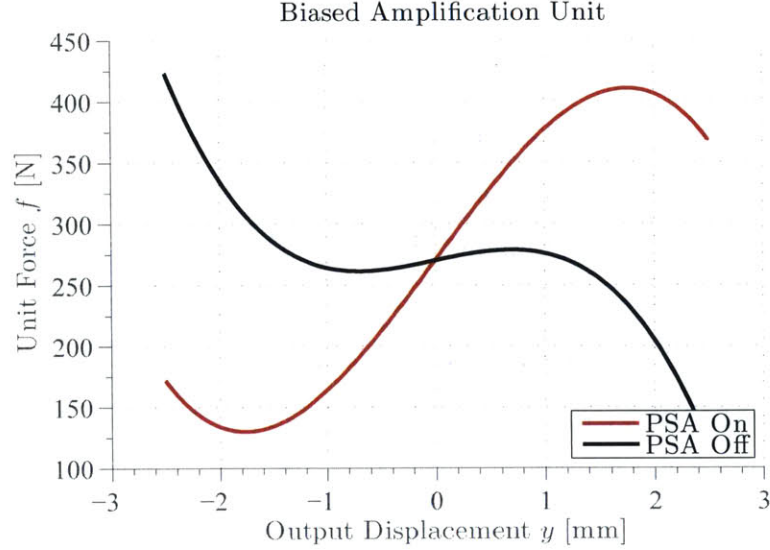


Figure 4-6: Force-displacement plot of the biased amplification Unit. Note the force is always positive and there is never a neutrally stable point. Furthermore, the peak forces for either extreme, on or off, are approximately the same magnitude ensuring low wear.

the linear term such that the peak in the on and off case are roughly equal ensuring a more even wear as shown in Fig. 4-6. The expression for the Unit output force becomes:

$$f = (k_{pre} - k_y)y + k_{eff} \frac{y^3}{2L^2} + \frac{y}{L} f_{eff} + f_{bias}, \quad (4.1)$$

where f is the force output of the Unit, k_{pre} is the effective stiffness of the PSA preload force, k_y is the stiffness of the PCS, k_{eff} is the effective stiffness of the PSA, L is the length scale of the buckling amplification mechanism, f_{eff} is the effective output force of the PSA, and f_{bias} is the bias force.

An additional benefit of the bias force is that the Units are always engaged directly with the transmission. This means that there is no backlash in the system. The PSAs are always in direct contact with the output and can rapidly react to any input. This enhances the practical bandwidth and ensures a minimal amount of play in the output position.

4.1.3 Design Optimization

Both of the presented implementations were designed with key features in mind, but neither were truly optimized in terms of achieving a peak performance metric. In general, a true design optimization must include an optimization of the PA in tandem with a set of specific functional requirements and design constraints. In addition, one of the most important components, the PSA, was not custom designed for this application. The following discusses a few trade-offs that were identified that would be crucial in a design optimization.

The dimensions of the PSA have a wide variety of effects on the design of the Unit. The force output scales linearly with the cross sectional area and the stroke scales linearly with the length. Therefore, the stiffness of the PSA can be tuned to match a given rolling contact joint. Given that the equation for transmissibility, Eq. (2.23), considers the normalized serial stiffness, a reduction in the PSA stiffness results in an increase in transmissibility. The major limitation preventing a design utilizing a long, skinny, compliant PSA is the loaded shear force. As shown in Fig. 4-7, the direction of mechanical load must be confined to within a cylinder with a radius roughly 10% of the width of the PSA. If the buckling unit acted exactly as the schematic shown in Fig. 2-3, this would not be an issue other than when considering manufacturing tolerances. However due to the rotation caused by the rolling contact, the mechanical load does tilt off axis by angle ϑ shown in Fig. 2-7, which is reproduced here for clarity in Fig. 4-8.

Assuming the PSA has a square cross-section, a fixed strain, and the cap radius has a fixed ratio with respect to the PSA length, the maximum amplification gain G_{pp} can be described as a function of the length-to-width aspect ratio of the PSA as shown in Fig. 4-9.

The design of the rolling contact surface encounters challenges similar to any bearing surface. The material should be stiff and have a high compressive yield strength, but the ultimate performance is highly dependent on the geometry of the rolling contact surface and the loading conditions. As the radius of the contact

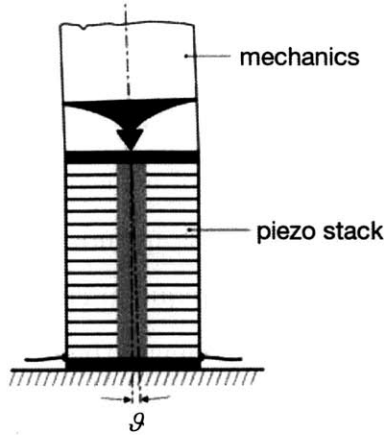


Figure 4-7: A figure provided by the PSA manufacturer describing the maximum off axis load angle ϑ .

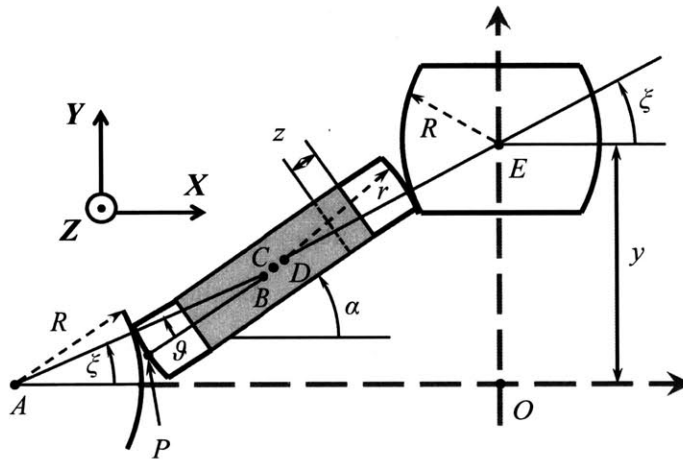


Figure 4-8: A reproduction of Fig. 2-7 to highlight off axis loading by angle ϑ caused by the rolling contact joint.

surfaces increase the stress decreases but so does the stiffness. These relationships are non-linear based on the Hertzian contact theory. [44] This includes the preload force and the variation of force due to the activation of the PSA. The cyclic loading of the surface is a dominant factor in the life of a Unit. Therefore, a balance must be struck between the surface radii, material, and loading conditions.

In addition to balancing the design trade-offs, there are several binary conditions that should be taken into account. For example, if the two rolling contact surfaces on the output node are concentric, it will be rotationally unstable about the Z-axis. A small rotation about that axis will force the two PSAs to produce a moment reinforce-

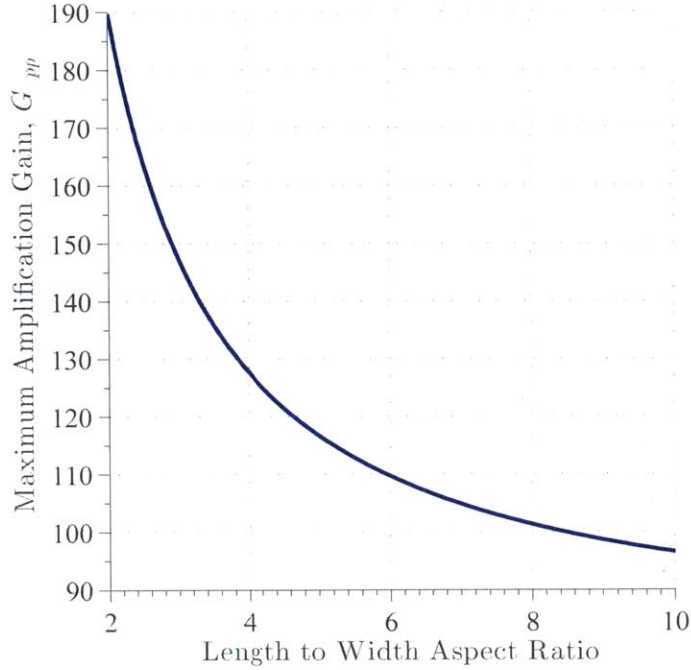


Figure 4-9: A plot of the maximum allowed amplification gain G_{pp} as a function of the length-to-width aspect ratio of the PSA, limited by the shear force caused by the rotation along the rolling contact joint.

ing the rotation. While the rotation can be prevented through proper constraint, it is possible to alleviate this instability by shifting the centers of the output node radii so the output node resembles more of an ellipse shape. The minimum magnitude of the shift depends on the rotation of the PSA and the ratio of the output node radius to the cap radius.

Furthermore, the distance from the contact point on the cap to the interface with the surface of the PSA should be large enough for the stress to be properly distributed. This can prevent awkward loading on the PSA including bending moments or stress concentration. The stress distribution can be simply modeled by via Rotscher's pressure-cone method typically used in bolt stiffness calculation. [30]

4.2 Poly-Actuator

Six buckling amplification Units were integrated into a harmonic PA proof-of-concept prototype shown in Fig. 4-10. The number of actuators satisfies the requirement in

(3.14b), $n = 6 > m+1 = 4$, so the PA output force, F , is independent of the nonlinear stiffness terms h_1 and h_3 . Note that with this input function, the terms c_q and d_q from Eq. (3.24) have the following properties: $c_q = 0, \forall q$ and $d_q = 0, \forall q \neq 2$. Therefore, there is only one choice for the input harmonic to produce a non-zero output force: $l = 2$. The necessary condition in Eq. (3.29) is satisfied, $n = 6 > l + p + 1 = 4$. The parameters in Eqs. (4.1) and (4.3) for the PA system are listed in Table 4.3.

$$f = h_1 y + h_3 y^3 + \eta_1 y u \quad (4.2)$$

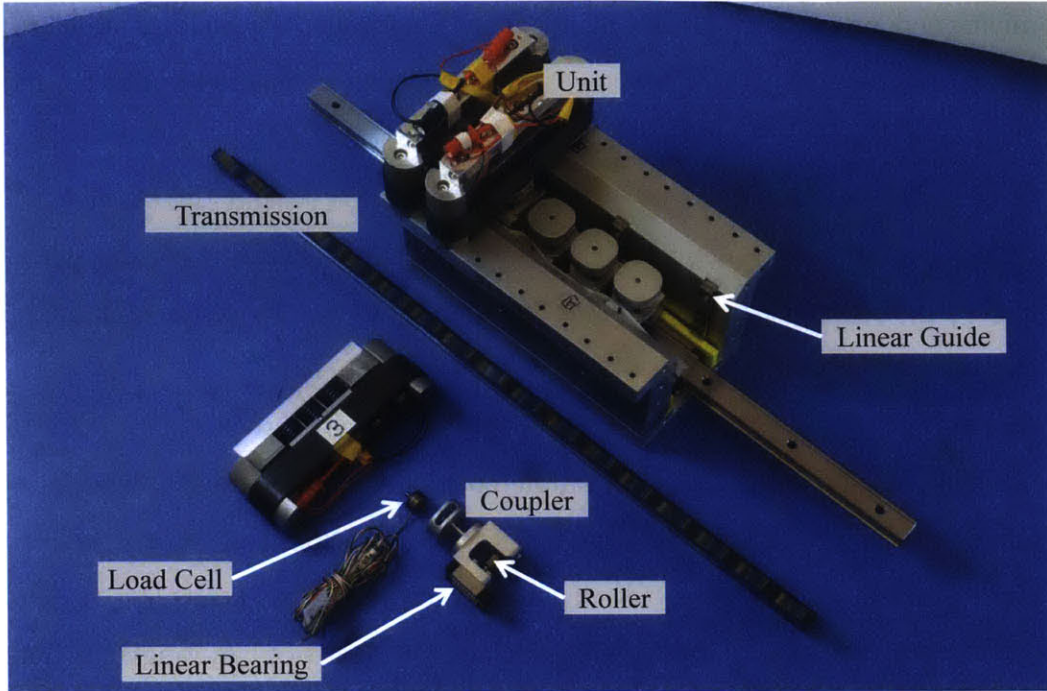
$$F = \sum_{i=1}^n \frac{\eta_1 A^2 \omega}{2} u_i \sin 2\theta_i \quad (4.3)$$

Table 4.3: Summary of Parameters of the Harmonic PSA Poly-Actuator

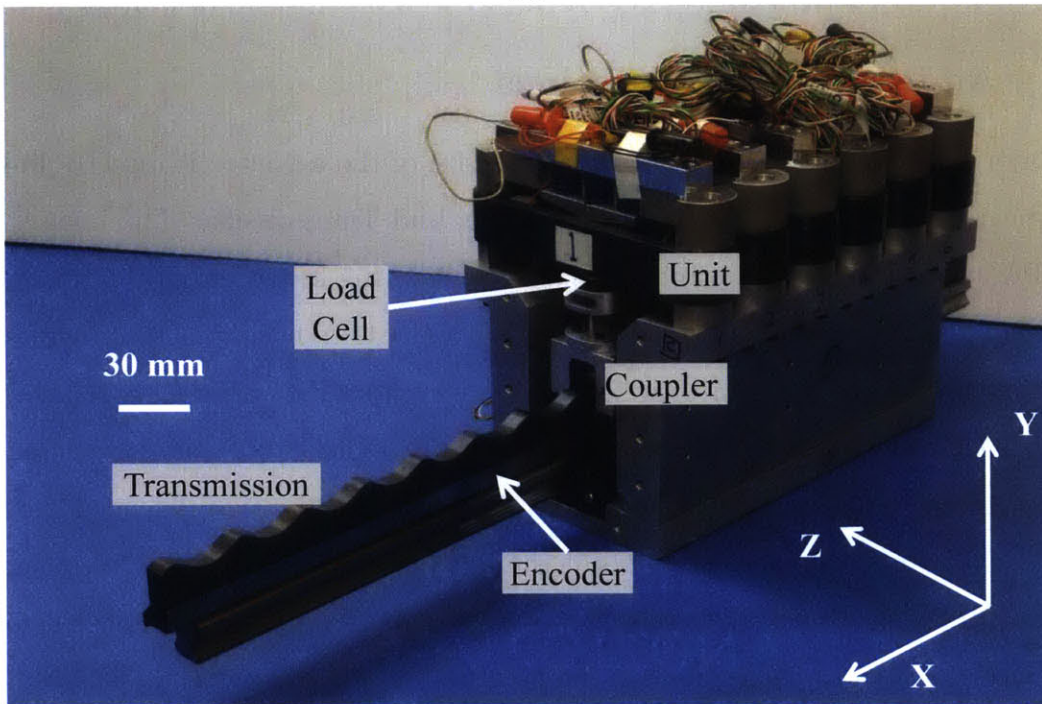
Parameter	Symbol	Value / Range
Effective input force	u	0-3730 N
Nonlinear stiffness coefficient, $\kappa = 1$	h_1	19 N/mm
Nonlinear stiffness coefficient, $\kappa = 3$	h_3	-12.5 N/mm ³
Coupling coefficient, $q = 1$	η_1	0.027 1/mm
Bias Force	f_{bias}	270 N
Transmission amplitude	A	2.5 mm
Transmission spatial wavelength	λ	27 mm
Transmission spatial frequency	ω	0.233 1/mm
Designed PA output force	F	± 110 N
Number of buckling Units	n	6

The Transmission dimensions were based on achieving a load capability of approximately 100 N and such that the Unit could be aligned one and one-sixth wavelengths apart from each other in accordance with the requirements described in Eq. (3.14).

A crucial component of the control scheme described in Sec. 3.2.4 is the measurement of the position to create the feedforward signal. The PA position is measured with an absolute linear encoder, a Renishaw RESOLUTE RL26. An absolute encoder was chosen over an incremental to ensure repeatability and remove the necessity for a homing sequence. The encoder has a resolution of 50 nm, an accuracy of 1.5 μm and a maximum velocity of 100 m/s.



(a)



(b)

Figure 4-10: Labeled pictures of the proof-of-concept PA prototype in (a) a disassembled and (b) assembled configuration. The encoder read head and power amplifier are not pictured.

As mentioned previously, the PCS no longer constrains the output node of the amplification mechanism. In this instance, linear bearings connected to the PA frame ensure the output is constrained to motion in the vertical (Y) axis. These bearings, shown in Fig. 4-10(a), also bear the Unit force in the PA output direction F_i . The roller on the coupler that transmits the force to the Transmission is coaxial with the center axis of the linear bearing. This prevents unnecessary moments that increase friction within the bearing.

Load cells were added in line with the output of each Unit to provide valuable sensing capabilities for debugging and online control. These load cells, while useful, added significant bulk to the overall actuator. Future iterations can greatly reduce the vertical size of the actuator by designing custom or low profile load cells. Furthermore, designs particularly focused on optimizing size and performance can weigh the benefit of online control with the expense of increased size and complexity.

4.2.1 Additional Considerations

The major bottleneck determining the overall size of the actuator is directly linked to the bearing stresses associated with the roller and Transmission. The innovation of the PA over previous large stroke actuators is removing friction from the transmission of force. The initial amplification mechanism exists to overcome the incredible stress that would exist within bearings on the length scale of a PSA displacement. Amplifying the displacement decreases the stress two-fold as the force is decreased and the length scale increases. The stress at this interaction is influenced greatly by more than just amplification ratio of the amplification mechanism. In terms of scaling, with the assumption the relative length ratios are roughly constant, the force scales with the area of the PSA, i.e. the length squared, whereas the displacement scales linearly.

The ball bearing mechanisms, e.g. the roller radial bearings, the Unit linear guides, etc., must minimize friction to reduce losses and improve positioning performance. Beyond proper lubrication and sizing, this can also be controlled by the magnitude and direction of the bearing loading. For example, the Transmission rides on two

linear bearings that bear the total vertical of all the units. The friction can be minimized by limiting the Unit bias force, and balancing the position of bearing and the Units such that the moment due to the unequal forces does not significantly contribute to the effective bearing load. Furthermore, the current Unit linear guides are recirculating ball bearings, however they do not have a long enough stroke to properly recirculate throughout the bearing track. Redesigning these bearings to be better integrated directly into the frame would reduce size and weight, while also improve loading conditions and lower friction.

4.3 Experimental Implementation

4.3.1 Implementation of Electronics

A linear amplifier, Cedrat LA75B, was used to power each Unit within the PA. While extremely accurate, the amplifiers are typically used for instrumentation and therefore have a low current saturation that limited the high power performance of the actuator. The system was controlled using a National Instruments cRIO NI-9075, which provided a single platform for all of the computation: the measurements of the linear encoder, Unit load cells and PSA current; the control computation; and the input signals for the amplifiers. Two output conditions were used during experimentation: no load and position driven. In the position driven case, the output was connected to a lead screw which could constrain the position either to a fixed point or driven at a variable velocity. When connected to the lead screw a load cell was added in series to provide a measurement of the PA output force, as shown in Fig. 4-11.

4.3.2 Force Ripple Compensation Based on Error Model

As analyzed previously in Section 3.2, the output force becomes imbalanced when the Units are misaligned or have diverse force-displacement characteristics. A spatial FFT of the output force, similar to the model shown in Fig. 3-4, can be measured and used

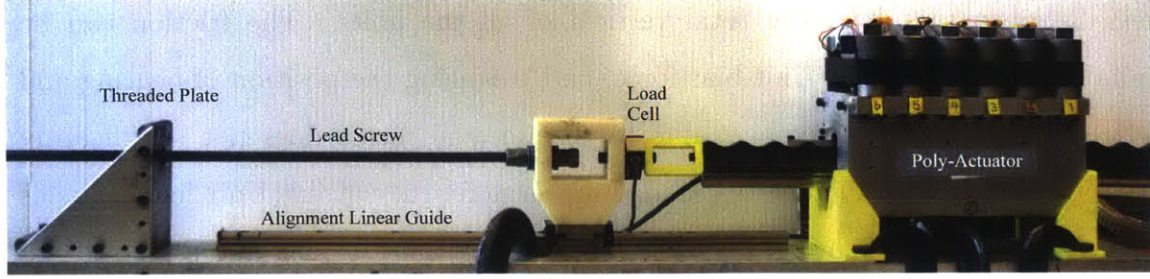


Figure 4-11: A labeled picture of the experimental implementation, including the PA, driving lead screw, and output measurement load cell.

to develop a low parameter model to compensate for the undesirable force ripple. In all cases, the resultant force deviation, or force ripple, \tilde{F} , can be expressed as a series of harmonic functions. This force ripple function can be effectively approximated as a finite order Fourier series of order V .

$$\tilde{F} \approx F_{ripple}(\theta) = \sum_{v=1}^V E_v \sin(v\theta + \psi_v) \quad (4.4)$$

The parameters E_v and ψ_v may be determined through experiments. Spatial Fourier analysis of measured force ripple provides E_v and ψ_v , $v = 1, \dots, V$, that represent the aggregate effect of all sources of error. Since the force ripple is a function of position alone, its effect can be compensated for by measuring the position of the PA, $\hat{\theta} = \omega \hat{x}$.

$$\hat{F}_{ripple}(\hat{\theta}) = \sum_{v=1}^V E_v \sin(v\hat{\theta} + \psi_v) \quad (4.5)$$

Subtracting \hat{F}_{ripple} from a nominal input command \bar{F} as demonstrated in Fig. 4-12, the ripple force can be significantly reduced. This compensation is similar to the cogging torque compensation for a synchronous motor [22], but a) the ripple force model (4.4) contains at most $2V$ parameters regardless of the number of Units n or the stroke of the Transmission, and b) the compensation law (4.5) does not include Unit index, i , and thereby no individual Unit compensation is required, only the

aggregate control.

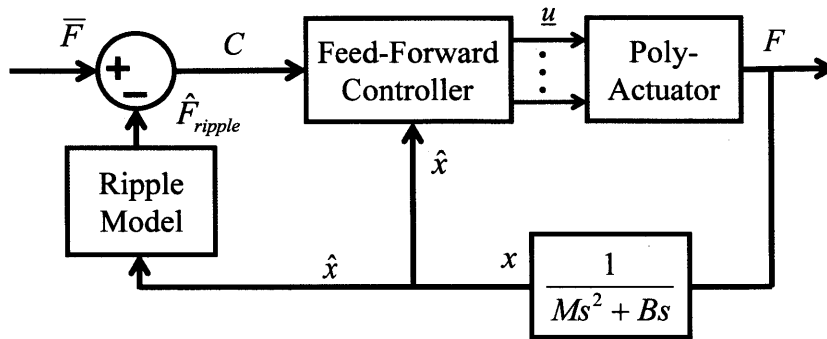


Figure 4-12: A block diagram of the feedforward force control including the ripple compensation and the phased sinusoidal inputs u .

4.3.3 Unit Force Control

The in-line Unit load cells can be used for online control as well as offline analysis. Reference inputs can be generated using the algorithm defined in Eq. (3.27) instead of the direct Unit inputs. Then a loop can be closed around each unit with a controller G_f as shown in Fig. 4-13. The possible benefit of this method was that it lessens the reliance on the previous ripple compensation method, which requires calibration. Furthermore, this would be robust to long-term changes such as creep or changes in friction or stiffness. Also, if a Unit was replaced in the PA, an additional calibration would not be required. Finally, it can compensate for complex phenomena such as hysteresis accurately provided the control is run at a high enough bandwidth.

The major limitation, however, is that it can only compensate for sources of ripple within the Unit, e.g. variations in the PCS stiffness or preload. It can't compensate for positioning errors or frictional variations that occur "downstream" of the force measurement. In addition, there are several singular points where the input cannot affect the output force. At these positions, the feedback control cannot compensate for an error and because each Unit has its own individual control, the other Units are ignorant to the issue and cannot contribute to maintain balance.

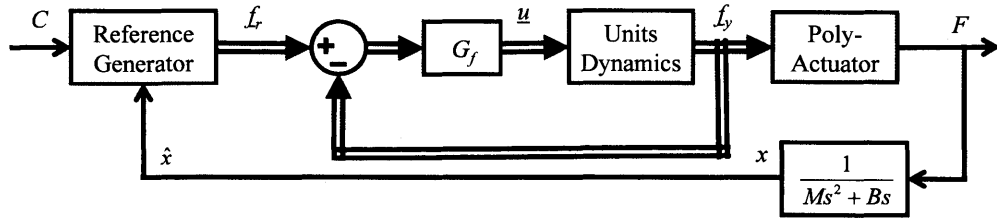


Figure 4-13: A block diagram of the Unit force feedback control including the ripple compensation. Instead of producing the inputs directly, the phased sinusoidal inputs generate the reference inputs f_r . Note the double lines denote a vector of size n , the number of Units.

4.3.4 Position Control

In addition to the ripple compensation, the control loop can be closed around the output position including a linear control block that outputs the desired force as shown in Fig. 4-14. As before, the position estimate \hat{x} is measured with the linear encoder.

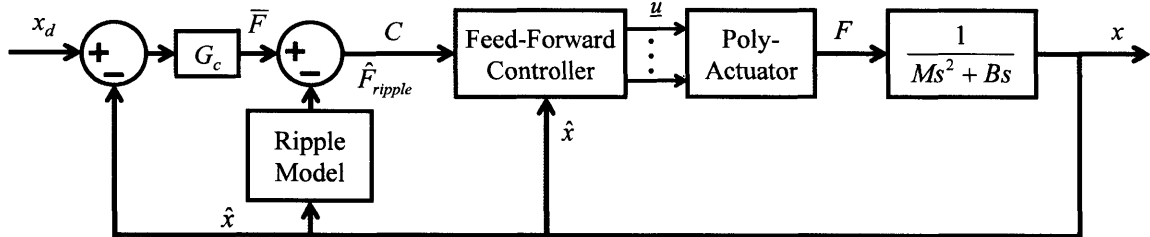


Figure 4-14: A block diagram using a general linear controller G_c to generate a force command to follow the reference position, x_d .

Several controllers G_c were implemented to overcome predicted and observed obstacles. Given purely the model as shown in Fig. 4-14, Proportional control is the simplest controller that provides control with zero steady state error. This model however ignores the static friction found largely at the output linear bearings, as discussed previously. Additionally, errors not fully compensated via the ripple compensation can also add disturbances that would limit pure Proportional control. PI control was implemented as well to overcome these issues, but the most frequent issue with this method is the slow settling caused by the integrator pole. Therefore, in addition to PI and Proportional, a Lead-Lag controller was employed. Finally due to input saturation, which practically limited both the voltage and current supplied

by the amplifier, gain scheduling was applied to prevent undesirable effects such as integrator wind up.

4.3.5 Simulation

A SIMULINK dynamic simulation was created to verify the dynamic model of the buckling amplification Unit and the PA. This simulation was experimentally verified and then used to test the theoretical limits of the design removing physical limitations, most significantly the current saturation of the linear amplifiers. It was also used to confirm assumptions made when determining which dynamic terms were insignificant and could be effectively ignored. Finally, the simulation provided measurements not realizable in implementation that are important for determining the integrity of the internal mechanics.

Given the capacitive loading properties of the PSA, the amplifier is modeled as a current source with saturation within a feedback loop that closes the loop around a commanded voltage. In addition, the current provided has two components: the charging of the PSA capacitance and the piezoelectric effect of the PSA velocity. The mechanical dynamic model is shown in Fig. 4-15. The PSA itself is modeled as a mass-spring-damper in parallel with the piezoelectric force source, ρ_p , k_{psa} , β_{psa} , and f_{in} , respectively. The output of the PSA is connected in series with a spring-damper modeling the collective joint stiffness, k_j and β_j , and then non-linearly transformed based on the buckling amplification. The transformation is modeled as instantaneous and lossless, therefore the power variables at those nodes, including \dot{z} and \dot{y} , are directly related by the instantaneous gain G from Eq. (2.4). The output node has a mass ρ_y which pushes on the compliant coupler at position y_c with mass-spring-damper properties: ρ_c , k_c , β_c , respectively. The compliant roller with stiffness k_r interacts with the Transmission which has an instantaneous gain $G_T = \frac{dx_i}{dy_i}$ that transforms the roller velocity \dot{y}_r to the output velocity \dot{x} . The forces from the phased Units are summed and applied to the mass-damper system at the output with parameters M and B , respectively. The simulation also could include a variety of non-linearities including friction/stiction, force ripple, discrete time sampling, and quantization. Several fac-

tors were not included in the simulation such as the hysteresis and internal dissipative heating.

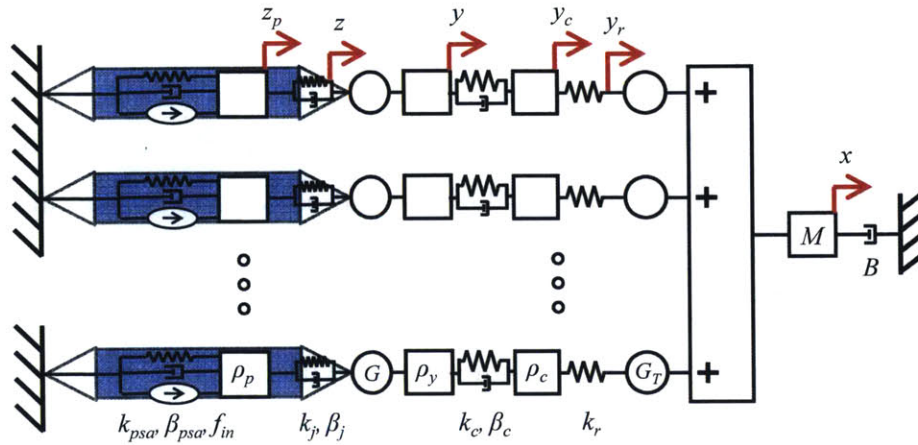


Figure 4-15: A schematic of the mechanical dynamic model used in the simulation

The simulation was verified by comparing like output conditions to the experiments described earlier. In addition, the output was driven at greater speeds than possible with the current implementation to predict the power and efficiency capabilities. Presentation and discussion of the results of the experiments and simulations are found in the following chapter.

Chapter 5

Experimental and Simulation Results

5.1 Unit Results

This section presents the measured force-displacement characteristics of both the proof-of-concept Unit and the PA Unit. The quasi-static parameters are solely presented due to the fairly insignificant dynamic properties on the overall output. As proven in Section 3.2.3, the individual Unit dynamic properties can be lumped into an effective overall mass or damping as viewed from the output. Furthermore, the effective lumped parameters are significantly smaller when compared to the actual mass and damping at the output due to the increased size. In addition, the PA Unit will be compared to some of the aforementioned mechanically leveraged PSA mechanisms.

5.1.1 Proof-of-Concept Unit

The prototype PSA with the flexure-free buckling displacement amplification mechanism and the preload compensation springs has been tested experimentally. Fig. 5-1 shows the measured force-displacement characteristics of the proof-of-concept buckling amplification mechanism prototype: f_y vs. y . A displacement source was aligned

in series with a load cell and connected to the output node, allowing for simultaneous measurement of both states. The circles show the measurements when the maximum voltage, 150 V, was applied, while the crosses are for 0 V. While the maximum voltage is applied, the prototype actuator produced a free displacement of 2.1 mm in either direction with a total net displacement of 4.2 mm due to the bi-directionality and an overall amplification gain of 81. The maximum force was 48 N when the PSAs were activated, while a maximum restoring force of 82 N was recorded when the PSAs were de-activated, producing 130 N of maximum peak-to-peak force.

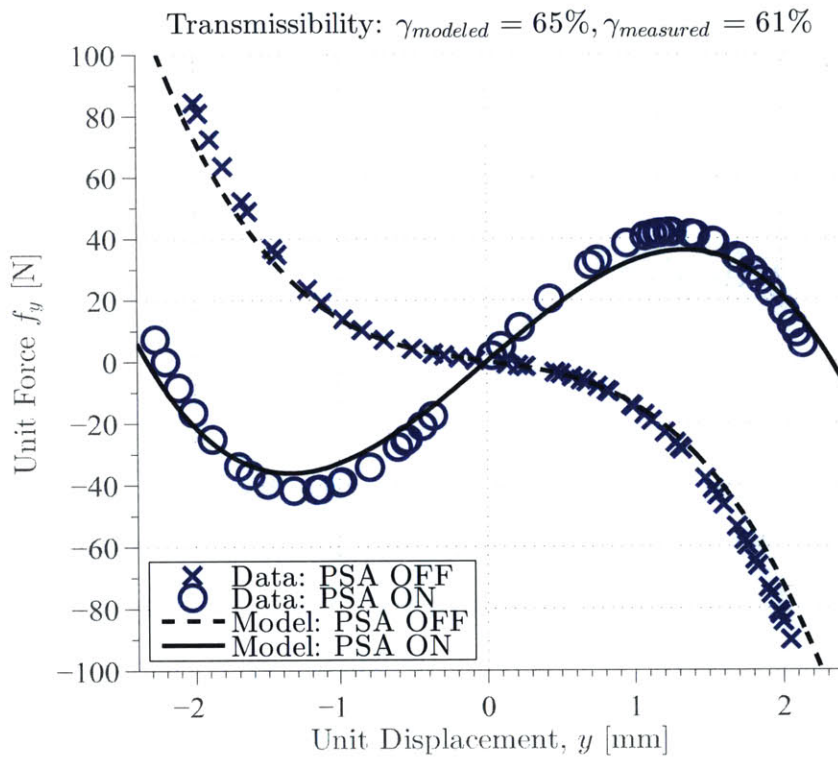


Figure 5-1: A plot of the force-displacement trajectory comparing the model of the initial prototype and the measured performance. A measured peak-to-peak displacement, Δy_{p-p} , of 4.2 mm and transmissibility, γ , of 61% was achieved.

The work output can be evaluated to determine the transmissibility of the prototype PSA buckling Unit based on the output force and displacement data. The two curves in the force-displacement plane produce 254 mJ of output work within one cycle of activation and de-activation, which corresponds to a transmissibility of 61%. This agrees closely with the analytic estimate of 65%. As analyzed previously, the

transmissibility does not depend on the transformer, i.e. the kinematic relationship of displacement amplification. This implies that the work output can be obtained by computing the area covered by one cycle of actuator operation in the output force-displacement plane, i.e. the $f_y - y$ plane. The experimental result of work output, 254 mJ, was obtained from the area between the two curves in the figure.

5.1.2 Poly-Actuator Unit

Similar measurements were taken for the 6 Units used within the PA. The measurements were taken both individually outside the PA, and assembled using the in-line Unit load cells. This confirmed the Units behaved as expected within the structure and provided estimates with regards to the vertical and horizontal errors, y_o and x_i respectively, that were discussed in the Section 3.3. The summary of the force properties are presented in Table 5.1. The table includes the specified target design values for comparison and statistical data, the average and standard deviation, for the measurements.

From the table, the cubic passive stiffness coefficient h_3 has the largest amount of variation from Unit to Unit, however, the force ripple caused by that term is fairly low. From the parameters listed, the largest source of ripple is the variation in the linear passive stiffness h_1 . This is logical because the term relies on the balancing of two separate design features: the manually-adjusted preload force and the PCS.

The difference in transmissibility between modeled and measured is largely due to the energy lost due to the PSA hysteresis. Approximately 7% of the energy was lost to hysteresis in a single full cycle. These hysteretic losses were taken into account for future calculations including the simulation. Hysteresis and internal friction also produced unmodeled force ripple at the PA, however the ripple maintained the harmonic phenomenon. This will be discussed in greater detail in the next section.

Table 5.1: Summary of Poly-Actuator Unit Measurements

Parameter	Units	Symbol	Modeled	Measured Avg.	St. Dev.
Preload force	[N]	f_{pre}	270	271	1.2
Linear stiffness	[N/mm]	h_1	19	18.8	0.5
Cubic stiffness	[N/mm ³]	h_3	-12.5	-12.84	0.57
Coupling term	[1/mm]	η_1	0.027	0.026	4.0×10^{-4}
Transmissibility	[%]	γ	71	66.2	1.1

5.1.3 Discussion

The major benefit, solely from the Unit standpoint, of the PA Unit over the proof-of-concept Unit is the use of CFRP as the frame material. The PA Unit performs well enough that it can be properly compared with other forms of PSA mechanical amplification. Table 5.2 shows the energy density by weight for multiple PSA mechanical devices.

Table 5.2: Comparison of Several PSA Mechanical Amplification Devices

Device	Transmissibility [%]	Amplification Gain [-]	Energy Density [J/kg]
Poly-actuator Unit	66.2	96	0.82
DWARF ¹	61	10	0.99
X-Frame ²	53	15	1.35
Nested Rhombus ³	11.9	210	0.145

While the transmissibility of the PA Unit is higher, the increased overall size of the actuator leads to a lower energy density. This comparison provides general characteristics, but it is important to note the large differences in implementation and capabilities of the actuators. Furthermore, the PA Unit mass does not take into account the necessary components to ensure the output node is properly constrained. In the current PA prototype, the mass of the linear guide is on the order of the Unit itself further lowering the energy density. The weight of this mechanism has not yet been optimized, however hence its omission.

¹P. Janker, *et al.*[17]

²E. Prechtel, *et al.* [33]

³J. Ueda, *et al.* [41]

5.2 Poly-Actuator Results

This section presents the experimental and simulated results of the PA prototype. Several experiments were conducted to confirm the theoretical results of previous chapters as well as to gauge overall performance of the actuator. Additional experiments were executed to verify the accuracy of the dynamic simulation. Once verified, the simulation was used to estimate the performance without the limitations of the physical prototype. These performance metrics are compared to other types of linear actuators.

5.2.1 Experimental Results

The first control method implemented was the ripple compensation. The force ripple was large enough that it significantly interfered with the feedforward and Unit force control methods. Furthermore, it caused atypical non-linear behavior during the position control. Once a reasonable level of ripple was achieved, position control was implemented and several key features were qualitatively confirmed.

Ripple Compensation

A spatial FFT of the output force, shown in Fig. 5-2, was used to confirm the claim in Section 4.3.2 that the force ripple is equal to a sum of sines with frequencies equal to that of the Transmission and a finite number of its harmonics. Note the first 6 harmonics have an amplitude significantly larger than the noise within the signal, while the higher order harmonics do not contribute.

Using the FFT and the measured data, a Fourier series based on the first 6 harmonics was fit to the data to create a model of the force ripple. This model is shown as the dashed line in Fig. 5-3a. This compensation method was tested using the model described in Eq. (4.5). The compensated force measurement is shown in Fig. 5-3b. Quantitatively, the force ripple can be represented by the RMS value of the force over the wavelength of the gear. The Fourier model-based compensator reduced the RMS ripple by a factor 290%. Qualitatively, observing the linear motion of the output,

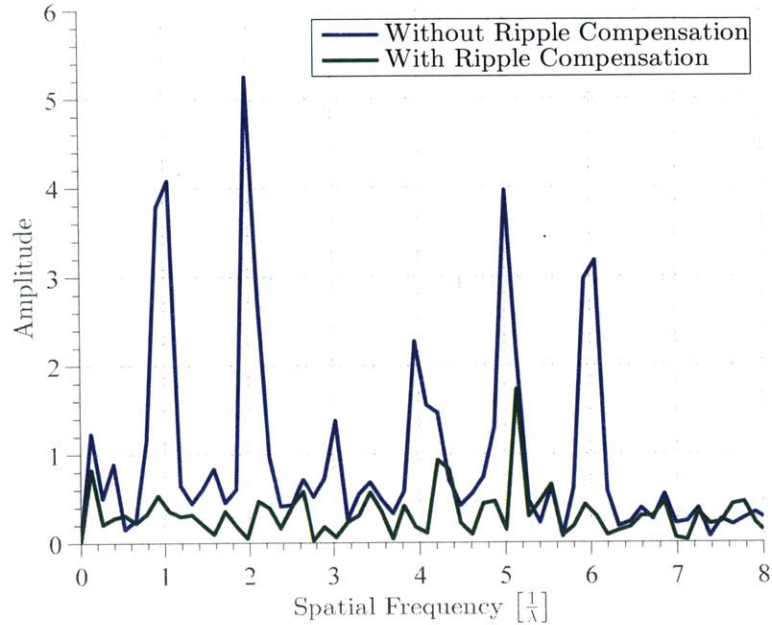


Figure 5-2: Spatial FFT of the output force ripple. The frequencies relate to the pitch of the gear and are affected by the discrepancies between Units, including position and stiffness.

the compensated velocity is significantly smoother and without as much jitter. Furthermore, the model-based compensator was able to reduce or eliminate “chattering” that occurred in the position controller described in detail below.

Feedforward Force Control

With the ripple compensation implemented, the feedforward force control implementation is straightforward. Using the method described in Section 3.2.4 after calibrating the input, the output force can be accurately driven, as shown in Fig. 5-4. In this experiment a static voltage is applied to each Unit based on the desired output trajectory described by the parameters C and φ in Eq. (3.30). Note the spatial frequency of the output is not a controllable parameter with static voltages. It is fixed at $l\omega$, where $l = 2$ in this case, hence why the sinusoidal force has a spatial wavelength of 13.5 millimeters.

By varying the voltages as the position changes, the force can now be controlled to be constant over the entire stroke. In order to minimize sensitivity and maximize

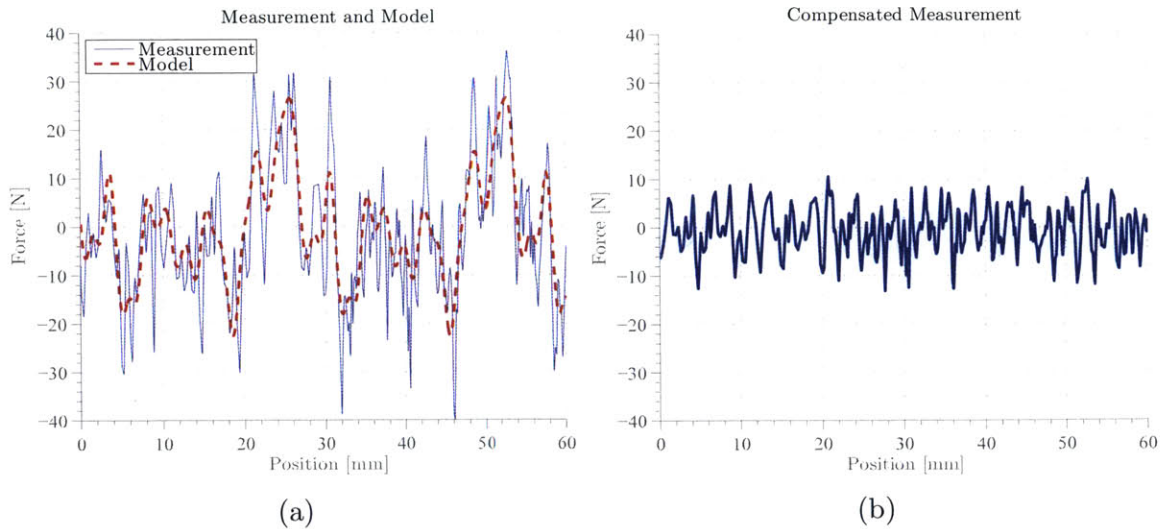


Figure 5-3: Two plots of the output force with a command of 0 N as a function of the output displacement. (a) In the first, the force ripple due to imbalanced Units is not compensated, but a model was developed based on a 6th order Fourier series model, shown in red. (b) The same command was given, but the ripple was compensated using the method shown in Fig. 4-14. Note the scales for both plots are the same.

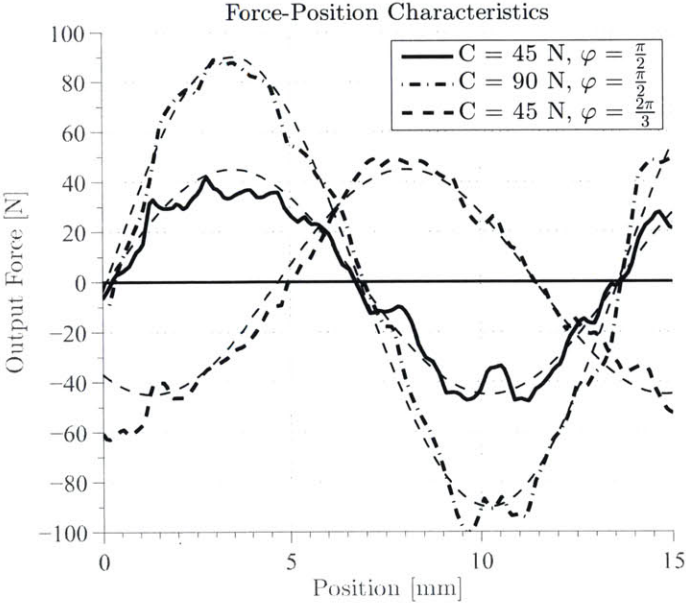


Figure 5-4: A plot showing the measured output force for three different inputs. The desired output is shown in the fine dashed line. Note this controller does include the ripple compensation.

the saturation limits, the sinusoid shown in Fig. 5-4 is always positioned such that ϕ is coincident with the current position. A constant output force was commanded

as the output was driven with the measurement apparatus with strokes longer than 50 mm (multiple Transmission wavelengths) while the PA force was measured. The output force was averaged over the entire stroke and the results are shown in Fig. 5-5.

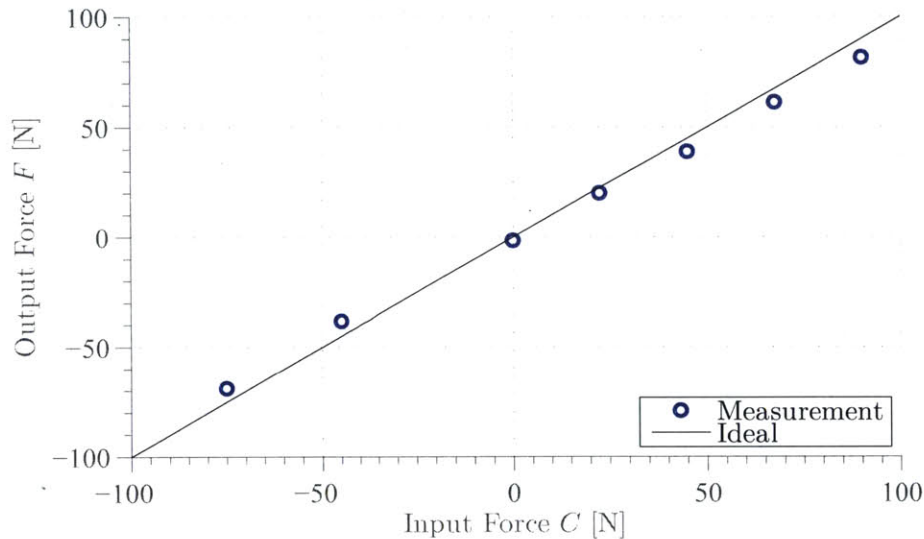


Figure 5-5: A plot showing the measured output force for three different inputs. The desired output is shown in the fine dashed line. Note this controller does include the ripple compensation.

Overall, the force remained within 10% of the commanded force. The PA output was driven in both directions and it was noted that the measured output force had a Coulomb friction component that was constant in magnitude regardless of commanded force, but the direction of force always opposed the direction of motion. The static friction component was measured to approximately 17 Newtons and averaged out of the force control data. This friction became more important during position control. Note the output force saturates due to the inherent limits of the PSAs, which are rated for a maximum electric field before the dielectric breaks down. The static friction limits this maximum force further to a total of 90 Newtons.

Unit Force Control

Unit force control attempts to reduce the need for ripple compensation by attempting to measure each Unit force and control it to within the reference command. Theo-

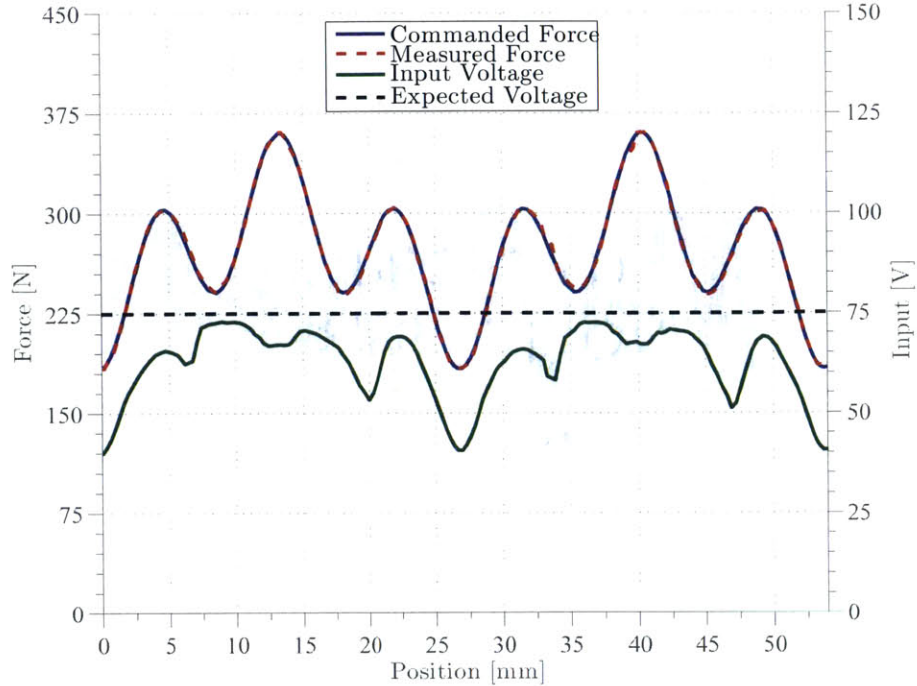


Figure 5-6: A plot of the individual Unit force control as function of the PA output displacement. A reference command (shown in blue) is passed to a feedback controller that varies input voltage (shown in green) to change the Unit force which is then measured (shown in red). In this example case the reference command is based off a desired PA output force. The expected (feedforward) command is shown in black.

retically this would allow for a balance of the passive force properties associated with the buckling Unit, e.g. the stiffness, preload, and PCS. The Unit force control was implemented using the in-line load cells within the PA to confirm the theoretical performance. The controller G_f , shown in Fig. 4-13, is a pure integral control, as there are essentially no dynamics between the voltage input u_i and the force output f_y . This control is verified in Fig. 5-6.

The most significant result from this experiment is the large variation of the input voltage, when the expected input was constant. The commanded output force in this example was nil at the output, which correlates to a constant input. However each Unit has a force that changes with displacement. This force profile was the generated reference profile shown in blue. The Unit force f_y is shown in red and follows the command to within a fraction of a percent, but the input varies by approximately 20% of its range.

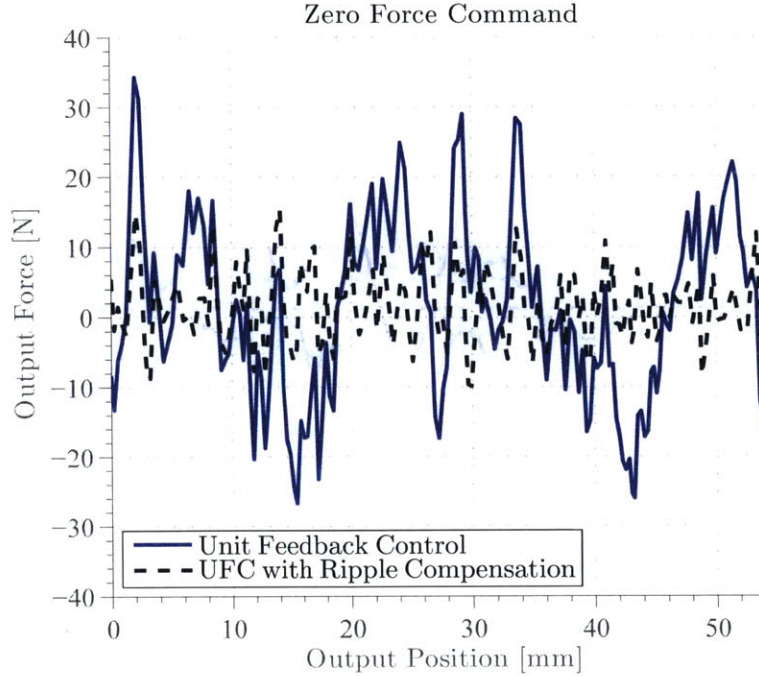


Figure 5-7: The output force of the PA as a function of output position utilizing Unit force control. The blue line plots solely the Unit force control, whereas the black line shows the Unit force control in conjunction with ripple compensation.

With the individual control confirmed, the overall output force was tested over a similar range. The results are shown in Fig.5-7. The input command in this example was again zero, but the results are not as accurate as the individual Unit. There is still a large variation in the output force due to unbalancing errors “downstream” of the Unit force feedback. In particular, the feedback cannot compensate for errors in position, horizontal x_i or vertical y_o , and it has a limited ability to overcome errors in the bias force f_{bias} . Furthermore, it is ignorant of any friction associated with the linear or rotary bearings. The ripple is approximately 20% less than the uncompensated feedforward output force, however this decrease in ripple hardly justifies the increase cost in sensors and computation.

It is interesting to note, that the errors are still periodic and repeatable over multiple trials. Therefore, it is still possible to implement ripple compensation, which is also shown in the figure. This provides the smoothest force control, as the ripple magnitude was the smallest with Unit force control and ripple compensation. But the increased complexity was not worth the minimal benefit of lower ripple so

for the remainder of the experimental results, feedforward force control with ripple compensation was used.

Position Control

The first controller implemented was a proportional control with the knowledge that it would not be able to position accurately due to the static friction and the force ripple. This provided a rough estimate of repeatability however, where the repeatability can be defined as the distribution of ending positions given the same input. Based on a variety of step sizes and initial starting positions, the repeatability correlated highly with the ripple harmonic with the largest magnitude. Without ripple compensation, the repeatability was approximately ± 4 mm; with ripple compensation, that was improved to ± 1.4 mm which correlates with the 5th harmonic of the Transmission spatial wavelength.

Furthermore, the experiment provided insight into non-linear phenomenon witnessed in nearly all the controllers with improper gains. First of all, with a large step the velocity will be saturated due to the current limitation within the linear amplifier. This saturation was consistent around 330 mm/s regardless of the controller. With a small gain, the output is likely to stop just before or just after the desired position, where the error is not large enough to force the controller to overcome the friction, as shown in Fig. 5-8. Increasing the gain too much results in a common behavior where the actuator enters a limit cycle, or “chatters.” This occurs when the actuator pushes too hard to overcome friction, the inertia carries the output too far, and the input switches sign and overshoots again ad infinitum. The goal of the more complex controllers is to overcome the steady state error without approaching the limit cycle behavior.

The next step after proportional control was PI control. The first plot, Fig. 5-9, highlights a variety of possible responses for small steps where velocity saturation does not play a major role. Depending on the initial and final position with respect to the ripple, the output may quickly jump to the desired position, as in Trial 1, or it may be suddenly pushed by a spike in the ripple, as in Trial 3. Either way,

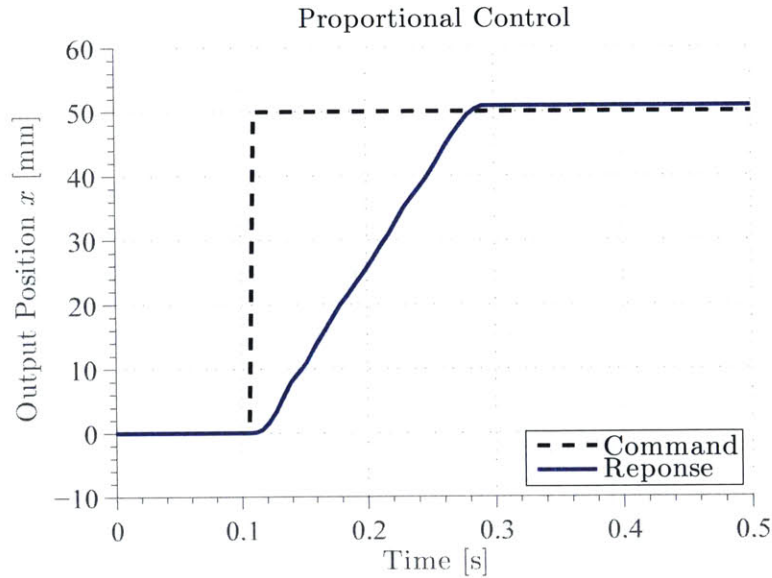


Figure 5-8: A step response of the PA with a proportional controller. Note a steady state error exists due to the force ripple and static friction.

the integrator is eventually able to overcome the disturbances including the static friction, however the time constant is extremely long. This is related largely to the limit on the gains to prevent the limit cycle behavior.

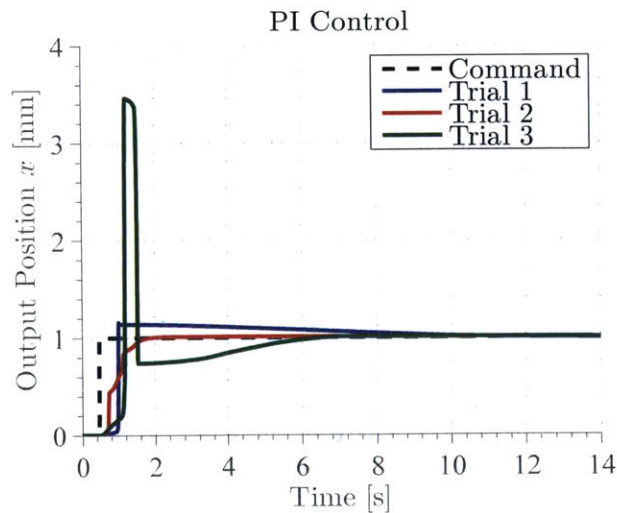


Figure 5-9: Several 1 mm step responses were measured at different initial positions utilizing a PI controller and ripple compensation. The variety of responses is due to the difference in the ripple force with position. Ultimately, the integrator is able to overcome the disturbances, but with a long time constant.

The second response plot, Fig. 5-10, exemplifies the limitation of the slow integra-

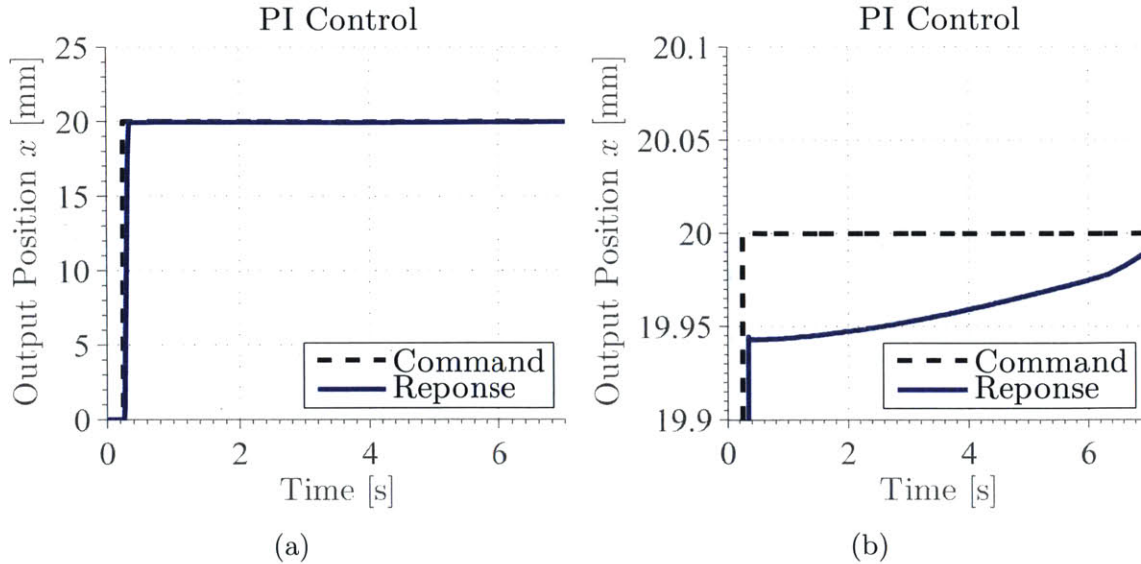


Figure 5-10: A step response exemplifying the two time scales of the PI controller. Both plots show the same experiment, however the first (a) shows the time scale of the velocity saturation region, and the second (b) shows the slow response of the integrator term. Note both plots have the same time scale.

tor response. The actuator is able to travel 99.7% of the distance within 0.1 seconds, but the final error is integrated away over several seconds. Note Fig. 5-10b has the same time scale but a reduced position scale to demonstrate the difference is time constant. Once again, the initial response is limited by the current saturation, but the controller is eventually able to overcome the force ripple and static friction. As would be expected, the slow time constant in the large step closely matches that of the small step shown in the previous figure.

A lead-lag controller was implemented to overcome the slow integrator dynamics. The lead-lag allowed for faster dynamics without increasing the gain to the point of chattering, as shown in Fig. 5-11. The time constant of the lead-lag system is an order of magnitude faster than the PI controller. Note the large overshoot is a consequence of the ripple, that effect cannot be accurately predicted and therefore cannot be anticipated, however as before the lag term overcomes any disturbances. The two separate regimes: velocity saturation and fine position, lend themselves to two separate control laws, i.e. gain scheduling. This also prevents integrator wind up or other runaway scenarios. If the distant (saturated) controller is modeled simply

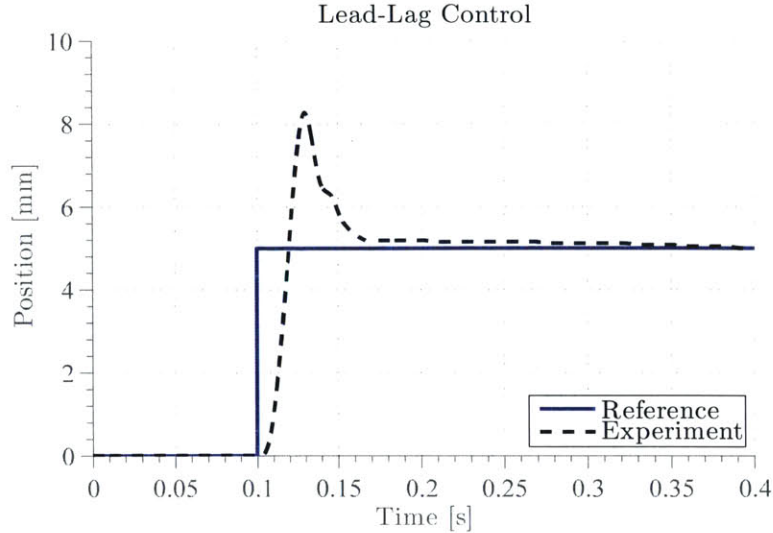


Figure 5-11: Lead-lag step response

a proportional gain, the boundary between the two would be the maximum output force divided by the proportional gain measured in N/mm .

In summary, the PA has a working stroke of over 200 mm with an accuracy of 1.5 micrometers, currently limited by the linear encoder. Due to the high encoder resolution and fine voltage control, it can reliably make 0.8 micrometer incremental steps, which is 0.003% of the Transmission wavelength. The resolution of this prototype is mostly limited by the static friction and the stick-slip effect at very small displacements, but reducing the accuracy of the linear encoder or amplifier could cause the resolution to reduce. Furthermore, the resolution can be affected by the force ripple. If, for example, the desired position had an unstable stiffness from the force variation it could cause the resolution to increase. For larger steps, on the order millimeters, the PA has a 2% settling time of approximately 0.3 seconds.

5.2.2 Simulation Results

The purpose of the simulation is to allow for extrapolation of the current system to attempt to foresee future limitations and predict practical performance. The simulation had three steps of verification: electrical dynamics, force dynamics, and positioning dynamics. Whenever possible, measured parameters were used including all of the

values already presented. For more difficult parameters to accurately model, such as the output viscous damping, the physical measurements were used. The simulation also included several implementation properties, e.g. quantization and the sampling frequency of the controller, however the discretization was fine enough that they did not have significant effects on the output.

Verification

The first verification is to confirm the electrical dynamics. The electrical dynamics are dominated by two parameters: the current saturation of the voltage amplifier and the capacitance of the PSA. The RC constant of the circuit is fast enough that the bandwidth is entirely dictated by the charging speed of the amplifier. These parameters were verified using a step response and a bode plot comparing the commanded voltage to the measurement, shown in Fig. 5-12

This being one of the simplest aspects of the model, the simulation agreed with the measurements nicely and confirmed the specified values for the capacitance of the PSAs and the current saturation of the linear amplifier. The hysteresis provides the only significant deviation between the model and measurement, most notably in the negative step response of the voltage. However, the discrepancy would only affect the transient response and not the steady state minimizing its impact on the accuracy of the simulation as a whole.

In an isometric measurement, the PA output, and therefore all of the Units, maintain a constant position, which implies that the non-linear aspects of the PA are static even if the input is changing. All of the same control methods apply but by making the nonlinearities static, the effects of the current saturation can be isolated from effects of other nonlinear phenomenon. For this verification, a sinusoidal input is given to magnitude of the phased sinusoidal input, i.e. $C = C(t) = C_o \sin \omega_t t$; where ω_t is the temporal frequency. Therefore, the individual inputs are given by $u_i(x, t) = U_2 \sin \omega_t t \sin 2\theta_i$; where the position θ_i is held fixed. The results are shown in Fig. 5-13.

The larger input commands are affected by the current saturation sooner because

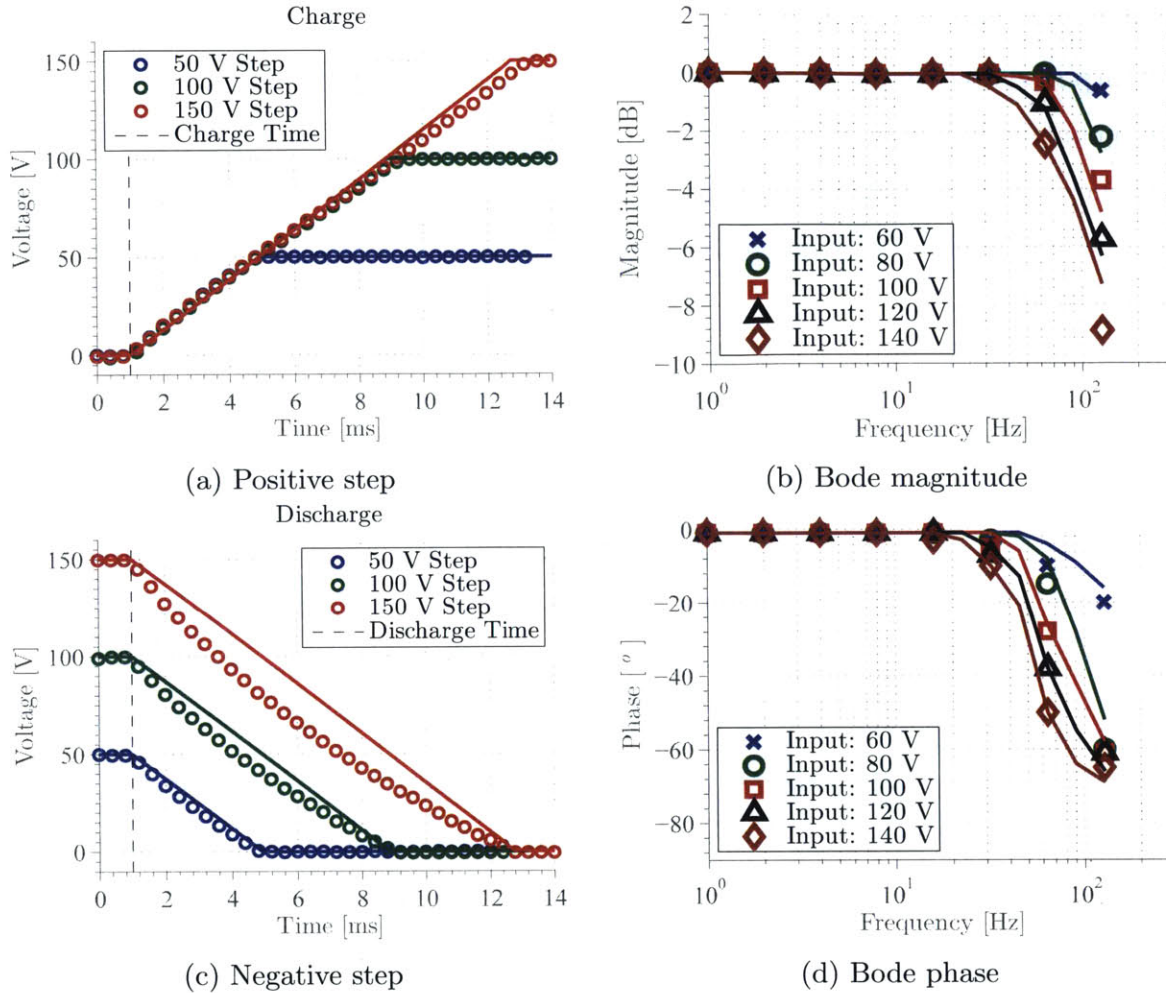


Figure 5-12: Several plots showing the verification of the electrical dynamics between the physical prototype and simulation. In general, the discrete points are measurements, whereas the continuous lines are simulation data.

of the larger currents required to charge the PSAs quickly. This leads to a decrease in the effective bandwidth of the PA. This verification confirmed the magnitude of the transmitted force and demonstrated the effect of current saturation on the output force. The bandwidth provided is theoretical upper limit for the specified amplifier because the position was held constant. As the PA moves the PSAs will draw additional current to provide the necessary mechanical power, thus reaching the amplifier saturation at lower frequencies and effectively reducing the bandwidth further.

The final verification tested the accuracy of the output position step response. In both the experiment and the simulation, a position control loop with lead-lag linear

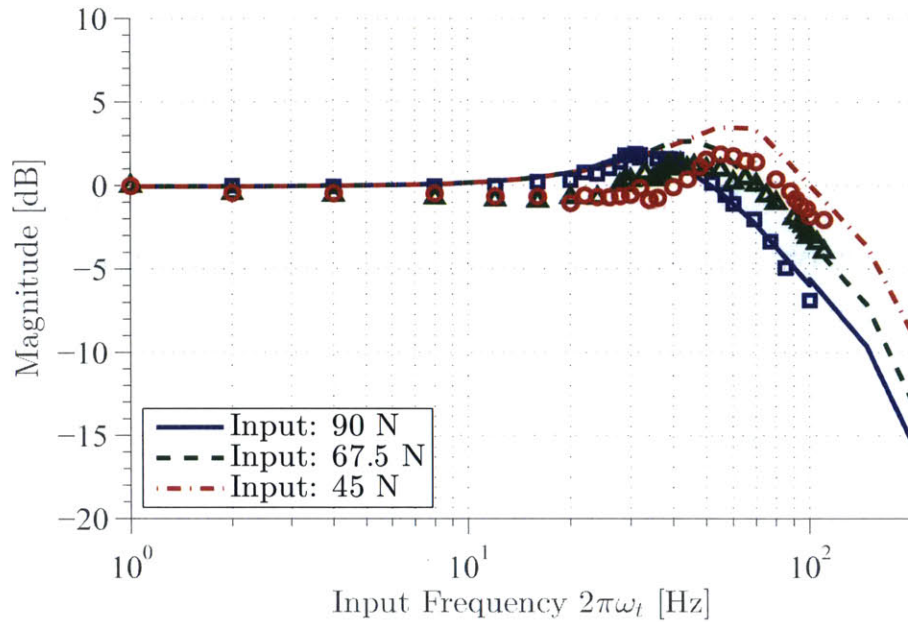


Figure 5-13: A bode diagram of the output force with respect to the input frequency. The bandwidth changes with input because the current saturation affects the larger voltages sooner. Note the discrete points represent experiments, whereas the continuous lines are simulation data.

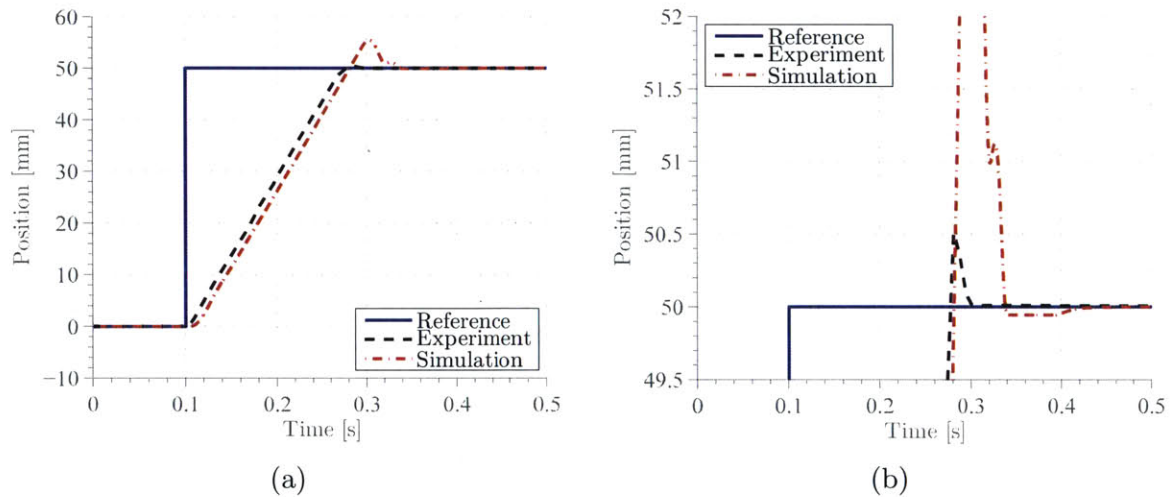


Figure 5-14: The measured and simulated step response of the PA. (a) Shows the complete response over, whereas (b) enlarges the response near the commanded position to highlight the dynamic response.

controller was commanded to step the output position by 50 mm, shown in Fig. 5-14. A large step was used to test both regimes of the response: first, the velocity saturated region; and second, the dynamic response near the commanded position.

This verification was essential for determining values for the Coulomb and viscous friction. Furthermore, it confirmed the validity of the velocity-current transformer in the PSA and the accuracy of the lead-lag controller. A model of the compensated ripple was included to the simulated output force which, in combination with the Coulomb friction, is responsible for the nonlinear characteristics near the commanded position, shown in detail in Fig. 5-14b.

Extrapolation Results

Summarizing the experimental and verified simulation results, it is clear the amplifier current saturation resulted in a limitation in gauging the peak performance of the actuator. Therefore, the saturation limit was raised in the simulation and the simulations were re-run for comparison. The saturation had little effect on the positioning ability of the actuator, so the high-speed performance was the focus of this analysis. The Unit input commands u_i were defined by Eq. (3.58) where the desired force \bar{F} was the maximum: 90 N. The PA force was measured while the position was driven at a constant velocity. This simulation was then repeated for several velocities, where the results are shown in Fig. 5-15.

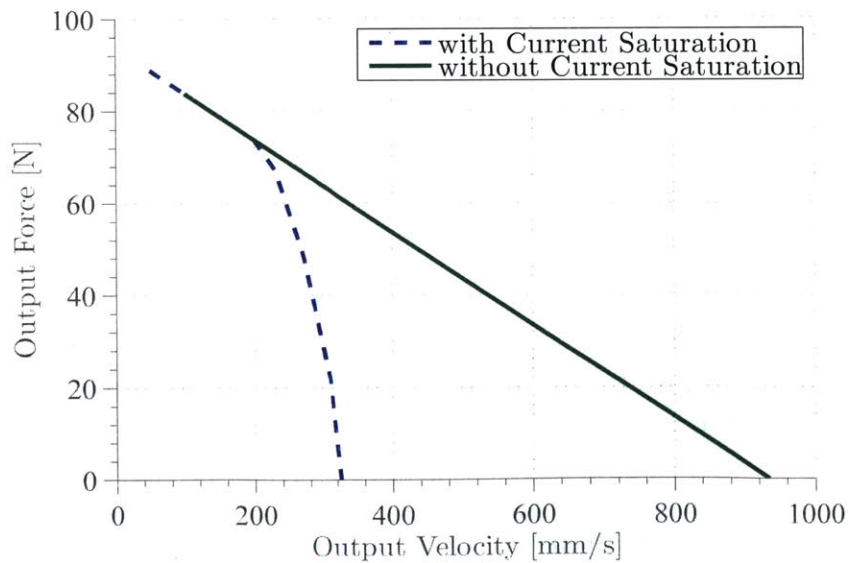


Figure 5-15: A plot of the simulated PA force as a function of the output velocity, both with and without amplifier current saturation.

Comparing the two results, it becomes clear where the current saturation begins to degrade the output force at approximately 200 mm/s. This corresponds to an input frequency of 15 Hz, much lower than the isometric measured bandwidth of the PA output force. The transmission of power from the amplifier to the PA output requires a higher current causing the amplifier to saturate quicker. The peak velocity, or no load speed, of the PA with saturation is 330 mm/s, which agrees with the previously measured value. Without the saturation, the force essentially decays linearly due to the viscous damping until it reaches a no load speed of 920 mm/s, which corresponds to an input frequency of 68 Hz. The peak current of each Unit at the no load speed is 1.05 A.

The linear decay of the velocity exemplifies the concept that the PA dynamics are dominated by the output impedance given they can provide the necessary power. The bandwidth of the internal components are generally higher than the output already due to the higher stiffness and lower mass. But in addition, this difference is increased because the displacement/velocity amplification of the system acts as a “gear accelerator” instead of a gear reducer. Although the amplification is highly nonlinear, the general increase in velocity yields a reduction in the effective mass of internal dynamics. Given that the modeled output dynamics are straightforward—a mass, a viscous damper and Coulomb friction—the results are similarly simple. This simplistic response is observed in the output power of the actuator as well, shown in Fig. 5-16. The output power is defined as the product of the output force and the output velocity.

Again, the point of departure from the two results due to the current saturation is clear at 200 mm/s. The peak power for the PA with the current limited amplifier is 15.2 Watts. It is important to note that the linear amplifier is able to output much more than 15.2 Watts in total. However since each Unit is being controlled separately a saturated channel can't receive additional power from another. Given the distribution of the Units and the charging algorithm defined by Eq. (3.58), typically at least two Units are not effective at driving the PA output and therefore do not draw significant power. Furthermore, a significant portion of the amplifier

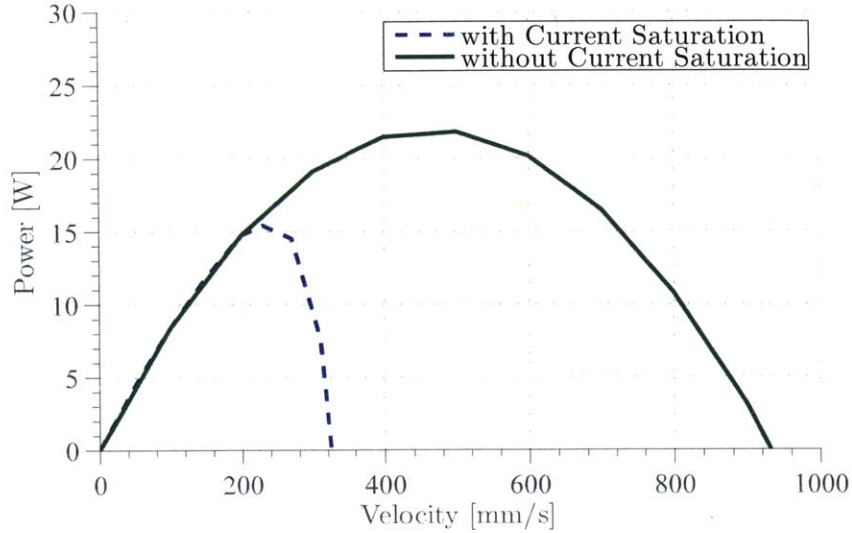


Figure 5-16: A plot of the simulated PA output power as a function of the output velocity, both with and without amplifier current saturation.

power has to go towards driving the capacitance of the PSAs.

Without current saturation, the maximum output power is 22 Watts at 460 mm/s. This result agrees with the simple formula for the output power of a linear system: $P_{out,max} = F_{stall}/2 \times v_{no\ load}/2$; where $P_{out,max}$ is the maximum output power, F_{stall} is the stall force, and $v_{no\ load}$ is the no load speed. This reinforces the idea that the main source of power dissipation is friction at the output.

For the measured level of friction and damping, the internal dynamics had minimal effect on the output. So the simulation parameters were adjusted to reduce friction to analyze when this assumption became invalid. As the damping coefficient was lowered, the output power of the actuator increased. The speed was increased until the activation frequency of the PSAs reached the recommended driving frequency from the manufacturer, 300 Hz. The linear speed and output power associated with this input frequency is 4 m/s and 100 W. At this point, the internal losses can cause the temperature to rise to the point of failure. Furthermore, before this 300 Hz limit is reached, the increase in temperature would cause a change in the PSA properties yielding the simulation inaccurate. However, it is accurate in measuring the transmission of the force from the PSA to the output and the assumption that the internal dynamics are negligible remained valid.

5.2.3 Discussion

Based on the experimental and simulation results, a few guidelines can be derived for improving the PA. The current PA prototype can be improved by providing an amplifier with a higher current saturation and by increasing the spatial frequency of the Transmission. As the simulations showed, a higher current produced more speed and power. The simulation also showed that the largest loss mechanism was the friction at the output. The output force is proportional to the spatial frequency, but the friction is independent. Therefore, the Units can run at a higher frequency achieving the same speed while increasing the force, which increases the output power.

Table 5.3: Comparison of Actuator Properties

Device	Stress [kN/m ²]	Power Density [W/kg]	Strain Rate [s ⁻¹]
Poly-actuator Prototype	4.3	5.1	35*
Optimized Poly-actuator [†]	20	100	100*
Muscle ⁴	350	>100	5
Piezoacoustic ⁵	80	4	16
Kiesewetter ⁶	1030	5	5×10^{-4}
Electromagnetic ⁷	20	200	10
Hydraulic ⁸	5×10^4	>1000	>10
Pneumatic ⁸	900	800	>10

* The strain rate of the PA is normalized by the Transmission wavelength, not its full stroke

† Approximated theoretical performance of an optimized prototype.

Ultimately, there are three limiting factors to consider to maximize the output power: the current saturation, the viscous friction and the heating within the PSAs. The viscous friction affects the output velocity, whereas the temperature increase is a function of the driving frequency. The spatial frequency can be designed to match the friction and heating limitations, which in turn specifies the maximum current required from the amplifier.

⁴I. Hunter, *et al.*[16]

⁵T. Shigematsu, *et al.* [36]

⁶W. Kim, *et al.* [19]

⁷J. Hollerbach, *et al.* [15]

⁸J, Huber *et al.* [14]

Based on this theoretical optimization and assuming a reduction in mass via streamlining of the design as discussed in Section 4.2.1, the dynamic performance of the PA can be improved. A conservative estimate of these properties are provided with comparison to the simulation model and other common linear actuators in Table 5.3.

Overall, the PA provides several desirable features. First and foremost, it is capacitive and backdrivable as intended. Provided the measurement and control resolution is fine enough, the output can be controlled to within a very high degree of accuracy. The optimized power density is comparable to that of muscles and electromagnetic actuators. However, the force density will always be low because the force is reduced by the displacement amplification.

Chapter 6

Conclusion and Future Work

6.1 Project Goals

This thesis presented a novel, high power piezoelectric linear actuator. Piezoelectric actuators were chosen based on several criteria, but mostly their capacitive transmission, efficient operation, and backdrivability. The capacitive transmission allows for static loads to be borne without drawing significant power. Backdrivability is an important feature in several fields, including interactive robotics where collisions with a rigid object could cause damage to the robot and/or the people interacting with it. Overall, the backdrivability is a passive feature that does not require high-bandwidth control or force sensors on the output. However, it is possible to dictate a desired output stiffness with control, improving its safety capabilities.

The high power piezoelectric actuator combines two amplification concepts: mechanical and frequency amplification. The mechanical amplification stage focused on a large gain while maximizing the transmitted energy, so the energy transmission did not have to rely on friction. The amplification was increased 10 fold compared to other similar mechanisms by exploiting the extremely large amplification due to controlled structural buckling. The resulting device can produce 100 times the displacement within a single stage. Rolling contact surfaces were used as the rotational joints to effectively eliminate friction and maximize the rigidity of the structure. The rigidity directly affected the transmissibility and the overall energy the device can

output. The challenge with the singular device was the high degree of nonlinearity.

The frequency amplification capitalized on the harmonic structure of the Transmission to balance the undesirable nonlinearities present due to the mechanical stage. The theory showed that the passive terms of the individual Units, including stiffness, damping, and mass, can be balanced without the need of additional control, yielding a smooth output force. Furthermore, the harmonic structure provided a means to output a constant force that did not rely on the position of the actuator. The control algorithm presented showed both the force and the instantaneous stiffness of the output can be controlled independently, barring limits due to saturation. This relates directly to the importance of backdrivability.

Implementation showed that the force profile was not smooth due to imperfect balancing. Errors in the location of the Units as well as the Unit properties yielded a force ripple that had a distinct pattern related to the sinusoidal output. Using standard linear control techniques, the output was controlled with an accuracy and resolution of 1.5 and 0.8 micrometers, respectively. For small step commands—less than one-half Transmission wavelength—the settling time was less than 0.3 seconds.

The measured performance was limited by the capabilities of the power amplifier controlling the PSAs, therefore, a simulation was developed to predict the maximum power performance. With an amplifier with a higher current, the poly-actuator could output 22 Watts for a power density of 5.1 W/kg. Several suggestions were made for improving this power output further, including matching the effect of the limiting factors: current saturation, friction, and heating within the PSAs. With several straightforward design improvements, the power density could theoretically be improved to approximately 100 W/kg.

6.2 Contributions

This body of work has led to several practical contributions:

- Preload compensation spring: An important criteria for interfacing with the PSAs maintained contact with the buckling amplification structure. This was

achieved through a preload force. In addition, the preload force allowed for a greater amount of energy to be extracted from the PSAs each stroke, effectively increasing the energy density. A restoring force was required to balance the preload, but the restoring force needed to be constant throughout the stroke. Any variation would restrict the performance of the mechanism. Instead of using a complex material, e.g. shape memory alloy, that would be under an extreme amount of stress, it was shown that a simple linear spring connected to the output node of the amplification mechanism provided the necessary constant preload force within less than 1% for the stroke of the actuator.

- Rolling contact gear teeth: Operation of the buckling mechanism required proper alignment of the relative rotation among the several rolling contact surfaces. Ideally there are no tangential forces that would cause the surfaces out of alignment, however at high speed dynamic forces could cause slip. This was prevented by integrating a gear tooth and slot that did not bear any of the large axial forces, but could ensure alignment within an acceptable tolerance. Furthermore, the teeth aided in the initial alignment during the complex assembly of the amplification mechanisms.
- Unit bias force: The physical interaction between the individual Units and the Transmission was simplified by applying a bias force to the Unit. Initially, it was expected that the Unit would apply a positive (upward) and negative (downward) force, requiring rollers on the top and bottom of the Transmission and a high machining tolerance for the location of the rollers. Furthermore, the Units would have backlash when the Unit switched the direction of the force. It was recognized that if all of the Units received the same bias force, the net effect on the actuator output was nil and so a bias force was added so that the Units only applied a force downward. This led to the elimination of the backlash and a reduction in size of the Transmission and Unit coupler. The bias force also changed the loading of the roller. The average stress on the roller increased, but the variation was lowered.

- Design optimization criteria: While the design parameters of manufactured components in the poly-actuator Unit prototype were carefully selected, several items were purchased off the shelf and were not optimized for overall performance. An analysis was presented identifying the key geometric and material properties that affected the performance of the Unit the most. These considerations included: the maximum allowable shear force applied to the PSA with respect to the amplification gain and size of the PSA; the stress within the rolling contact surfaces compared to the preload force and PSA stiffness; and the relationship between the size and stability of the output node.
- Sufficient balancing proof: A key conclusion of the thesis was the idea that multiple Units connected in parallel along a single Transmission could balance, yielding a smooth output with no passive force variation with respect to position. In addition to this idea, a sufficient condition that guaranteed passive balancing was proven provided that the Unit force and Transmission functions are approximated as a certain class of functions. Furthermore, the method presented provided a frame work for finding unique solutions given individual Unit force and Transmission function.
- Ripple modeling and compensation: While the ideal theory claimed the output force would have no dependency on the output position, a method for modeling errors revealed that a force ripple would exist when there are errors in the parameters of the design. It was shown that errors, particularly errors within the Units, would cause a repeatable ripple that had frequency components directly related to the spatial frequency of the Transmission. As an example, the ripple associated with a Unit parameter variation was explicitly derived. The phenomenon was verified experimentally by analyzing a FFT of the measured output force. A compensation method was proposed inspired by a technique common among synchronous motors. Given that the force ripple was repeatable, the output force can be measured over several wavelengths of the output Transmission and fitted utilizing a finite order Fourier series. This compensa-

tion method works well because the ripple can be approximated by a low order model—2 times the order of the Fourier series—and it is applicable beyond the range that was initially measured. Additionally, it does not require any supplementary sensors because it only relies on a measurement of position.

6.3 Future Work

Future design consideration involving this actuator would need to be heavily focused on the power amplifier for several reasons. First, most off the shelf products that interface with piezoelectric actuators are lower power with a high degree of accuracy. The accuracy of the applied voltage is not as important in a high power actuator compared to a sensitive sensor or servos. Whereas the current saturation can directly limit the maximum speed of the actuator. Second, the electrical efficiency of the amplifier can be greatly improved by recovering the electrical energy stored on the capacitive element of the PSAs. Finally, linear amplifiers are traditionally large and inefficient. While continuous voltage control is important for maintaining a high degree of output force resolution, by lowering the resolution it may be possible to use alternative techniques that are more efficient while minimizing the effects at the actuator output.

In terms of mechanical design, the actuator can be greatly reduced in size by the removing the large Unit linear bearing. They could be replaced with an integrated structure that provides the necessary support for the Units to operate properly. The overall size of the actuator is generally a direct function of the size of the radial bearing allowing the roller to interact with the Transmission. Any form of bearing that can reduce the size further without introducing unacceptable losses due to friction could allow the actuator to be reduced further. Finally, the Unit force control that utilized the inline load cells was found to have a limited benefit in terms of control, but certainly aided in assembly and debugging. However, the size of the load cells was unnecessarily large and could be reduced to limit the effective mass of the Unit output.

Appendix A

Derivation of the Mechanism Transmissibility

In order to derive the work output by the PSA within an amplification mechanism, the trajectory must be determined using several parameters: the stiffness, free displacement, and blocking force of the PSA, k_{psa} , z_{free} , and f_{block} , respectively, and the serial and parallel stiffness associated with the mechanism, k_s and k_p , respectively. The trajectory, shown in Fig. A-1, can then be integrated to find the overall work output via Eq. 2.1. Given the points shown in Fig. A-1, the total work output is:

$$W_{out} = \frac{f_{block} z_{free} k_s^2 k_{psa}}{(k_{psa} + k_s)(k_{psa} k_s + k_{psa} k_p + k_p k_s)} \quad (A.1)$$

Recognizing that the ideal work output of the PSA is: $W_{psa} = f_{block} \times z_{free}$, and the definition of transmissibility is: $\gamma \equiv \frac{W_{out}}{W_{psa}}$, the transmissibility can be expressed as:

$$\gamma = \frac{k_s^2 k_{psa}}{(k_{psa} + k_s)(k_{psa} k_s + k_{psa} k_p + k_p k_s)} \quad (A.2)$$

By substituting $k_s = k'_s \times k_{psa}$ and $k_p = k'_p \times k_{psa}$ into Eq. A.2, it becomes Eq.

2.2.

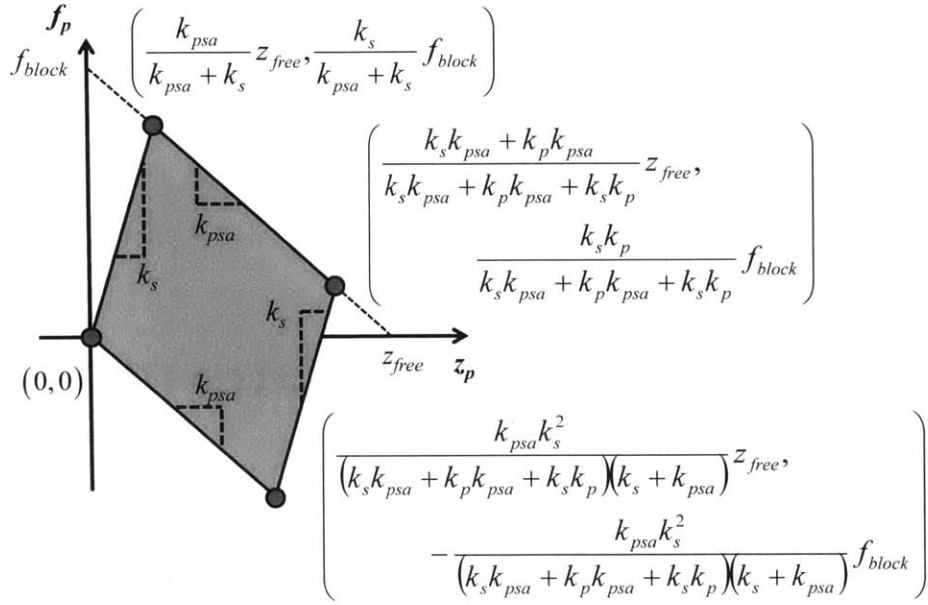


Figure A-1: The force-displacement trajectory, c , of a PSA with stiffness, blocking force and free displacement of k_{psa} , F_{block} , and z_{free} , respectively, within a mechanism with a serial and parallel stiffness, k_s and k_p , respectively.

Bibliography

- [1] R Akmeşe and JF Eastham. Design of permanent magnet flat linear motors for standstill applications. *Magnetics, IEEE Transactions on*, 28(5):3042–3044, 1992.
- [2] GB Andeen and R Kombluh. Design of compliance in robots. In *Robotics and Automation, 1988. Proceedings., 1988 IEEE International Conference on*, pages 276–281, 1988.
- [3] P. Barragan and H. Asada. Design of energy-saving PZT drive amplifiers for mobile and wearable physical assists. In *Proceedings of the 2011 ASME Dynamics Systems and Control Conference*, volume 2, pages 783–790, October 2011.
- [4] Ion Boldea and Syed A Nasar. Linear electric actuators and generators. In *Electric Machines and Drives Conference Record, 1997. IEEE International*, pages MA1–1, 1997.
- [5] A. Borboni. *Meso- to Micro-Actuators: A Theoretical and Practical Approach*, chapter Modeling Actuators, pages 176–205. CRC Press, Boca Raton, FL, 2008.
- [6] D. Campolo, M. Sitti, and R. Fearing. Efficient charge recovery method for driving piezoelectric actuators with quasi-square waves. *IEEE Transactions on Ultrasonics, Ferroelectrics and Frequency Control*, 50(3):237–244, 2003.
- [7] X. Deng and S. Avadhanula. Biomimetic micro underwater vehicle with oscillating fin propulsion: System design and force measurement. In *Proceedings*

of the 2005 IEEE International Conference on Robotics and Automation, pages 3312–3317, April 2005.

- [8] A. Dogan, Kenji Uchino, and Robert E. Newnham. Composite piezoelectric transducer with truncated conical endcaps “cymbal”. *Ultrasonics, Ferroelectrics, and Frequency Control, IEEE Transactions on*, 44(3):597–605, May 1997.
- [9] John F Donovan, Linda D Kral, and Andrew W Cary. Characterization of a lorentz force actuator. In *28th AIAA Fluid Dynamics Conference, 4th AIAA Shear Flow Control Conferences, Snowmass Village, CO, June, 1997*.
- [10] R.S. Fearing, K. H. Chiang, M.H. Dickinson, D. L. Pick, M. Sitti, and J. Yan. Wing transmission for a micromechanical flying insect. In *Proceedings of the 2000 IEEE International Conference on Robotics and Automation*, volume 2, pages 1509–1516, April 2000.
- [11] R. Fenn, J. Downer, D. Bushko, V. Gondhalekar, and N. Ham. Terfenol-d driven flaps for helicopter vibration reduction. *Smart Materials and Structures*, 5(1):49–57, 1996.
- [12] E. Furukawa, M. Mizuno, and T. Doi. Development of a flexure-hinged translation mechanism driven by two piezoelectric stacks. *JSME International Journal*, 38(4):743–748, 1995.
- [13] S. Hall, T. Tzianetopoulou, F. Straub, and H. Ngo. Design and testing of a double x-frame piezoelectric actuator. In *SPIE International Conference on Smart Materials and Structures*, volume 3985, pages 26–37, March 2000.
- [14] J. Huber, N. Fleck, and F. Ashby. The selection of mechanical actuators based on performance indices. *Mathematical, Physical and Engineering Sciences*, 453(1965):2185–2205, 1997.
- [15] Ian W Hunter, John M Hollerbach, and John Ballantyne. A comparative analysis of actuator technologies for robotics. *Robotics Review*, 2, 1991.

- [16] I.W. Hunter and S. Lafontaine. A comparison of muscle with artificial actuators. In *Proceedings of the 1992 5th Technical Digest IEEE Solid-State Sensor and Actuator Workshop*, pages 178–185, June 1992.
- [17] P. Janker, M. Christmann, F. Hermle, T. Lorkowski, and S. Storm. Mechatronics using piezoelectric actuators. *Journal of the European Ceramic Society*, 19(67):1127 – 1131, 1999.
- [18] J. Kim, S. Kim, and Y. Kwak. Development and optimization of 3-d bridge-type hinge mechanisms. *Sensors and Actuators A: Physical*, 116(3):530–538, 2004.
- [19] Won-jong Kim and Ali Sadighi. A novel low-power linear magnetostrictive actuator with local three-phase excitation. *Mechatronics, IEEE/ASME Transactions on*, 15(2):299–307, 2010.
- [20] Hermano Igo Krebs, Bruce T Volpe, Dustin Williams, James Celestino, Steven K Charles, Daniel Lynch, and Neville Hogan. Robot-aided neurorehabilitation: a robot for wrist rehabilitation. *Neural Systems and Rehabilitation Engineering, IEEE Transactions on*, 15(3):327–335, 2007.
- [21] Yong Kwun Lee and Isao Shimoyama. A skeletal framework artificial hand actuated by pneumatic artificial muscles. In *Robotics and Automation, 1999. Proceedings. 1999 IEEE International Conference on*, volume 2, pages 926–931. IEEE, 1999.
- [22] J.-P. Louis. *Control of Synchronous Motors*, chapter Optimal Supply and Synchronous Motors Torque Control, pages 107–113. Wiley, 2010.
- [23] H. Ma, S. Yao, L. Wang, and Z. Zhong. Analysis of the displacement amplification ratio of bridge-type flexure hinge. *Sensors and Actuators A: Physical*, 132(2):730–736, 2006.
- [24] J. Maas, T. Schulte, and N. Frohleke. Model-based control for ultrasonic motors. *Mechatronics, IEEE/ASME Transactions on*, 5(2):165–180, Jun 2000.

- [25] T. Mashimo, K. Awaga, and S. Toyama. Development of a spherical ultrasonic motor with an attitude sensing system using optical fibers. In *Robotics and Automation, 2007 IEEE International Conference on*, pages 4466–4471, April 2007.
- [26] M. Muraoka and S. Sanada. Displacement amplifier for piezoelectric actuator based on honeycomb link mechanism. *Sensors and Actuators A: Physical*, 157(1):84–90, 2010.
- [27] D. Neal and H. Asada. Bipolar piezoelectric buckling actuators. *IEEE/ASME Transactions on Mechatronics*, 19(1):9–19, February 2014.
- [28] R.E. Newnham, A. Dogan, Q.C. Xu, K. Onitsuka, and S. Yoshikawa. Flextensional “moonie” actuators. In *Ultrasonics Symposium, 1993. Proceedings., IEEE 1993*, pages 509–513 vol.1, Oct 1993.
- [29] C. Niezrecki, D. Brei, S. Balakrishnan, and A. Moskalik. Piezoelectric actuation: State of the art. *The Shock and Vibration Digest*, 33(4):269–280, 2001.
- [30] Carl C Osgood. Saving weight on bolted joints. *Machine Design*, 51(24):128–133, 1979.
- [31] Joel C Perry, Jacob Rosen, and Stephen Burns. Upper-limb powered exoskeleton design. *Mechatronics, IEEE/ASME Transactions on*, 12(4):408–417, 2007.
- [32] J. Pons. Piezoelectric actuators. In *Emerging Actuator Technologies: A Micromechatronic Approach*, pages 46–100. Wiley, 2005.
- [33] E. Prechtel and S. Hall. Design of a high efficiency, large stroke electromechanical actuator. *Smart materials and Structures*, 8(1):13–30, 1999.
- [34] Nicolaas Bernardus Roozen and Gerard Van Schothorst. Mri apparatus with a piezo actuator in a non-rigid suspension of the gradient coil carrier, April 2003. US Patent 6,549,010.

- [35] T. Secord and H. Asada. A variable stiffness PZT actuator having tunable resonant frequencies. *IEEE Transactions on Robotics*, 26(6):993–1005, 2010.
- [36] Takashi Shigematsu, Minoru Kuribayashi Kurosawa, and Katsuhiko Asai. Nanometer stepping drives of surface acoustic wave motor. *Ultrasonics, Ferroelectrics, and Frequency Control, IEEE Transactions on*, 50(4):376–385, 2003.
- [37] P.H. Stahlhuth. Piezoelectric stack motor stroke amplifier. U.S. Patent 4,769,569, Sept. 6, 1988.
- [38] G. Strang. *Computational Science and Engineering*, chapter Fourier Series and Integrals, pages 330–331. Wellesley Cambridge Press, 2007.
- [39] K. Takemura and T. Maeno. Design and control of an ultrasonic motor capable of generating multi-dof motion. *Mechatronics, IEEE/ASME Transactions on*, 6(4):499–506, Dec 2001.
- [40] K.K. Tan, T. Lee, and H.X. Zhou. Micro-positioning of linear-piezoelectric motors based on a learning nonlinear PID controller. *Mechatronics, IEEE/ASME Transactions on*, 6(4):428–436, Dec 2001.
- [41] J. Ueda, T. Secord, and H. Asada. Large effective-strain piezoelectric actuators using nested cellular architecture with exponential strain amplification mechanisms. *IEEE Transactions on Mechatronics*, 15(5):770–782, 2010.
- [42] V.K. Varma and W.E. Dixon. Design of a piezoelectric meso-scale mobile robot: a compliant amplification approach. In *Proceedings of the 2002 IEEE International Conference on Robotics and Automation*, volume 2, pages 1137–1142, May 2002.
- [43] Yi Wang, Gregory Cole, Hao Su, Julie G Pilitsis, Gregory S Fischer, et al. Mri compatibility evaluation of a piezoelectric actuator system for a neural interventional robot. In *Engineering in Medicine and Biology Society, 2009. EMBC 2009. Annual International Conference of the IEEE*, pages 6072–6075, 2009.

- [44] W. Young. *Roark's Formulas for Stress and Strain*, page 651. McGraw-Hill, USA, 6th edition, 1989.
- [45] Michael O Zenge, Mark E Ladd, Florian M Vogt, Katja Brauck, Joerg Barkhausen, and Harald H Quick. Whole-body magnetic resonance imaging featuring moving table continuous data acquisition with high-precision position feedback. *Magnetic resonance in medicine*, 54(3):707–711, 2005.